NAVAL POSTGRADUATE SCHOOL
Monterey, California

THESIS

MICROCHEMICAL ANALYSIS OF NON-METALLIC
INCLUSIONS IN C-MN STEEL SHIELDED METAL
ARC WELDS BY ANALYTICAL TRANSMISSION
ELECTRON MICROSCOPY

by

Jon D. Walters

June 1998

Thesis Advisor: Alan G. Fox

REPORT DOCUMENTATION PAGE

Public reporting burden for this collection of information is estimated to average 1 hour per response, including the time for reviewing instruction, searching existing data sources, gathering and maintaining the data needed, and completing and reviewing the collection of information. Send comments regarding this burden estimate or any other aspect of this collection of information, including suggestions for reducing this burden, to Washington headquarters Services, Directorate for Information Operations and Reports, 1215 Jefferson Davis Highway, Suite 1204, Arlington, VA 22202-4302, and to the Office of Management and Budget, Paperwork Reduction Project (0704-0188) Washington DC 20503.

1. AGENCY USE ONLY *(Leave blank)*	2. REPORT DATE June 1998	3. REPORT TYPE AND DATES COVERED Master's Thesis

4. TITLE AND SUBTITLE
MICROCHEMICAL ANALYSIS OF NON-METALLIC INCLUSIONS IN C-MN STEEL SHIELDED METAL ARC WELDS BY ANALYTICAL TRANSMISSION ELECTRON MICROSCOPY

5. FUNDING NUMBERS

6. AUTHOR(S)
Walters, Jon D.

7. PERFORMING ORGANIZATION NAME(S) AND ADDRESS(ES)
Naval Postgraduate School
Monterey, CA 93943-5000

8. PERFORMING ORGANIZATION REPORT NUMBER

9. SPONSORING / MONITORING AGENCY NAME(S) AND ADDRESS(ES)
Naval Surface Warfare Center, Carderock Division, 9500 McArthur Boulevard, Bethesda, Maryland 20084-5000

10. SPONSORING / MONITORING AGENCY REPORT NUMBER

11. SUPPLEMENTARY NOTES
The views expressed in this thesis are those of the author and do not reflect the official policy or position of the Department of Defense or the U.S. Government.

12a. DISTRIBUTION / AVAILABILITY STATEMENT
Approved for public release; distribution unlimited.

12b. DISTRIBUTION CODE

13. ABSTRACT *(maximum 200 words)*

Microchemical analyses of the inclusions present in several shielded metal-arc steel weld metals were made by analytical transmission electron microscopy (TEM). Low alloy C-Mn steel weld metal samples were studied in which only the titanium and aluminum contents varied significantly. Carbon extraction replicas were made from each of the weldments and the inclusions were analyzed in the TEM by energy dispersive x-ray (EDX) and parallel electron energy loss spectroscopy (PEELS). The results indicated that, for weld metals containing small amounts of Al (13 ppm), the inclusions were comprised of MnO-SiO_2, TiO (maybe as a compound) and $Cu(Mn)S$. As the Al content was increased to 160 ppm, Mn and Si no longer took part in the deoxidization process and the inclusion compositions were dominated by TiO and Al_2O_3 along with some sulfides. For weld metal containing a much higher amount of Al (580 ppm) the inclusions became essentially mixtures of TiO, Al_2O_3 and TiN sometimes complexed with sulfides. These inclusion chemistries were predicted by the use of equilibrium thermodynamics and their effect on the microstructure and mechanical properties of the steel weld metals investigated.

14. SUBJECT TERMS
Shielded Metal Arc Welding, C-Mn Steel Weldments, Non-Metallic Inclusions, Transmission Electron Microscopy

15. NUMBER OF PAGES
156

16. PRICE CODE

17. SECURITY CLASSIFICATION OF REPORT Unclassified	18. SECURITY CLASSIFICATION OF THIS PAGE Unclassified	19. SECURITY CLASSIFI- CATION OF ABSTRACT Unclassified	20. LIMITATION OF ABSTRACT UL

NSN 7540-01-280-5500

Standard Form 298 (Rev. 2-89)
Prescribed by ANSI Std. 239-18

MICROCHEMICAL ANALYSIS OF NON-METALLIC INCLUSIONS IN C-MN STEEL SHIELDED METAL ARC WELDS BY ANALYTICAL TRANSMISSION ELECTRON MICROSCOPY

Jon D. Walters
Lieutenant, United States Navy
B.E., Vanderbilt University, 1990

Submitted in partial fulfillment of the
requirements for the degree of

MASTER OF SCIENCE IN MECHANICAL ENGINEERING

from the

NAVAL POSTGRADUATE SCHOOL
June 1998

ABSTRACT

Microchemical analyses of the inclusions present in several shielded metal-arc steel weld metals were made by analytical transmission electron microscopy (TEM). Low alloy C-Mn steel weld metal samples were studied in which only the titanium and aluminum contents varied significantly. Carbon extraction replicas were made from each of the weldments and the inclusions were analyzed in the TEM by energy dispersive x-ray (EDX) and parallel electron energy loss spectroscopy (PEELS). The results indicated that, for weld metals containing small amounts of Al (13 ppm), the inclusions were comprised of MnO-SiO_2, TiO (maybe as a compound) and $Cu(Mn)S$. As the Al content was increased to 160 ppm, Mn and Si no longer took part in the deoxidization process and the inclusion compositions were dominated by TiO and Al_2O_3 along with some sulfides. For weld metal containing a much higher amount of Al (580 ppm) the inclusions became essentially mixtures of TiO, Al_2O_3 and TiN sometimes complexed with sulfides. These inclusion chemistries were predicted by the use of equilibrium thermodynamics and their effect on the microstructure and mechanical properties of the steel weld metals investigated.

TABLE OF CONTENTS

x

ACKNOWLEDGMENT

I would like to express my sincere gratitude and appreciation to Dr. Alan G. Fox for his enthusiasm and guidance in completing this research.

Special acknowledgment is due to Dr. Sarath Menon, Dr. Martin Sanders and Mr. Richard Hashimoto, for their contribution of many hours of laboratory assistance.

Finally I would like to thank my parents and family who provided the most important things of all, love and support.

I.   INTRODUCTION

Welding research is vitally significant to the United States Navy. The materials that fabricate modern day warships must withstand the rigorous requirements of operating for many years in multiple missions and environmental conditions. This dynamic life cycle subjects the ship's structure to a multitude of stresses, each having the ability to cause material failure. Such failures often occur at weld joints due to the high stress concentrations which form between the steel base plates.

The Naval Surface Warfare Center (NSWC), Carderock Division, Bethesda, MD, in conjunction with the Naval Postgraduate School have undertaken an aggressive research and development program to analyze, predict and strengthen steel weldments used in ship and submarine construction. The most difficult research to conduct is microanalysis which greatly helps to develop better understanding into the complex microstructural characteristics of a weldment. This type of analysis eventually leads to engineering advances that produce stronger and more cost effective welds.

As a weld deposit cools to room temperature, different microstructures form within the weld pool such as grain boundary ferrite, side plate ferrite, acicular ferrite, bainite, and martensite. In addition, deoxidizing elements from the flux and/or weld wire, such as aluminum, titanium, silicon and manganese, react with oxygen, sulfur and sometimes nitrogen in the molten weld pool to form small non-metallic inclusions. The chemical composition, size and distribution of these non-metallic inclusions influence the formation of microstructures and impact the mechanical properties of the weld. Previous

1

research has shown that the microstructure which is most effective for strengthening and toughening ferritic steel weld metal is acicular ferrite. This finely woven microconstituent severely restricts crack propagation and thus helps prevent material failure. Small non-metallic inclusions nucleate acicular ferrite, but the chemistry and composition of these inclusions and how they nucleate acicular ferrite have not yet been determined in detail.

The objective of this research is to further analyze the microchemical composition and formation of non-metallic inclusions in C-Mn steel Shielded Metal Arc Welds (SMAW). Inclusions from three samples were studied. Each sample contained varying amounts of titanium and aluminum. Energy dispersive x-ray spectroscopy (EDX) and parallel energy loss spectroscopy (PEELS) were conducted and compared on the inclusions through the use of the transmission electron microscope (TEM). This research helped advance the understanding of the formation, chemistry and complex microstructure of non-metallic inclusions.

II. BACKGROUND

A. SHIELDED METAL ARC WELDING

SMA welding is one of the oldest and most versatile of all fusion welding processes. This process is simple, relatively inexpensive and can be performed above or below water. The United States Navy uses SMA welding in many applications including deck/hull maintenance, structural and damage control repair. Figure 2.1 provides a sketch of the SMA welding process. In SMA, also known as "covered electrode" welding, an electric arc is established between a manually fed consumable electrode and the base metal [Ref. 1]. The electrode consists of an inner filler metal covered by an extruded layer of flux. To remove excess water from the outer covering, the rods are usually baked forming a hard outer shell. This reduces the hydrogen content of the rod which helps prevent hydrogen cracking in the weld deposit. The flux covering may account for up to half of the composition of the electrode and serves the following functions [Ref. 1, 2]:

- Provides alloying elements for the weld pool.

- Forms a gaseous shield to protect the molten weld pool from the environment.

- Controls the atmosphere, arc stability, and bead contour.

- Contains elements that help deoxidize and remove impurities from the weld pool.

- Produces a slag layer that protects the weld bead upon solidification and cooling.
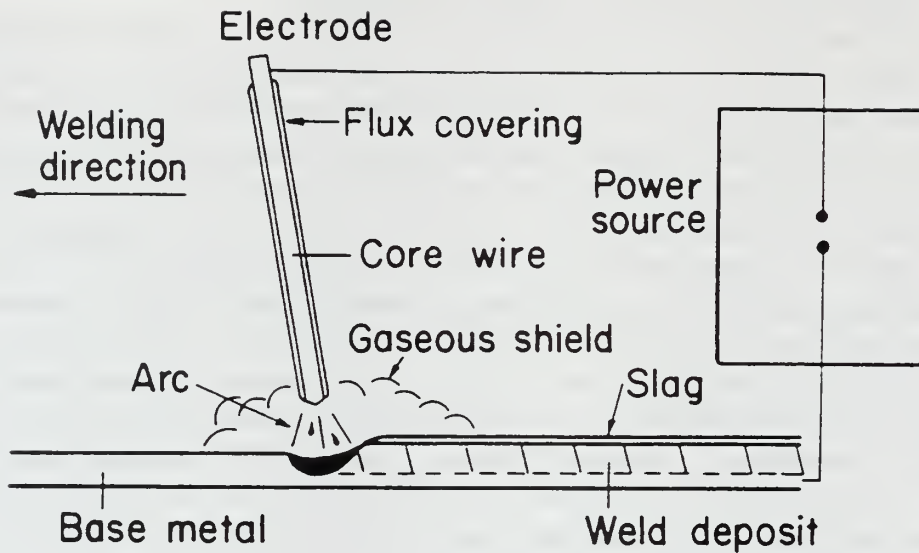
Figure 2.1   SMA welding process [From Ref. 2]

B.   WELD METAL MICROSTRUCTURE

1.   Microstructure Identification

As the weld deposit cools, multiple microstructures can form as shown in the schematic continuous cooling transformation (CCT) diagram Figure 2.2. The microstructures that develop are determined by the cooling rate, alloying element and oxygen content of the weld metal [Ref. 2]. Any changes in cover gas composition, welding speed, or power density will influence the microstructure and affect the mechanical properties of the weld.
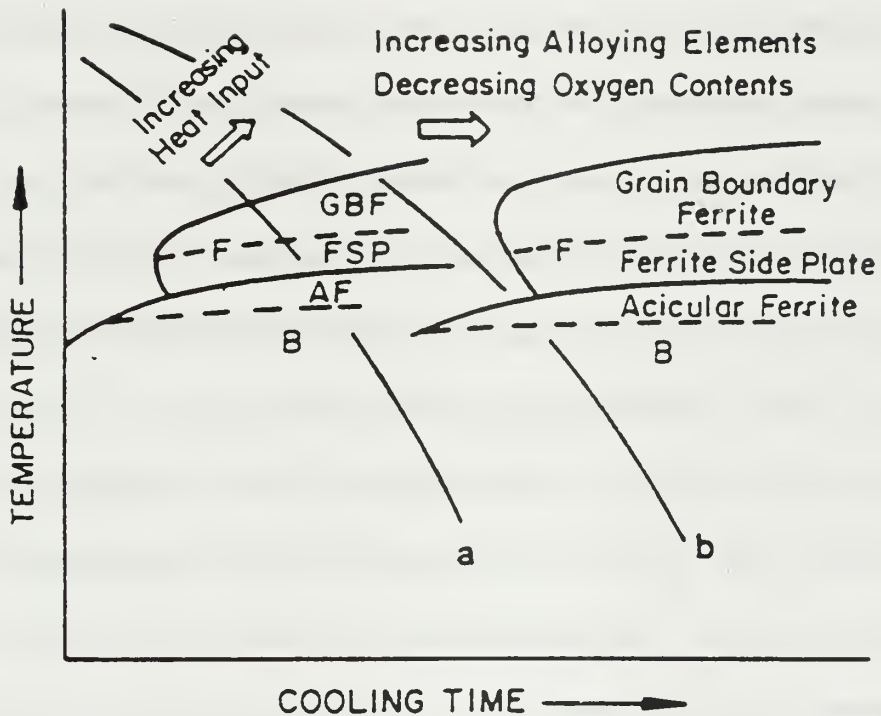
Figure 2.2   CCT Diagram for the weld metal of low-carbon,
low-alloy steels [From Ref. 2]

To assist material scientists in microstructure identification, the International

Welding Society established the guidelines for the optical classification of the major

microstructural constituents found in ferritic steel weld metals [Ref. 3]. The guidelines

define the following weld metal microstructures.

a. *Primary Ferrite (PF)*

Primary ferrite is the first microstructure that forms as the weld deposit cools from austenite. It is a diffusion controlled reaction that occurs at high temperatures at slow cooling rates. Primary ferrite includes both grain boundary (Allotriomorphic) ferrite and intragranular polygonal ferrite. Grain boundary ferrite transforms at the austenite grain boundaries in the form of veins or polygonal grains. Intragranular polygonal ferrite forms within existing prior austenite grains. These ferrite morphologies are larger than the surrounding acicular ferrite (AF) and ferrite with second phase (FS).

b. *Ferrite with Second Phase (FS)*

Ferrite with second phase includes both ferrite with aligned and non-aligned second phase. Aligned second phases are side plate (Widmanstätten) Ferrite, upper and lower bainite. Side plate ferrite forms at a slightly lower temperature than proeutectoid ferrite at a faster cooling rate. It nucleates by a displacive mechanism on the ferrite-austenite grain boundaries [Ref. 4], producing coarse parallel ferritic plates formed perpendicular to the grain boundary. Bainite forms at a lower temperature than acicular ferrite at a rapid cooling rate. It nucleates on austenite grain boundaries producing fine needlelike plates consisting of sheaves of ferrite with cementite forming between them [Ref. 5, 6]. Upper bainite forms at higher temperatures and produces a sheaf-like microstructure and lower bainite forms at lower temperatures producing a finer microstructure [Ref. 6]. The cementite surrounding the ferrite sheaves can form a brittle crack propagation path which reduces the toughness of the weld. Non-aligned second phase comprises the microstructures surrounding the laths of acicular ferrite.

c.   *Acicular Ferrite (AF)*

Acicular ferrite forms within prior austenite grains in an interlocking basket-weave pattern which strongly resists crack propagation. It forms at temperatures below primary ferrite at faster cooling rates. Acicular ferrite forms through a displacive-diffusion reaction but unlike side plate ferrite, acicular ferrite nucleates on inclusions as opposed to grain boundaries and forms in isolated laths with a high aspect ratio [Ref. 7, 8, 9]. Acicular ferrite is the most desired microconstituent due its ability to improve both strength and toughness. This microstructure increases the number of times a propagating crack will encounter an interface and be required to change direction in order to continue in its irregular fracture path. Figure 2.3 illustrates the crack propagation behavior for three different morphologies including acicular ferrite.

d.   *Ferrite Carbide Aggregate (FC)*

Ferrite carbide aggregate consists of ferrite with interphase carbides included in the morphology and the microstructure pearlite. Pearlite nucleates from austenite and is comprised of ferrite and cementite (Fe_3C) phases producing alternating layers known as lamellae. It forms at high temperatures and long cooling rates. Thin layers of cementite and thick layers of ferrite form simultaneously during the transformation due to carbon diffusion [Ref. 5].

e.   *Martensite (M)*

Martensite is a hard and brittle microstructure supersaturated with carbon. It forms from austenite during rapid cooling rates when carbon diffusion is minimal. The martensitic microstructure consists of long needle-shaped grains surrounded by austenite

that failed to transform to ferrite due to the rapid cooling rate [Ref. 5]. It may also form between ferrite laths from excess carbon enriched areas found in the austenite. Martensite grains form in colonies with similar crystal orientation providing an easy path for crack propagation as shown in Figure 2.3.
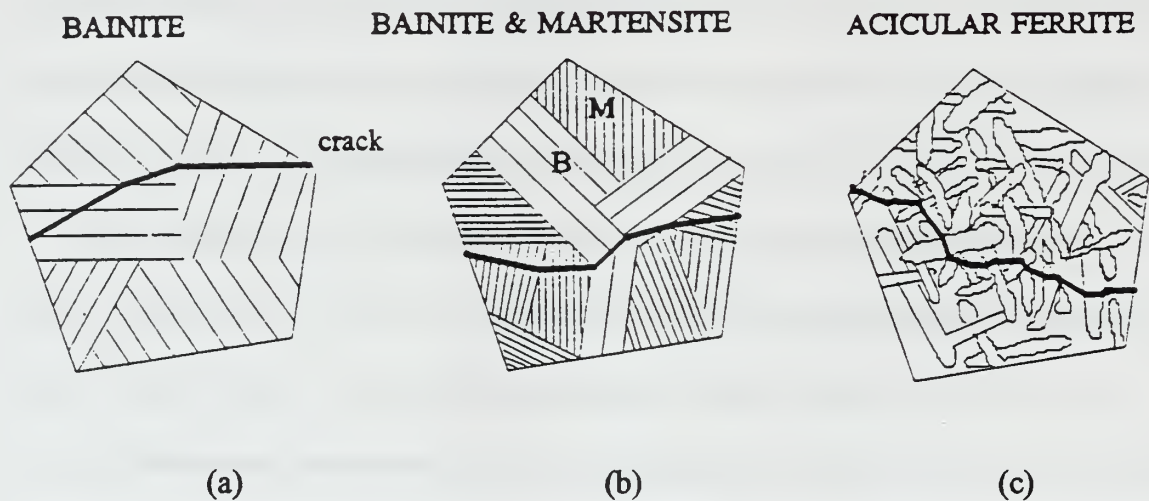

Figure 2.3   Schematic diagrams: a) cleavage crack deflection at colony boundaries; b) austenite grains subdivided by bainite; c) cleavage crack deflection at lath boundaries [From Ref. 10, 11]

2.   Weld Deposit Microstructure Zones

The microstructure of a low carbon steel weld can be divided into three zones; the Fusion Zone (FZ), the Heat Affected Zone (HAZ), and the Base Metal. The HAZ can be

8

further divided into three distinct regions: Grain Coarsening (GC), Grain refining (GR), and Partial Grain Refining (PGR) regions. [Ref. 2]

The Fusion Zone (FZ) forms from the solidification the weld deposit. Here the molten metal is in contact with the unmelted part of the base metal or previous weld known as the substrate. Thermal gradients are established and solidification occurs by epitaxial nucleation of δ-ferrite. These grains initiate at the substrate and proceed inward toward the fusion zone center [Ref. 2]. As the temperature decreases, austenite (γ) becomes more thermodynamically favorable and nucleates at the newly formed δ-ferrite grain boundaries. The resultant microstructure consists of coarse columnar grains which are brittle and susceptible to cracking. Increasing the heat input during the welding process can reduce the grain size and strengthen the zone [Ref. 2]. During this solidification, large inclusions tend to be pushed along the grain boundaries while small inclusions are enveloped by the grain [Ref. 12].

The HAZ Partial Grain-Refining region is formed when a sufficient temperature is reached in order to re-austenitize the prior pearlite colonies in the region and expand them slightly into prior ferrite colonies. During cooling, the grains decompose into small pearlite and ferrite grains producing a microstructure stronger than the base metal. [Ref. 2]

The HAZ Grain Refining region is formed when a sufficient temperature is reached to allow austenite grains to nucleate but not coarsen [Ref. 2]. This region produces the toughest microstructure in the weldment due to the very small prior austenite grains.

The HAZ Grain Coarsening region is formed when a sufficient temperature is reached to allow austenite grains to nucleate and coarsen [Ref. 2]. This region produces grains larger than the grain refining region, but still smaller than that found in the fusion zone.

The Base Metal Zone is the part of the weldment in which the heat produced from the weld process does not effect the microstructure.

The zones and regions discussed above are diagrammed for a single-pass and multipass weldment in Figure 2.4 and Figure 2.5. Individual CCT curves for the fusion zone and HAZ regions are shown in Figure 2.6.
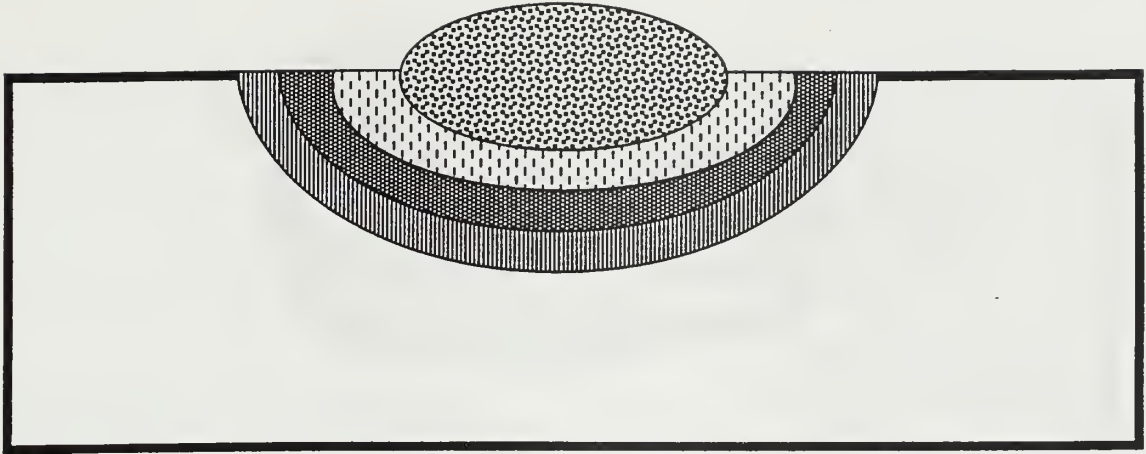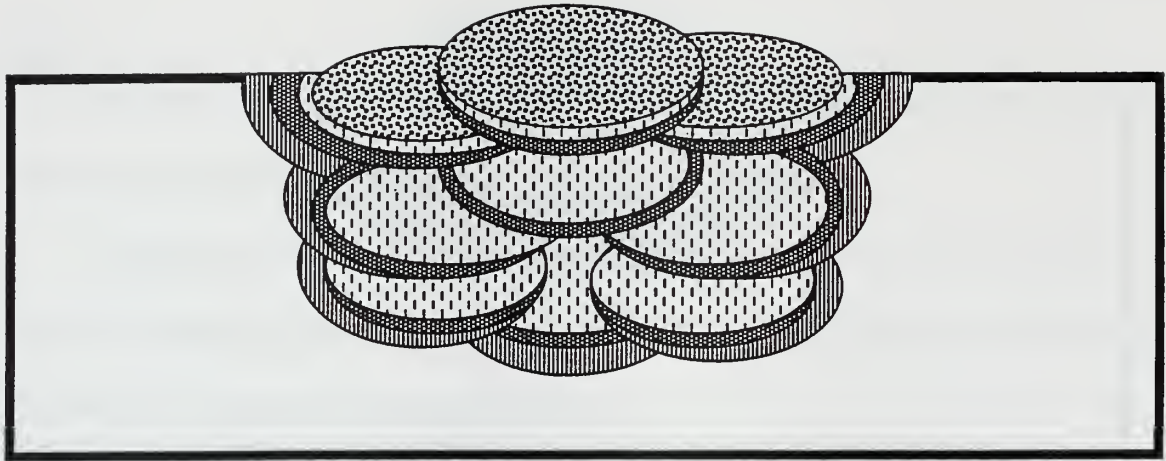
FZ - Columnar Grains

HAZ - Coarse Grains

HAZ - Small Grains

HAZ - Partial Refined Grains

Base Metal

Figure 2.4   Single-pass weld deposit diagram

FZ - Columnar Grains

HAZ - Coarse Grains

HAZ - Small Grains

HAZ - Partial Refined Grains

Base Metal

Figure 2.5   Multi-pass weld deposit diagram
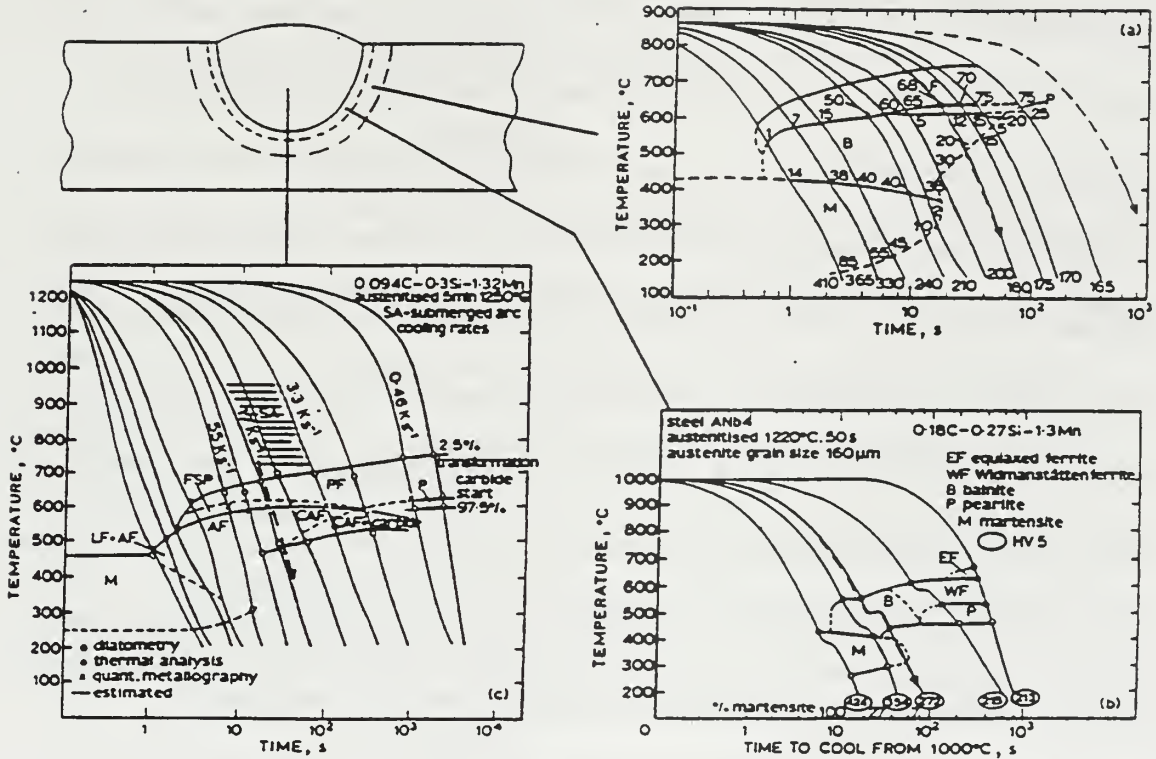
12

Figure 2.6   CCT curves for various regions of a weld deposit [From Ref. 9]

C.   NON-METALLIC INCLUSIONS AND DEOXIDATION

1.   Non-Metallic Inclusions

Welded steel consists of a metallic matrix in which non-metallic inclusions co-exist. These particles are formed by the interaction of oxygen, nitrogen, and/or sulfur present in the cover gas and flux, with the alloying elements in the weld pool. Inclusions are classified as either indigenous or exogenous. Indigenous inclusions occur as a result of homogeneous reactions during solidification and form as oxides, sulfides and/or nitrides. Exogenous inclusions result from impurities such as refractories and slag trapped in the molten weld. These inclusions are usually large and can be detrimental to the weld metal toughness. The inclusion shape, size, distribution and morphology can have a beneficial or adverse effect on the strength and toughness of the weld. Inclusions of less than 2 μm in size can improve the toughness of the weld by pinning and restricting grain growth and also by providing nucleation sites for acicular ferrite [Ref. 13]. Inclusions larger than 2 μm in diameter can initiate ductile and brittle fracture by acting as crack or micro-void initiation sites.

2.   Deoxidation of Steel Weld Metals

Deoxidizing elements are normally added to the fluxing agent or consumable weld wire. Deoxidizers reduce the amount of oxygen which improves the toughness of the weld [Ref. 2]. There are three reasons deoxidizers improve toughness. First, the removal of oxygen helps prevent the formation of brittle FeO oxides [Ref. 2]. Deoxidizing

14

elements such as aluminum, titanium, silicon, and manganese have a free energy of oxide

formation lower than that of FeO as shown in Figure 2.7. Second, the removed oxygen

helps prevent the formation of carbon monoxide which can lead to weld porosity during

the solidification process [Ref. 2]. Third, as mentioned previously, small non-metallic

inclusions can act as nucleation sites which promote the formation of acicular ferrite [Ref.

13]. The most common deoxidizers are discussed below.

a. *Aluminum*

Aluminum is the strongest and most effective deoxidizing agent of

the weld metal alloying elements. Aluminum reacts with oxygen to form Al_2O_3. Because

aluminum removes such a large amount of oxygen, Al_2O_3 is usually found in high

concentrations in inclusions if aluminum is present in significant quantities in the weld

pool. Pervious research has shown that aluminum oxides are aciclular ferrite nucleators

[Ref. 14, 15]. Aluminum also improves toughness by forming aluminum nitrides which

pin the weld metal prior austenite grain boundaries and thus refine the grain size [Ref. 16].

b. *Titanium*

Titanium is the second strongest deoxidizer found in weld deposits.

Titanium-containing inclusions have also been found to promote the nucleation of acicular

ferrite formation [Ref. 17]. There is much controversy over the formation of titanium

oxides. Research has suggested that different forms can occur including TiO [Ref. 15],

TiO_2 [Ref. 18], and Ti_2O_3 [Ref. 19]. TiN inclusions can also form when the level of

oxygen in the weld deposit is low after Al_2O_3 deoxidation [Ref. 20]. These comments

suggest that the form of the titanium oxides and/or nitrides depends critically on the weld

15

metal chemical composition particularly with respect to oxygen, nitrogen, aluminum and titanium.

c.   *Silicon*

Silicon is a weak deoxidizer and forms SiO_2. SiO_2 has not been shown to be as strong an acicular ferrite nucleator as aluminum and titanium oxides [Ref. 21]. In addition silicon can have a detrimental effect on the toughness of the weld if it is found in concentrations greater than 0.5% [Ref. 22].

d.   *Manganese*

Manganese is also a weak deoxidizer which forms MnO and complex oxides such as $MnO.SiO_2$ and $MnO.Al_2O_3$. Manganese can promote the nucleation of acicular ferrite and does so at the expense of grain boundary ferrite [Ref. 22]. Manganese also reacts with sulfur to produce MnS as opposed to FeS. Unlike FeS which "wets" grain boundaries, MnS has a more globular morphology which limits solidification cracking at grain boundaries therefore increasing toughness [Ref. 2, 18].
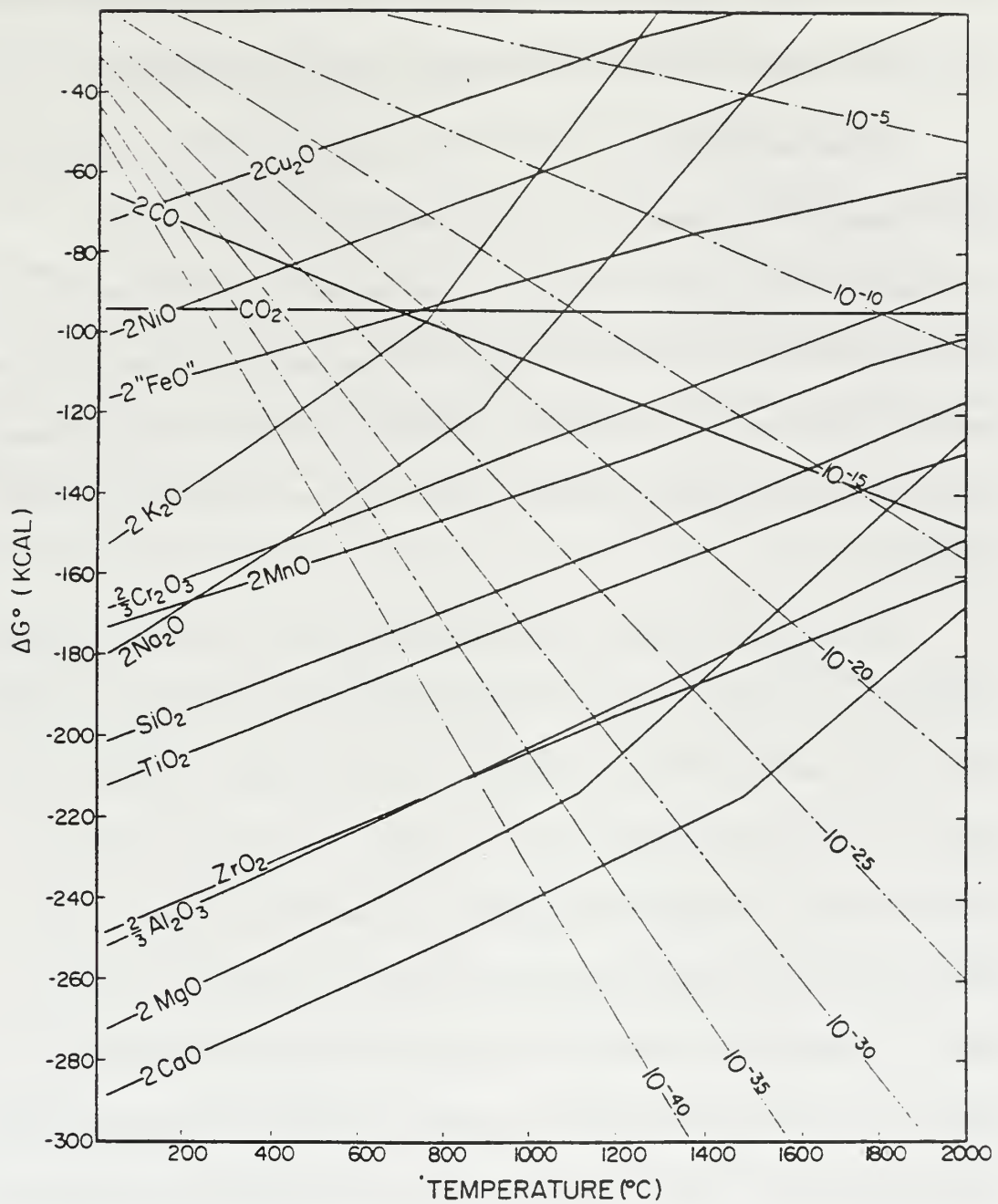
Figure 2.7   Free energy of formation of oxides [From Ref. 23]

17

D. PREVIOUS CHEMICAL AND COMPOSITION ANALYSIS OF INCLUSIONS BELIEVED TO FORM ACICULAR FERRITE

A substantial amount of research has been conducted on the crystal structure and microchemistry of non-metallic inclusions. The majority of analyses have been accomplished through analytical modeling, energy dispersive x-ray (EDX) and electron diffraction performed with transmission electron microscopes (TEM). The results have been inconclusive, and the exact chemistry and formation reactions of these inclusions and why acicular ferrite nucleation is favored for certain inclusion compositions is not fully understood.

Four possible mechanisms for acicular ferrite nucleation on inclusions have been outlined in recent reviews by Fox et al. [Ref. 24], Bhadesia [Ref. 25], Grong et al. [Ref. 20] and Zhang and Farrar [Ref. 26]. These are: i) simple nucleation of ferrite on an inert substrate, ii) epitaxial growth of the ferrite on a suitably oriented facet in the inclusions (lattice matching), iii) nucleation occurring from the strain energy associated with the difference between the thermal expansion coefficients of the inclusions and the steel matrix, iv) chemical effects which lower the hardenability in the steel surrounding the inclusion. Due to the multitude of oxides and oxide compounds (and sometimes nitrides and sulfides) that can be found in the inclusions and the thermodynamics and kinetics that govern their formation, it is very difficult to predict the complex chemistry of the phases present in inclusions.

Babu et al. [Ref. 14] shed some light on the problem by developing empirical formulae to produce time temperature transformation and nucleation rate curves from

which inclusion deoxidizing reactions could be predicted. Figures 2.8 and 2.9 show one of the TTT and nucleation rate curves of various oxides produced for a given steel weldment. The diagrams showed strong correlation between published inclusion compositions and stability of oxides, but the theory is based on the assumption of constant weld metal composition. Since the weldment is always cooling, continuous reactions occur in the inclusions and this is not modeled. Babu et al. concluded that $MnO.Al_2O_3$ (galaxite), Al_2O_3, TiO_2, Ti_3O_5, SiO_2 and MnO as inclusion constituents were likely to be responsible for acicular ferrite nucleation and the sequence of oxide formation in the nonmetallic inclusions to be Al_2O_3, $MnO.Al_2O_3$, Ti_3O_5, $FeO.Al_2O_3$, TiO_2, SiO_2, and MnO in the C-Mn steels they studied. Also discussed was the layered effect observed in inclusions due to subsequent deoxidization (desulfurization) reactions and heterogeneous nucleation. Figure 2.10 shows a theoretical schematic of a layered inclusion. [Ref. 14]
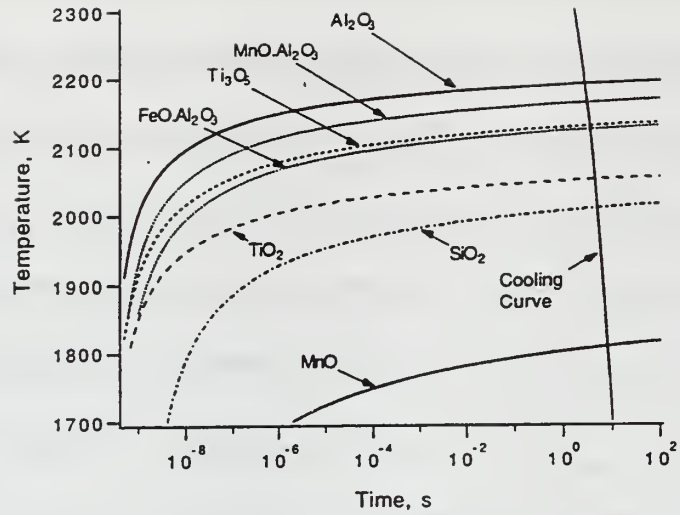
Figure 2.8   TTT curve generated using extent of reaction equations
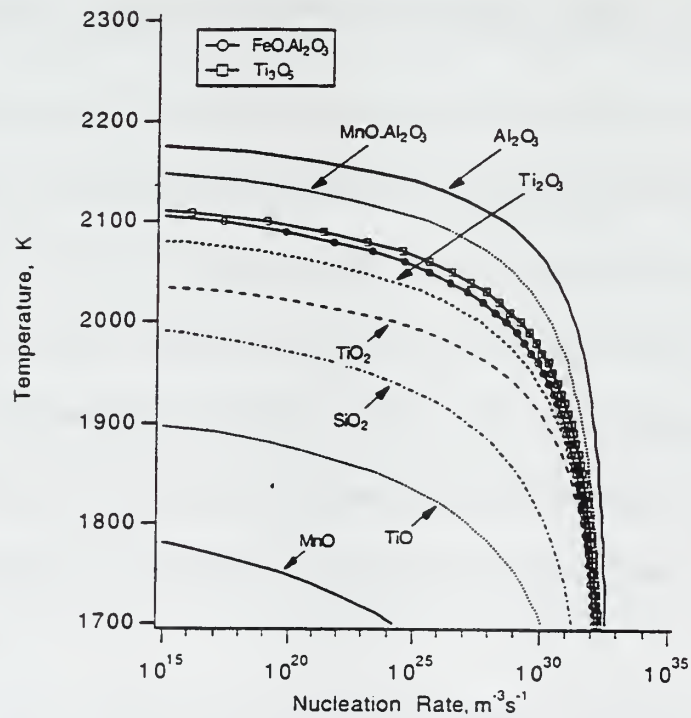[From Ref. 14]

Figure 2.9   Nucleation rate curve generated using extent of reaction equations [From
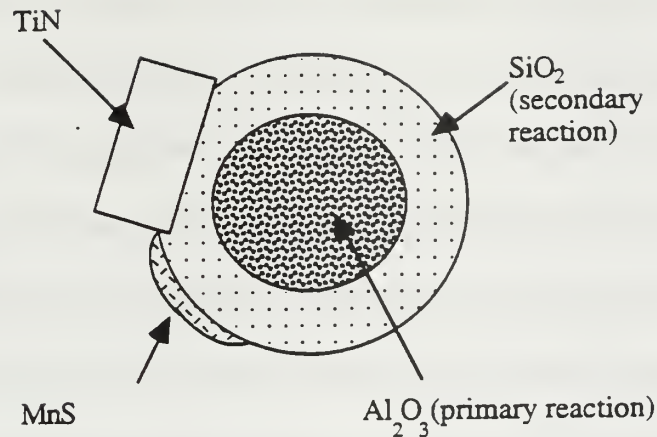Ref. 14]

Figure 2.10   Theoretical schematic of a layered inclusion [From Ref. 14]

$MnO.Al_2O_3$ may be responsible for acicular ferrite nucleation and Fox and

Brothers [Ref. 27] suggest that, in addition to $MnO. Al_2O_3$ that $MnO.TiO_2$ (pyrophanite)

may be an acicular ferrite nucleator as well. Gregg and Bhadesia [Ref. 28], however,

indicate that this may not be correct and that $MnO.Al_2O_3$ may not form acicular ferrite on

its own.

When aluminum and titanium contents are low, MnO and $MnO.SiO_2$ (Rhodonite)

form as the primary reaction products in the inclusions. This is shown on the ternary

phase diagram illustrated in Figure 2.11. As the aluminum content increases other

compounds can form such as $3MnO.Al_2O_3.3SiO_2$ (Spessartite) and $MnO.Al_2O_3.2SiO_2$

(Mn-Anorthite) with Al_2O_3 or $MnO.Al_2O_3$ possibly forming if aluminum contents are

21

higher. If titanium is present the resulting compositions could be combinations of Al_2O_3-TiO-MnO or Al_2O_3-TiO-MnO.SiO_2. Unfortunately there are no quarternary diagrams in the literature representing these compounds [Ref. 29]. As mentioned earlier, titanium has been reported to form as TiO [Ref. 15], TiO_2 [Ref. 18], and Ti_2O_3 [Ref. 19] and this further complicates the problem. Titanium oxides have been shown to promote acicular ferrite formation [Ref. 13] as well as TiN [Ref. 20]. Green [Ref. 30] found it difficult to differentiate between TiO and TiO_2 in titanium rich inclusions in C-Mn steels using analytical transmission electron microscopy (TEM) but showed that as little as 28 ppm titanium in aluminum free C-Mn steel can promote considerable acicular ferrite growth. Figure 2.12 shows such an inclusion. Blais et al. [Ref. 31] conducted analytical (TEM) and diffraction on similar samples to those studied by Greene and found TiO (fcc structure) on the surface of the inclusion which they felt would be responsible for acicular ferrite nucleation.

Zhang and Farrar [Ref. 26] generated energy dispersive x-ray analysis in the TEM from carbon extraction replicas obtained from several low alloy steels. They concluded that TiO, Al_2O_3, SiO_2, MnO-SiO_2, TiO (Al_2O_3)-MnO-SiO_2, MnS and CuS can all nucleate acicular ferrite. They claim that this occurs because the inclusions act as substrates which lower the free energy barrier to the ferrite nucleation and that lattice matching, strain and chemical effects are less important. Zhang and Farrar then went on to claim that weld metals in which the formation of acicular ferrite was subdued arose because the prior austenite grain size was reduced by the presence of small inclusions (< 0.2 μm). This smaller grain size naturally leads to increased amounts of grain boundary nucleated

22

microconstituents such as bainite. In addition, low aluminum to oxygen ratios appear to increase the amount of acicular ferrite formation while high aluminum to oxygen ratios suppress its formation. This is thought to occur due to the soluble aluminum content which promotes sideplate ferrite formation. Both Zhang and Farrar and Bhadesia [Ref. 25] discuss this possibility. Zhang and Farrar's discussion does not point out the considerable circumstantial evidence that titanium-containing inclusions are very effective in promoting acicular ferrite over other inclusions and that all inclusions are not alike. In addition Zhang and Farrar did not think epitaxy was important but Grong et al. [Ref. 20] have clearly shown that epitaxial nucleation of acicular ferrite can occur on δ-Al_2O_3 and TiN (fcc structure) inclusions.
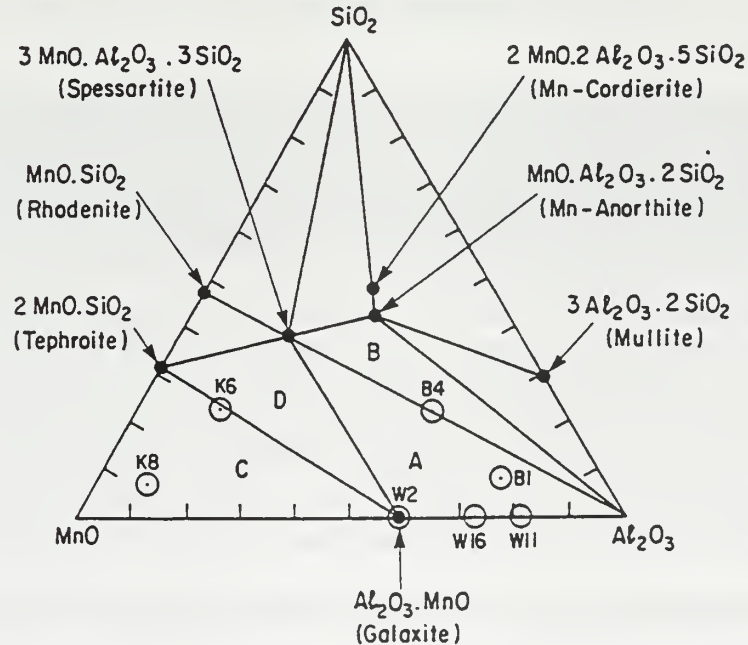

Figure 2.11   Ternary Diagram of Coexisting Phases in Annealed Mixes for the System Al_2O_3-MnO-SiO_2 [From Ref. 29]
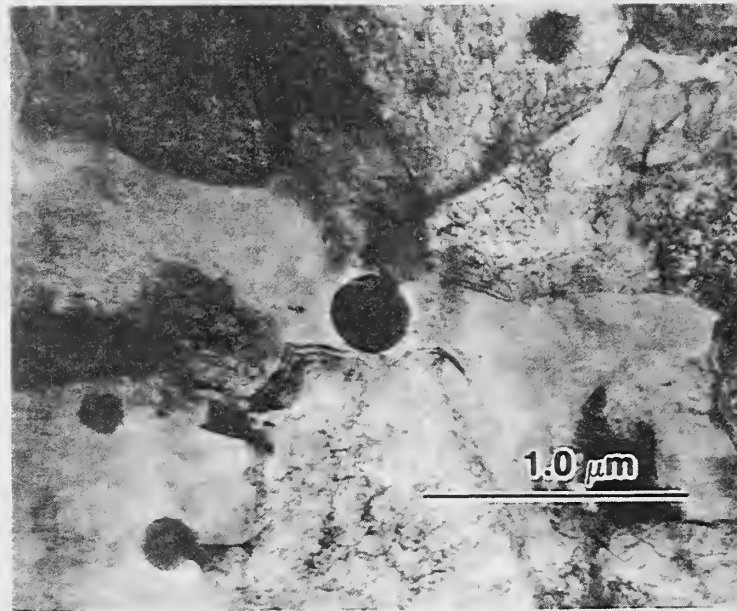
Figure 2.12   Multiple nucleation of acicular ferrite on an inclusion in a C-Mn steel weld metal containing 28 ppm titanium [From Ref. 30]

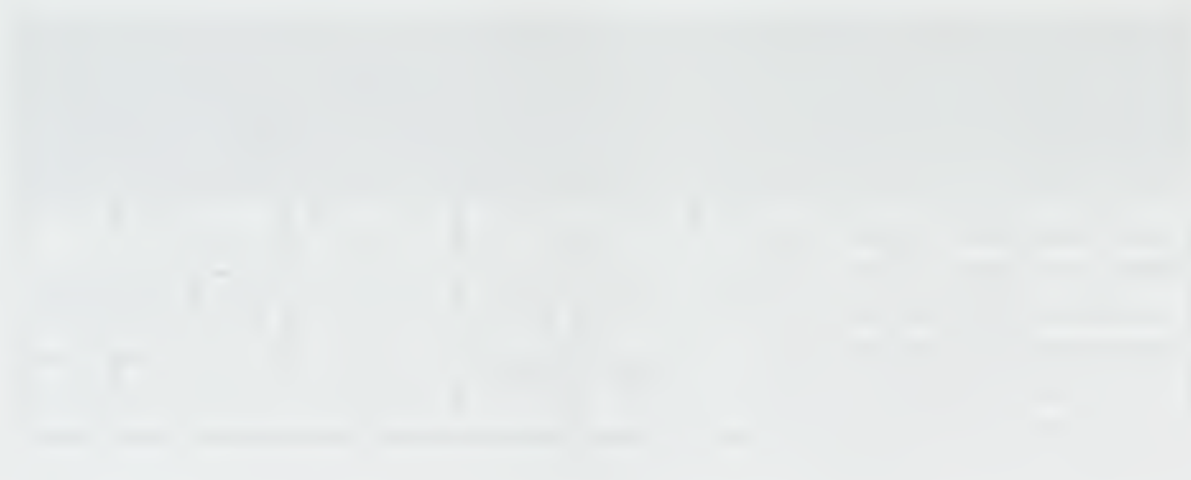## E.   SCOPE OF THE PRESENT WORK

The above discussion shows that welding metallurgy is a complex science and that the exact nature and chemical composition of the inclusions responsible for the nucleation of acicular ferrite is not yet fully understood. The ultimate objective of this research is to further the knowledge of the microchemical and structural composition of such inclusions in C-Mn steel SMA weldments. A detailed examination of the microstructure and inclusions in the final weld pass of three samples was conducted. The samples final weld

pass chemical compositions were provided by Dr. G. M. Evans [Ref. 32] and are shown in Table 1.1. For this study only the titanium and aluminum contents varied significantly as the primary deoxidants which allowed for a more definitive analysis to be conducted. The experiments were conducted in a TOPCON 002B transmission electron microscope (TEM) equipped with an EDAX energy dispersive x-ray (EDX) spectrometer and a Gatan parallel electron energy loss spectroscopy (PEELS) imaging filter. Previous work has primarily analyzed non-metallic inclusions using only EDX and modeling. This study extends the inclusion research to in-depth PEELS microanalysis and mapping which can better "fingerprint" the exact chemical composition. The PEELS data is then compared to the EDX data from the same inclusions.

SAMPLE	C	Mn	Si	S	P	Ti	B	Al	N	O
	%					ppm				
Y	0.070	1.57	0.45	0.006	0.010	390	39	13	83	308
Z	0.072	1.56	0.49	0.007	0.010	420	48	160	67	438
V	0.078	1.44	0.60	0.006	0.007	540	56	580	41	336

Table 1.1   Chemical composition of the C-Mn steels studied in the present work

III.   EXPERIMENTAL PROCEDURE

A.   WELD SAMPLES

The SMA welding samples were prepared by Dr. G. M. Evans at Oerlikon Welding Limited, Zurich, Switzerland. Weld sample preparation outlined here is covered in detail in Ref. 32 and 33.

1.   Electrodes

Increasing amounts of titanium and aluminum metal power were added to the coatings of three basic low hydrogen electrodes in order to obtain weld metal levels of 390 ppm Ti and 13 ppm Al (Sample Y), 420 ppm Ti and 160 ppm Al (Sample Z) and 540 ppm Ti and 580 ppm Al (Sample V). The experimental electrodes were then extruded onto 4 mm diameter core wire. The coating factor (D/d) of 1.68 was used.

2.   Weld Preparation

Two 20 mm thick plates were welded as specified in ISO 2560-1973. Twenty-seven shielded metal arc welds were required to fill the joint. Each weld was performed in the flat position with approximately three beads per layer. The interpass temperature was maintained at 200°C. Direct current (electrode positive) of 170 A was used with a voltage of 21 volts and a nominal heat-input of 1 kJ/mm.

3. Mechanical Testing

Tensile specimens consisting of only weld metal from each deposit were machined and then tested. In addition, approximately thirty-five centrally located Charpy-V notch specimens were tested to obtain a full transition temperature curve.

4. Metallography

Weld samples were cut into transverse sections and optical examination was conducted on the top beads and adjacent intercritically reheated zones.

B. SAMPLE PREPARATION

The three weld samples were cut into ¾" transverse pieces for analysis. Grinding was conducted on the Struers Knuth Rotor-3 and Buehler Ecomet-4 polishers using 180, 220, 320, 500, 1000, and 2400 grit Struers and Buehler waterproof silicon carbide paper. The samples were further polishing using 3 μm followed by 1 μm diamond compound on Buehler Microcloth.

C. OPTICAL MICROSCOPY

The weld samples were deep etched with 5% nitric acid and 95% methanol (nital) for a period of 1 minute. The deep etch was performed to reveal surface relief corresponding to the weld deposit microstructure zones. Macrophotographs were

then taken by GRM Custom Photographic Lab, Monterey CA, using a 6X macro lens on a mounted 35 mm camera. Samples were then repolished and lightly etched for 10 seconds with the nital solution. The light etch revealed microstructural features such as acicular ferrite (AF) and ferrite with second phase (FS). Micrographs were taken on a Zeiss Jenaphot 2000 optical photomicroscope with an attached Pulnix TMC-74 optical camera. The camera was connected to a 486/DX2 computer and Semicaps photo analysis software was used to process the digital photographs.

D.   TRANSMISSION ELECTRON MICROSCOPY (TEM)

The non-metallic inclusions were analyzed using a transmission electron microscope (TEM) with energy dispersive x-ray (EDX) and parallel electron energy loss spectroscopy (PEELS) microanalysis. The TEM is the most effective tool to investigate the chemical composition and morphology of steel weld metal inclusions. Carbon extraction replicas were prepared and initial observation was performed on a JEOL JEM-100 CX II TEM with a LaB_6 filament energized to 120,000 volts. Final imaging, EDX and PEELS analysis was performed on a TOPCON 002B TEM with LaB6 filament energized to 200,000 volts shown in Figure 3.1.

Figure 3.1   TOPCON 002B TEM at the Naval Postgraduate School

30

1. Carbon Extraction Replicas

TEM samples were prepared in the form of carbon extraction replicas. The three weld samples were repolished as outlined earlier, and the transverse face of each was etched in a solution of 5% nitric acid and 95% methanol (nital) for twenty seconds. Each sample was masked to expose only the area of the final weld pass. Two strands of carbon fiber were wound into a filament and stretched between the electrodes of an Ernest F. Fullan Mk II carbon coater. Samples were then individually placed in the vacuum chamber of the coater at a distance of 3.1 cm from the carbon filament. The chamber was evacuated and a current was applied depositing a thin layer of carbon onto each sample. The carbon deposition process was repeated until a bluish-gold carbon film was achieved representing a thickness of approximately 20 nm. Coated samples were scribed into 3 mm squares and then deep etched in the nital solution until the regions floated off the sample or peeled partially from the surface. The carbon extraction replicas, containing the non-metallic inclusions, were then gently lifted from the Nital solution and placed into a 5% acetone water bath which flattened the replicas due to surface tension effects. The flattened foils were removed from the mixture using small 400 mesh nickel grids. Due to possible CuS formations in the inclusions, nickel grids were chosen instead of copper grids. Figure 3.2 outlines the steps of the procedure.
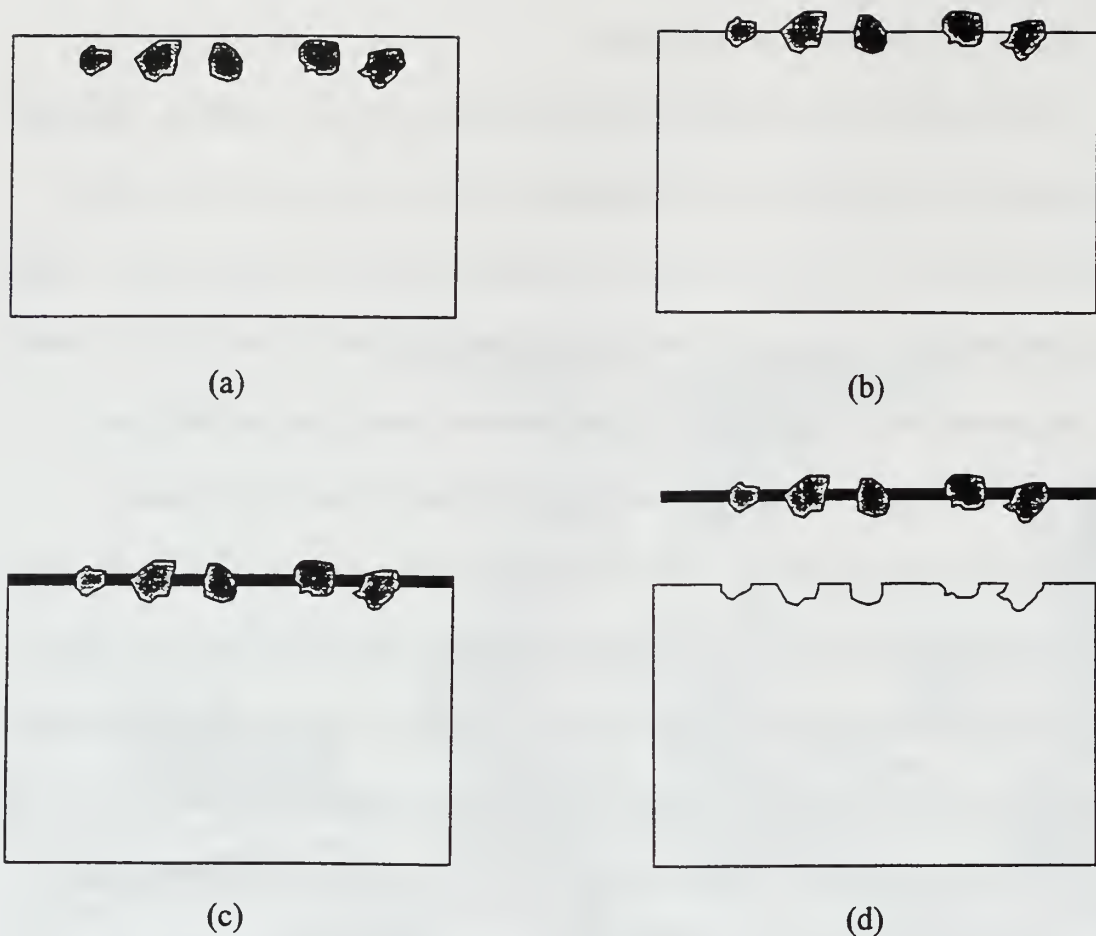
Figure 3.2   Steps in obtaining a carbon extraction replica: a) Polished sample; b) Etched sample; c) Carbon coated sample; d) Carbon extraction replica separation.

2.   TEM Overview

Transmission electron microscopes allow imaging at very high magnifications in excess of 1,000,000X. In addition microchemical analysis can be performed through the use of EDX and PEELS. TEMs allow high resolution images of very small samples because accelerated electrons have a short wavelength. The TOPCON 002B, for

example, has a 0.18 nm spatial resolution and a usable electron probe diameter of 5 nm for

EDX and 1 nm for PEELS. The TEM consists of an electron gun and an assembly of

magnetic condenser lenses enclosed in an evacuated column. This is shown schematically

in Figure 3.3. The vacuum keeps the electrons from being scattered by air molecules. The

condenser lenses collimate the electron beam and illuminate the sample placed between the

objective lenses. The sample image is then magnified by additional lenses and projected

onto a fluorescent viewing screen. The image can then be observed or photographed by a

recording system located below the viewing screen. [Ref. 34]
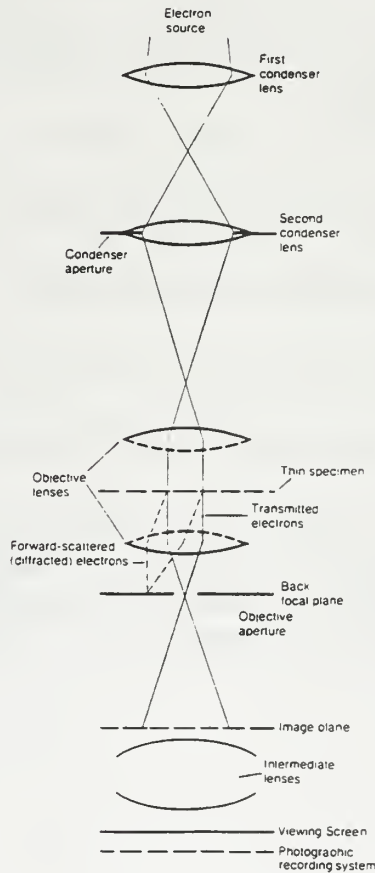
Figure 3.3   The electron optical system of a TEM [From Ref. 35]

3. Interactions of Electron with Matter

Electrons are classified as ionizing radiation because they are capable of striking an atom and removing tightly bound inner-shell electrons to a higher energy level [Ref. 35]. When ionizing radiation hits a sample it produces secondary emissions as shown in Figure 3.4. These emissions include backscattered electrons, x-rays, secondary electrons and Auger electrons all of which can be measured or counted so as to analyze the chemistry and composition of the sample.
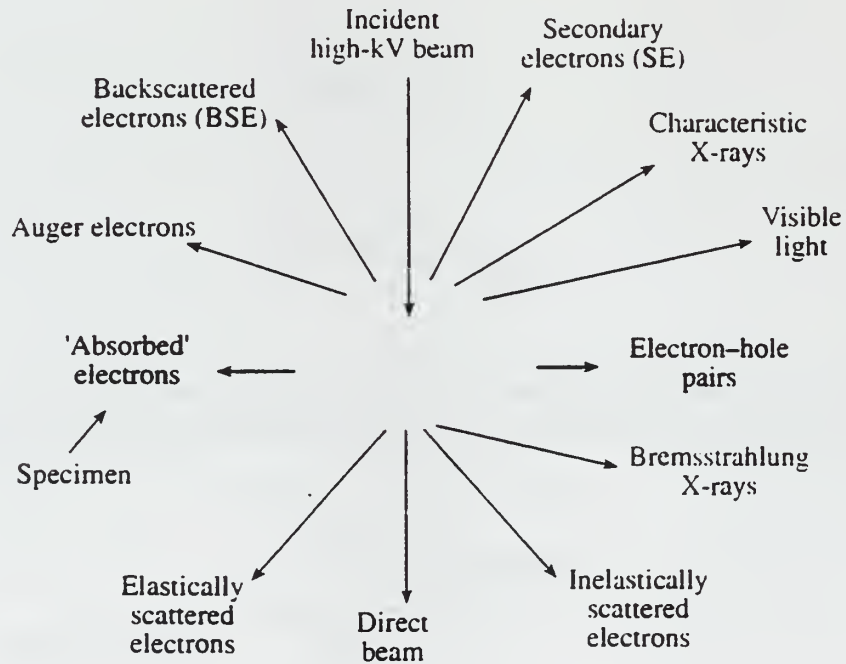
Figure 3.4   Signals generated when a high-energy beam of electrons interacts with a thin specimen [From Ref. 34]

34

4.   Energy Dispersive X-ray Spectroscopy (EDX)

As mentioned earlier, electrons that strike a sample can penetrate through the outer electron shells and remove tightly bound inner-shell electrons to a higher energy level away from the field of the nucleus. This leaves an opening in the inner shell and an electron in a higher energy state, thus ionized. To account for this energy difference, the atom fills the opening form one of the outer shells producing the emission of an x-ray as shown in Figure 3.5. The x-ray has a certain amount of energy depending on and the distance from the nucleus to the outer shell used to fill the missing electron position. As a result a "characteristic x-ray" is produced with a specific energy. The innermost electron shell is the K-shell followed by the L-shell followed by the M-shell and so on. If the opening is in the K-shell and it is filled by an electron from the L-shell, a K_α x-ray is produced, or if its filled by an electron from the M-shell a K_β x-ray is produced. An L_α x-ray is formed if the opening is in the L-shell and it is filled by an electron from the M-shell. Figure 3.6 shows these electronic transitions in as atom. All shells with the exception of the K-shell can have sub shells which are annotated by Roman numerals, example L_{II} or L_{III} from which additional characteristic x-rays such as $K_{\alpha 2}$ and $K_{\alpha 1}$ are created. Figure 3.7 shows the complete range of electron transitions that give rise to characteristic x-rays. [Ref. 35]
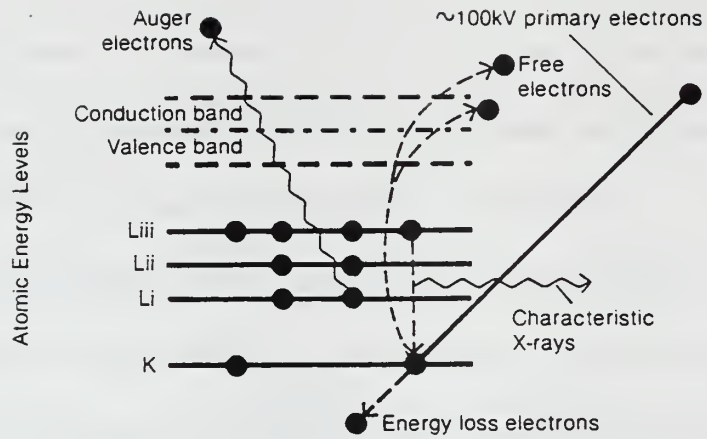
Figure 3.5   Ionization process producing an x-ray [From Ref. 34]
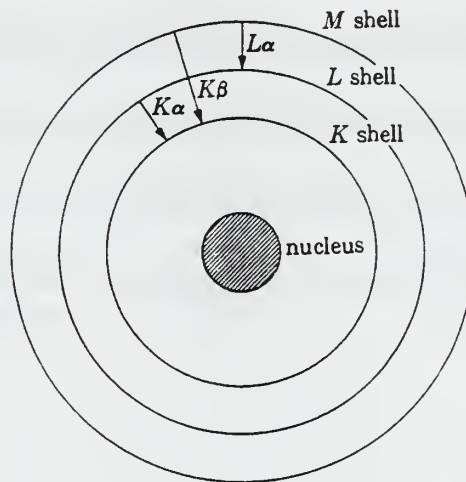

Figure 3.6   Electronic transitions in an atom [From Ref. 36]
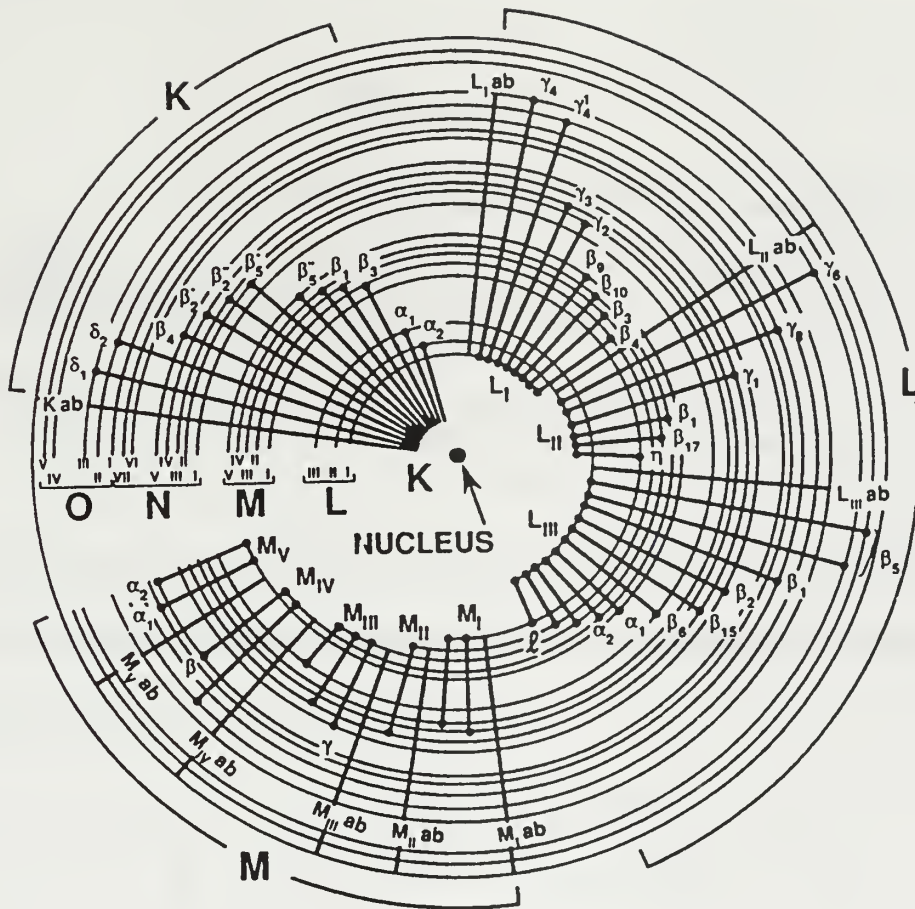
Figure 3.7   Range of possible electron transitions that give rise to characteristic
x-rays [From Ref. 35]

Characteristic x-rays can be detected by an energy dispersive x-ray spectrometer as

shown in Figure 3.8. X-rays are directed to a SiLi detector where they produce electron-

hole pairs. Electrical signals associated with the electron-hole pairs are then amplified and

sent to a multi channel analyzer (MCA) and displayed as intensity verses characteristic

energy (EDX Spectrum). Figure 3.9 shows a typical EDX spectrum. [Ref. 37]
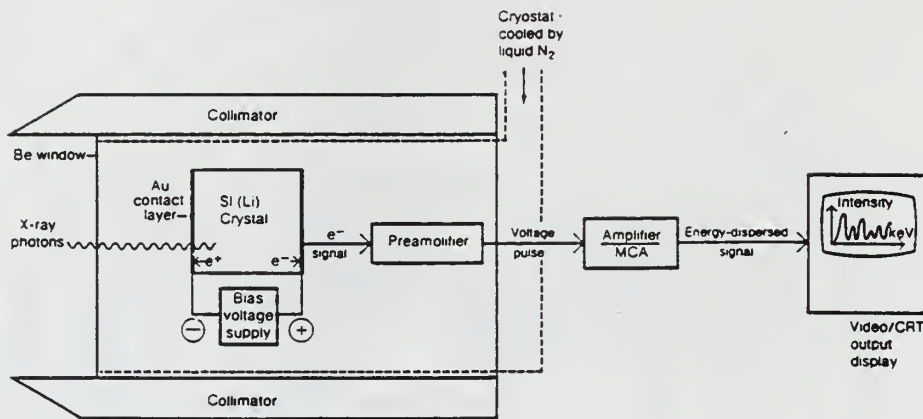
Figure 3.8   Diagram of an energy dispersive x-ray spectrometer [From Ref. 34]
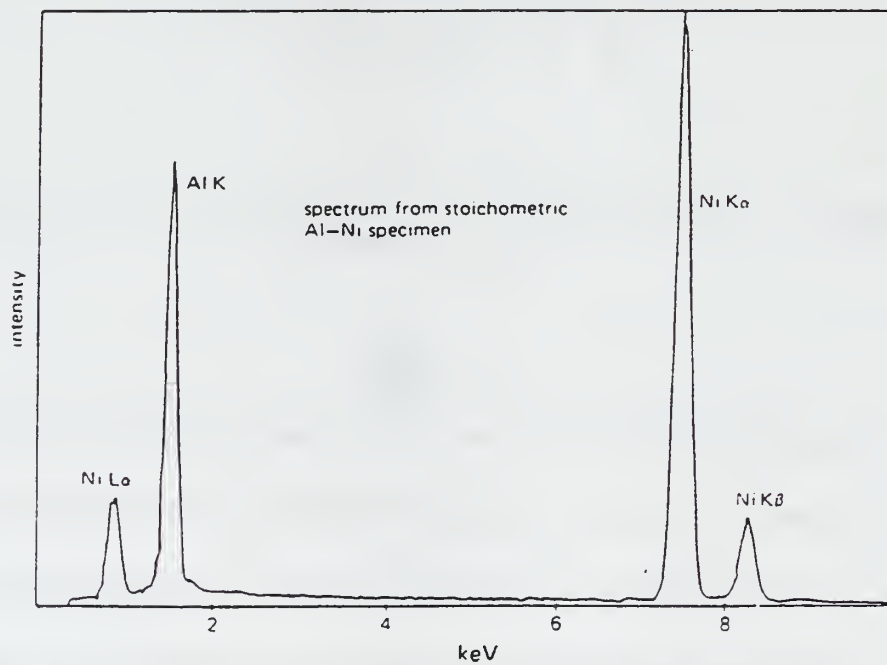

Figure 3.9   Typical EDX spectrum [From Ref. 37]

The x-ray measured intensity of a specific element in a sample is given by :

$$I_A = iQ\omega n$$

I_A = intensity generated by element A

i = current incident on the atom

Q = cross section/cm^2 for the ionization event

ω = fluorescent yield

n = number of atoms in the excited volume

Similarly if the sample is composed of more than one element such as A and B, then the ratios of x-ray intensity is measured in order to give a quantitative result. This ratio will give a relative percentage of A to B in the sample.

$$n_A / n_B = I_A Q_B \omega_B \alpha_B \eta_B / I_B Q_A \omega_A \alpha_A \eta_A$$

α = fraction of K, L, M line collected

η = detector efficiency

A limitation of EDX is its difficulty in measuring light elements such as nitrogen, carbon and oxygen. When light elements are excited by an electron they often eject an Auger electron as opposed to an x-ray. The result is lower energy and reduced number of x-rays making it difficult to properly detect intensities due to poor signal to noise ratio. In addition, the detector efficiency is much reduced for light elements ($Z < 11$). Corrections also have to be taken into account due to atomic number, absorption and fluorescence

between elements in the sample and absorption corrections are particularly difficult for light elements (Z < 11). [Ref. 37]

5.   Parallel Electron Energy Loss Spectroscopy (PEELS)

Parallel electron energy loss spectroscopy analyzes the electrons that are transmitted though the sample. These electrons either have no energy loss or else they have been inelastically scattered by the sample and therefore have lost energy. The composition and structure of the sample will therefore determine the amount of energy lost. The basis of PEELS is to separate these inelastically scattered electrons and quantify the information that they contain [Ref. 35]. After the transmitted electrons have left the sample they enter a magnetic prism separating them into there characteristic energies which are then processed by a multi channel analyzer and display. Figure 3.10 shows a schematic diagram of a magnetic spectrometer for electron energy loss analysis.
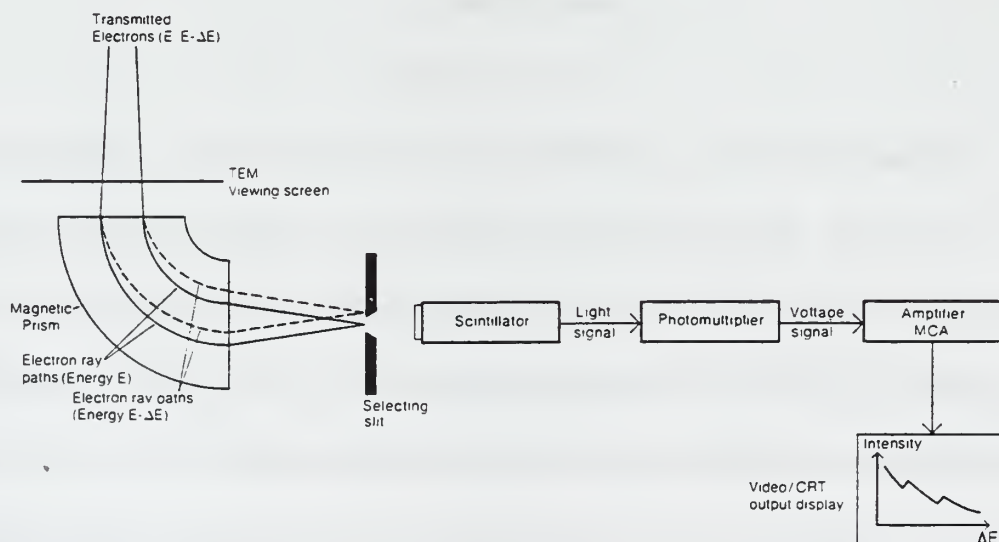

Figure 3.10   Typical electron energy loss spectrometer [From Ref. 34]

The nomenclature used for PEELS analysis is like that used in x-ray analysis but instead of getting K, L, M, etc. peaks in the spectrum, PEELS displays K, L, M, etc. ionization edges as shown in Figure 3.11. The PEELS edges give greater energy resolution and can therefore resolve small differences in spectra including energy states within a shell. A zero loss peak is established as a reference in order to determine the amount of electron energy loss in subsequent edges. This peak represents the electrons that passed through the sample and were not inelastically scattered. From this peak all other edges and associated energy losses are referenced. Qualitative chemical and structural analysis is performed by comparing the observed edges to known standard edges, a form of microchemical "fingerprinting." The edge energy provides the basic information on the elements in the sample [Ref. 30]. Analyzing the energy loss near edge fine structure (ELNES) provides information on the nature of electronic bonding and helps to identify composition and structure such as the difference between TiO and TiO_2. Extended energy loss fine structure (EXELFS) represents oscillations due to short range order effects caused by ejected electrons scattering with neighbor atoms [Ref. 35]. PEELS can also be used to map a desired element in a multi-phase material by detecting the characteristic energy loss across the entire sample. A typical PEELS spectrum is shown in Figure 3.12, and ELNES and EXELFS structures are shown in Figures 3.13 and 3.14
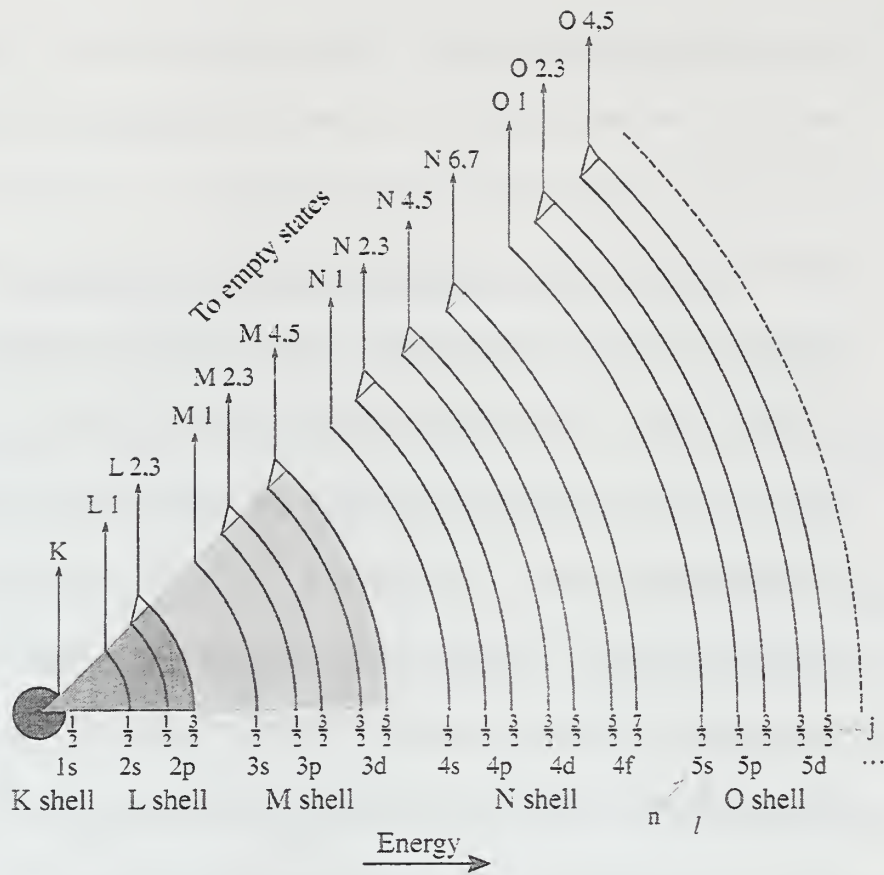
Figure 3.11   The range of possible edges due to inner-shell ionization [From Ref. 35]
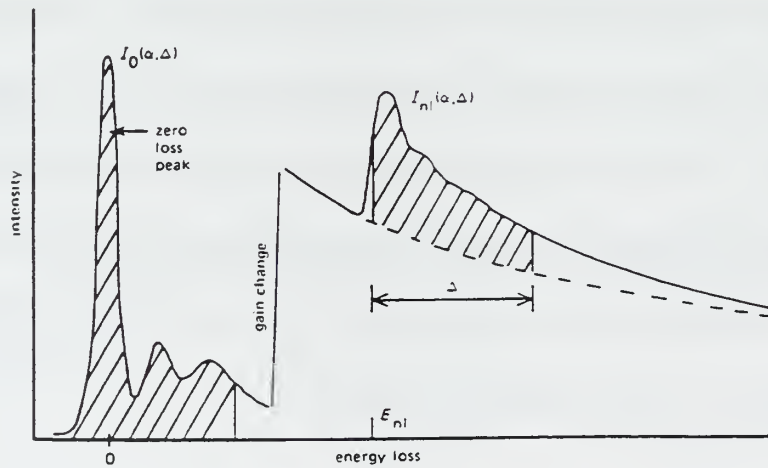

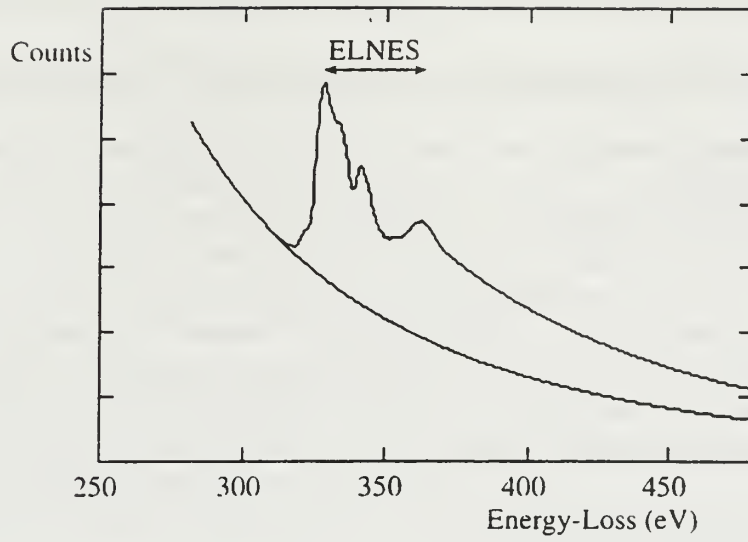Figure 3.12   Typical PEELS spectrum [From Ref. 37]

Figure 3.13 ELNES features of an inner-shell ionization edge [From Ref. 35]
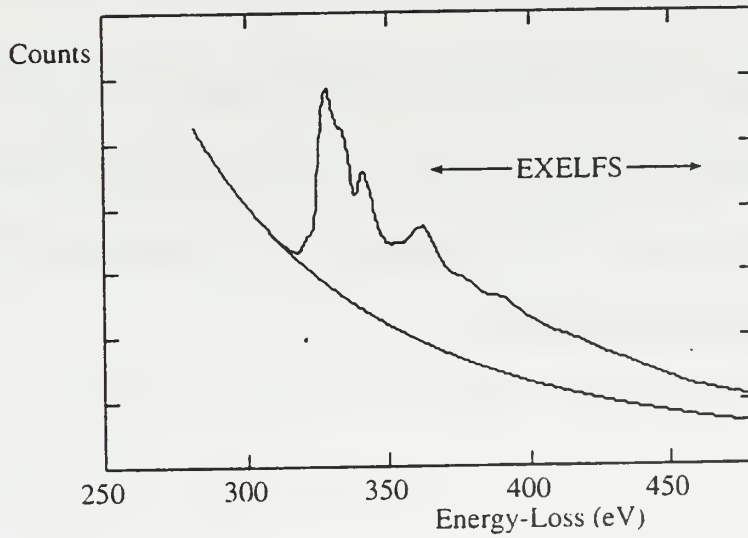

Figure 3.14 EXELFS Features of an inner-shell ionization edge [From Ref. 35]

43

6.   Electron Diffraction Patterns

In addition to EDX and PEELS, diffraction patterns can be created from the sample giving insight to the inclusion's crystalline structure. These patterns are projected onto the fluorescent viewing screen of the TEM and photographed. Diffraction patterns are created from Bragg diffraction of elastically scattered electrons. The scattering occurs at small angles producing spot diffraction patterns representing the planes of the associated crystallographic region. The measurement of the angle of diffraction and the wavelength of electrons can be related to produce the distance between planes of atoms in the inclusion. From this, the Bravais lattice of the crystal structure can be determined. If these patterns are generated using a convergent beam, then additional symmetry information can be obtained which can allow the point and space groups of the crystal structure to be determined. This information, together with microchemical analysis information, can allow the complete characterization of a phase in a TEM sample. [Ref. 35]

Unfortunately the electron diffraction patterns obtained from the non-metallic inclusions present in C-Mn steel weldments are very often difficult to analyze and obtain crystallographic information. This is because they come from samples which are usually multiphase and often polycrystalline.

IV. RESULTS AND ANALYSIS

A. WELD METAL CHEMICAL COMPOSITION

The weld metal chemistries for the final weld passes of all three samples were provided by Dr. G. M. Evans and are shown in Table 4.1 [Ref. 32]. The weldments were prepared in controlled environmental conditions in order to insure specific compositions. All alloying elements with the exception of titanium and aluminum were held fairly constant which helped simplify the inclusion analysis.

SAMPLE	C	MN	Si	S	P	Ti	B	Al	N	O
	%					ppm				
Y	0.070	1.57	0.45	0.006	0.010	390	39	13	83	308
Z	0.072	1.56	0.49	0.007	0.010	420	48	160	67	438
V	0.078	1.44	0.60	0.006	0.007	540	56	580	41	336

Table 4.1   Chemical compositions of samples Y, Z and V [From Ref. 32]

B.   WELD METAL MECHANICAL PROPERTIES

The mechanical properties for the three samples were also provided by Dr. G. M.

Evans and are shown in Table 4.2 [Ref. 32]. Shelf temperatures for 100J and 28 J

Charpy-V notch tests are shown.

	YS	EL	RA	ISO-V Celsius	
	MPa	%	%	100J	28J
Y	546	25.8	73.0	-84	-114
Z	610	27.2	73.4	-83	-100
V	668	20.2	69.4	-12	-46

Table 4.2   Mechanical properties of samples Y, Z and V [From Ref. 32]

C.   OPTICAL MICROSCOPY

A macrophotograph of sample Y, shown in Figure 4.1, represents the typical

twenty-seven weld bead placement for each sample. Figures 4.2 through 4.7 show the

first pass and last pass microstructures for each sample. The last pass micrographs clearly

46

show the presence of acicular ferrite (AF) and ferrite with second phase (FS) formations for all three samples.
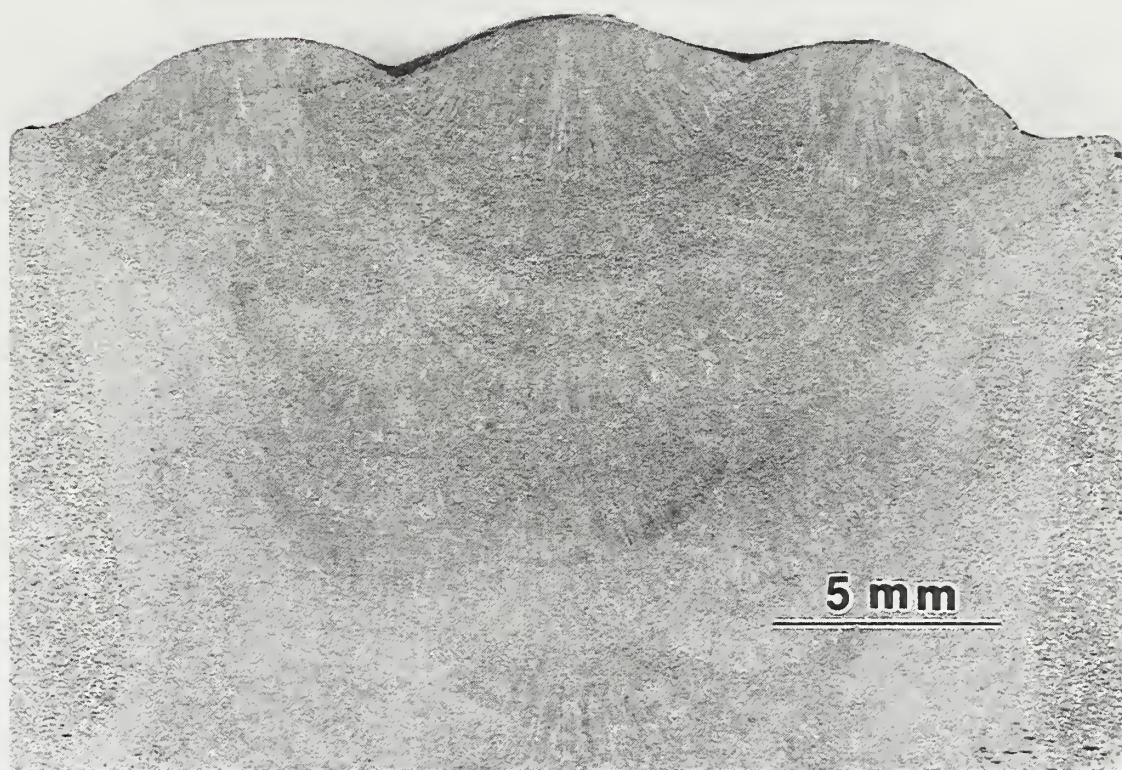
Figure 4.1   Typical optical macrograph of sample Y
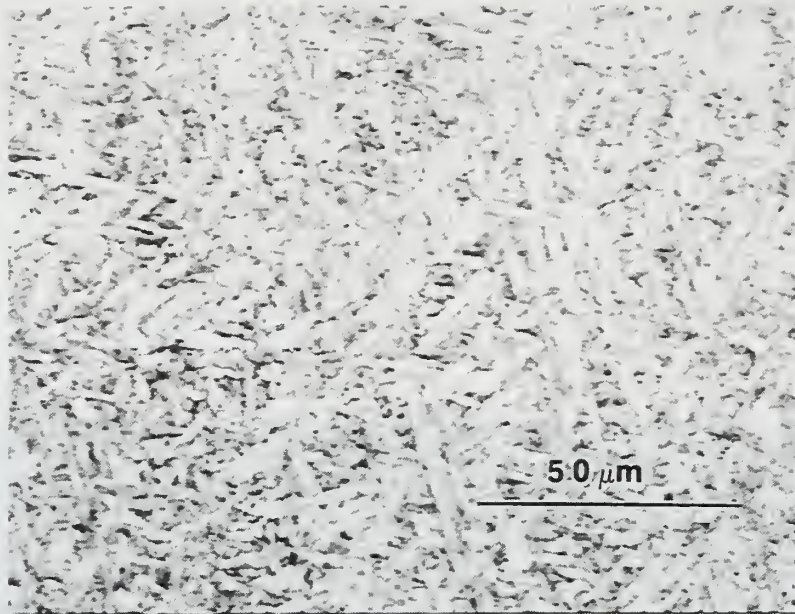
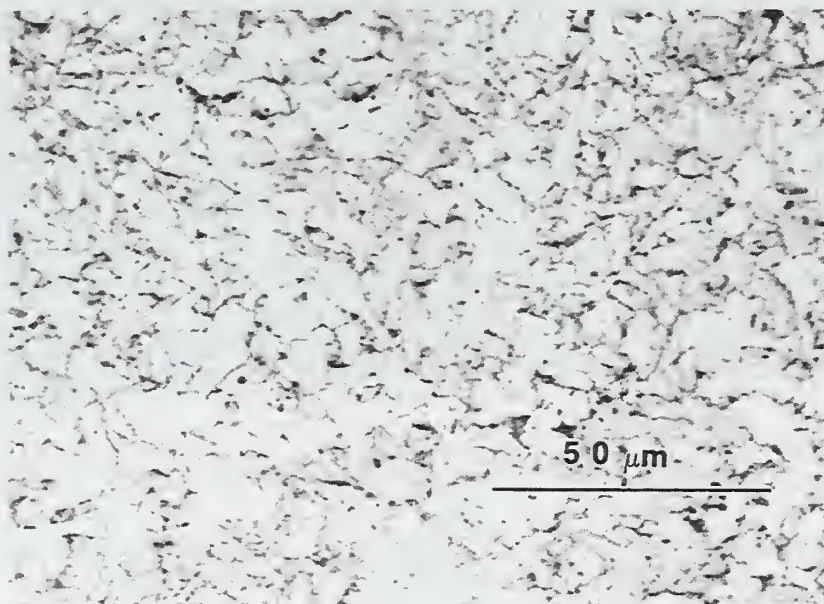Figure 4.2   Optical micrographs of final weld pass of sample Y

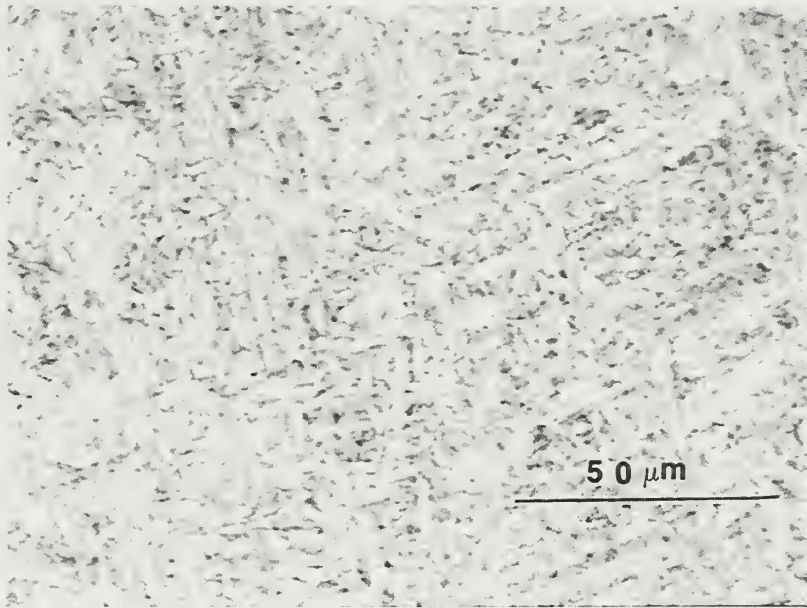Figure 4.3   Optical micrographs of first weld pass of sample Y

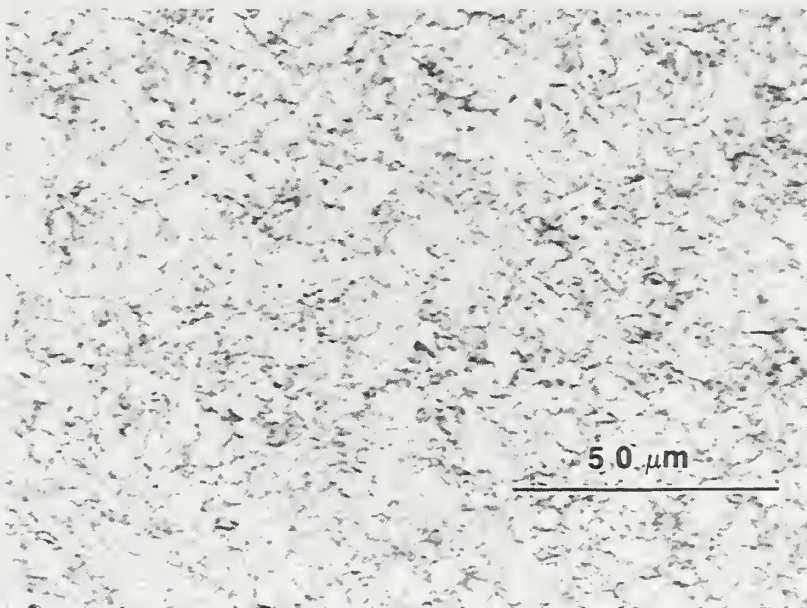Figure 4.4 Optical micrographs of final weld pass of sample Z

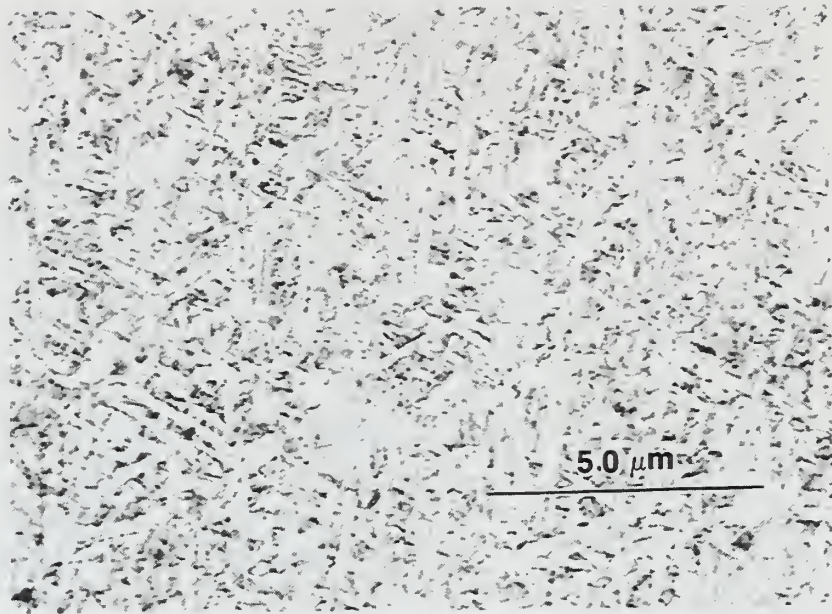Figure 4.5 Optical micrographs of first weld pass of sample Z

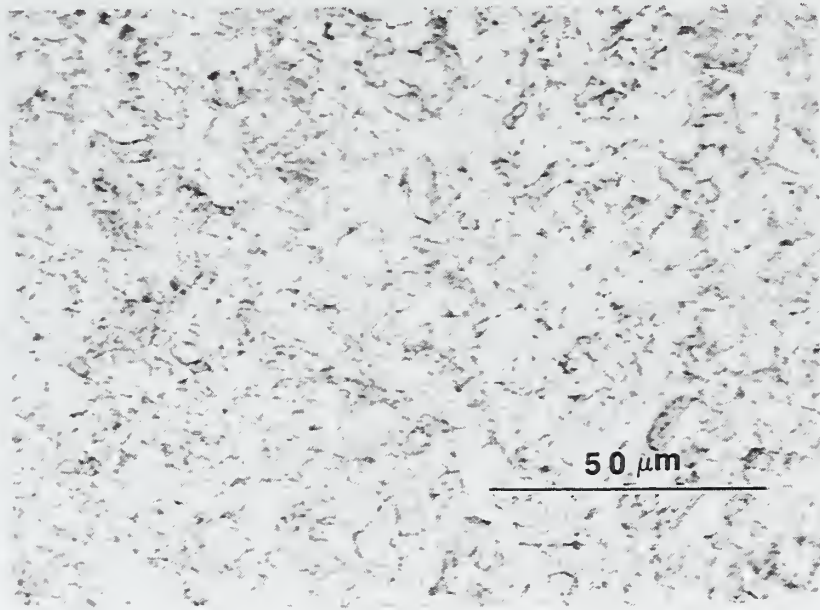Figure 4.6   Optical micrographs of final weld pass of sample V

Figure 4.7   Optical micrographs of first weld pass of sample V

D. ACICULAR FERRITE CONTENT

Optical examination by Dr. G. M. Evans on the final pass weld bead was used to determine and measure the major microstructure components of each sample [Ref. 32]. Microstructural identification was performed in accordance with Ref. 3 using a manual point count survey. The results show that sample Y contained approximately 87% acicular ferrite (AF), sample Z approximately 92% aciclular ferrite (AF) and sample V approximately 65% acicular ferrite (AF). Remaining phases were primary ferrite (PF) and ferrite with second phase (FS). Figures 4.8 through 4.10 show the individual microstructure components for each sample. Figure 4.11 shows a comparison of the microstructures compositions of the three samples as the aluminum level increases for standard nitrogen levels (between about 50 and 100 ppm nitrogen).
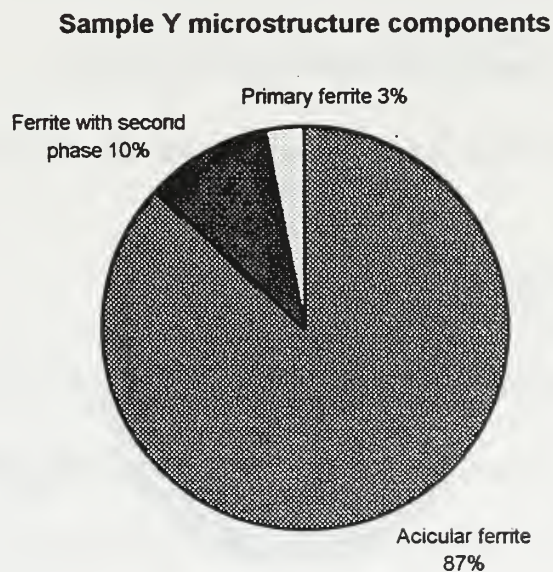
Sample Y microstructure components

Primary ferrite 3%

Ferrite with second
phase 10%

Acicular ferrite
87%

Figure 4.8   Chart showing the ferrite distribution for sample Y

51

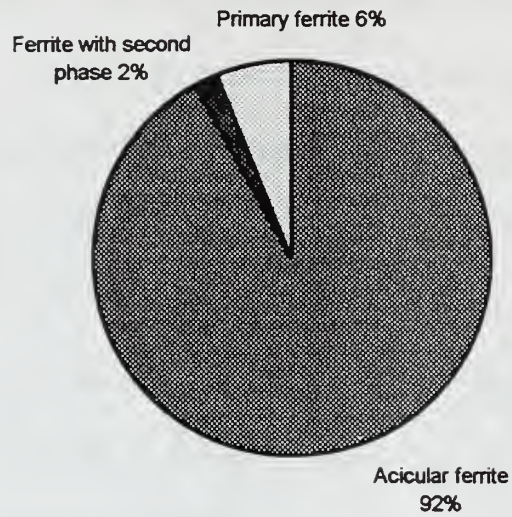**Sample Z microstructure components**

Figure 4.9   Chart showing the ferrite distribution for sample Z
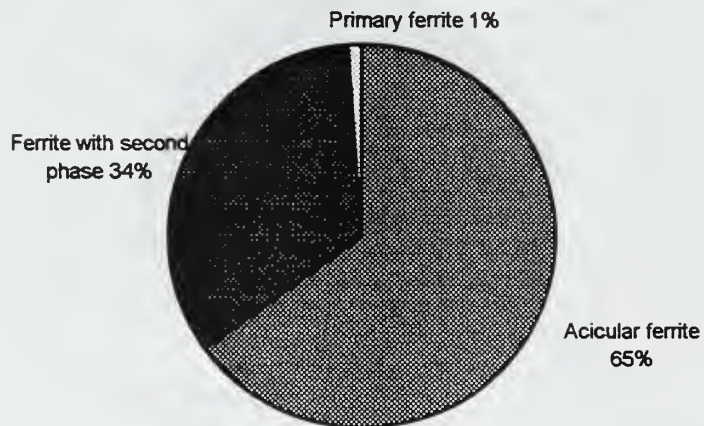
Sample V microstructure components

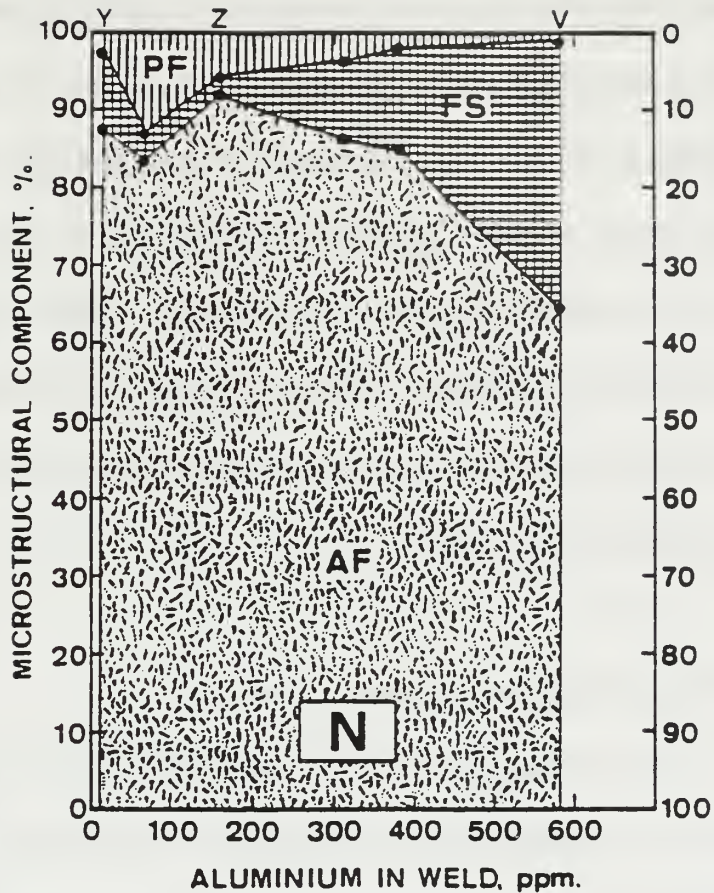Figure 4.10   Chart showing the ferrite distribution for sample V

Figure 4.11   Effect of aluminum on weld metal microstructure of samples Y, Z and V
[From Ref. 32]

E.   TEM RESULTS OF WELD METAL SAMPLES Y, Z AND V

Microchemical analysis of the inclusions found on extraction replicas taken from

samples Y, Z, and V was performed on the TOPCON 002B TEM located at the Naval

Postgraduate School. EDX using a 6 nm probe was conducted on twenty-five inclusions

per sample in order to determine overall average chemical composition of the inclusions.

53

In depth study of three individual inclusions per sample was then conducted through the use of EDX and PEELS and comparisons were made. PEELS data on the inclusions was then compared to known PEELS standards in order to "fingerprint" inclusion components such as TiO where it is difficult to make an accurate analysis by EDX. Small probe sizes were used on the samples, 6 nm For EDX and 3 nm for PEELS, to allow for segregation of compositional changes in different areas of the inclusions. PEELS maps were also generated on one inclusion per sample. Diffraction patterns were also generated and recorded but proved too difficult to analyze in most cases because of the multiphase, polycrystalline nature of the inclusions.

1. PEELS Edges and Standard Spectra

PEELS results were compared to known energy loss edges and spectra in order to determine the elements present and their coordination so that differentiation between TiO and TiO_2 could be made. Gatan has published spectra in a reference text covering all stable elements [Ref. 38]. Edge energies for elements analyzed in the inclusions are as follows:

$$N_K = 401 \text{ eV} \qquad O_K = 532 \text{ eV}$$

$$Al_{L2,3} = 73 \text{ eV} \qquad S_{L2,3} = 165 \text{ eV}$$

$$Ti_{L3} = 456 \text{ eV} \qquad Ti_{L2} = 462 \text{ eV}$$

$$Mn_{L3} = 640 \text{ eV} \qquad Mn_{L2} = 651 \text{ eV}$$

To differentiate between TiO and TiO$_2$, Drs. A. G. Fox and E. S. K. Menon pulverized known samples into fine powders and generated PEELS spectra for the two compounds. Figures 4.12 through 4.17 show standard spectra to include edge and ELNES structures for titanium oxides and aluminum oxides often found in non-metallic inclusions.
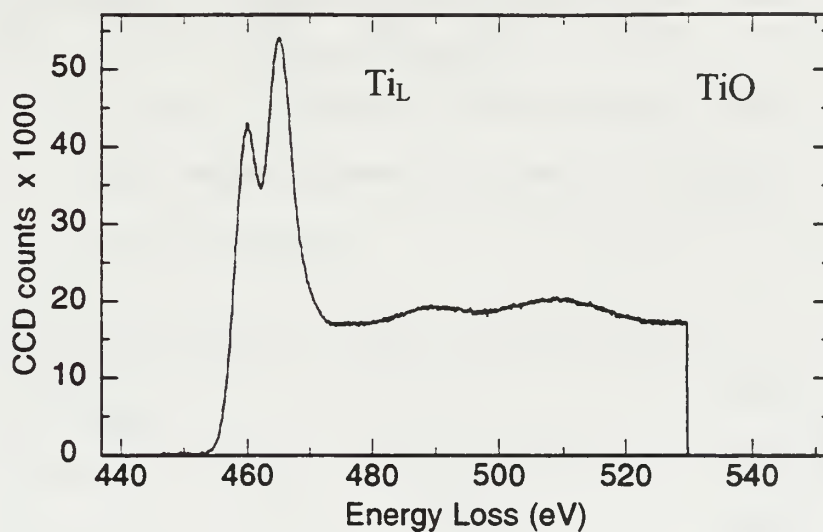

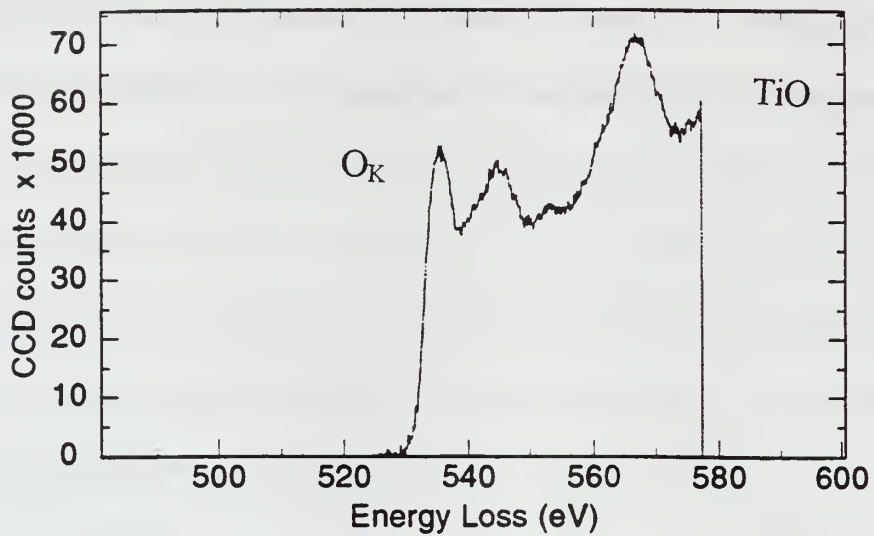Figure 4.12   Energy loss spectra for titanium - TiO

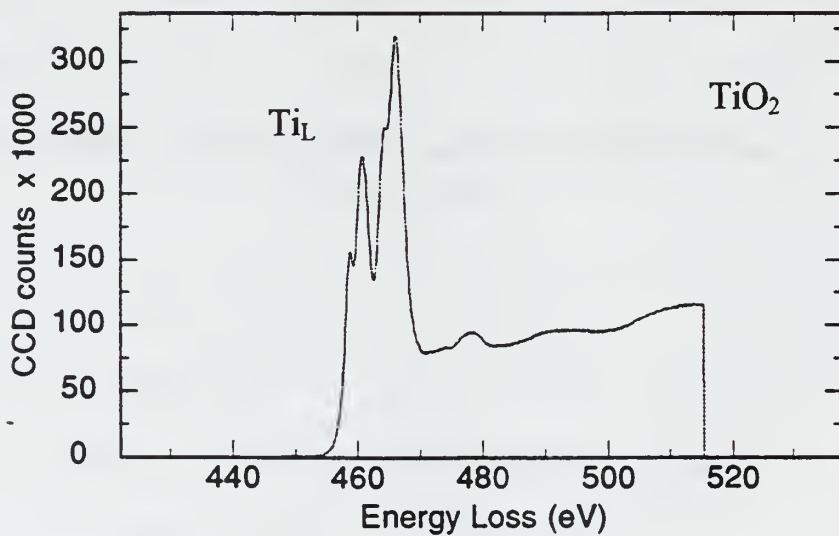Figure 4.13   Energy loss spectra for oxygen - TiO
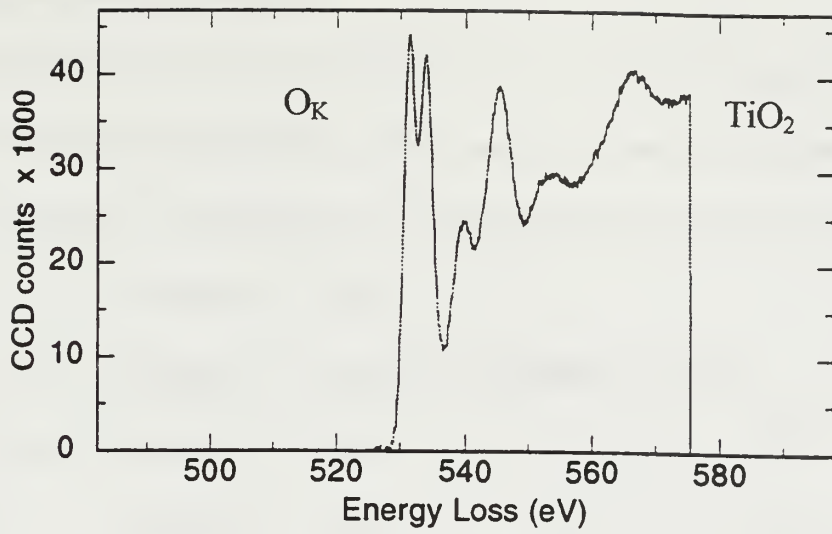

Figure 4.14   Energy loss spectra for titanium - TiO$_2$

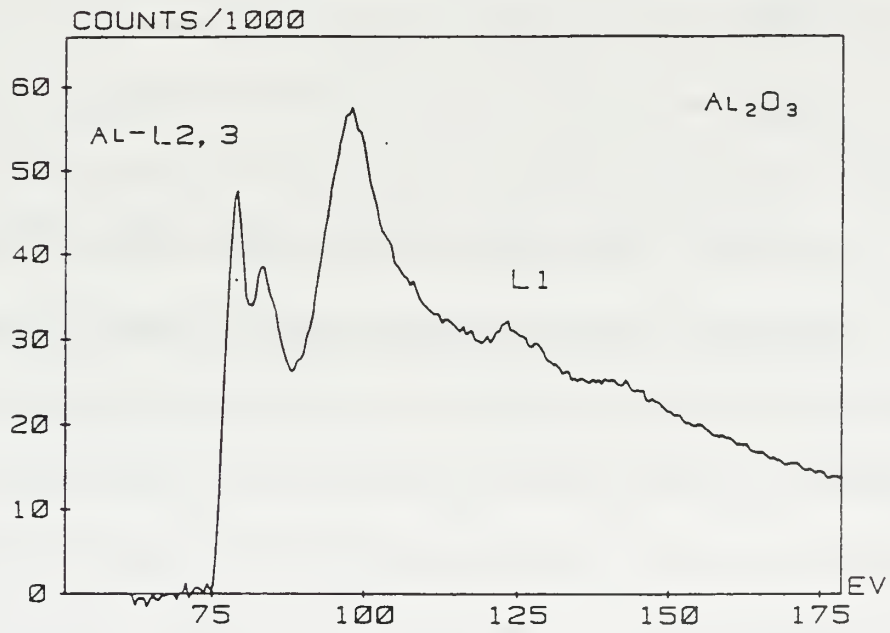Figure 4.15   Energy loss spectra for oxygen - TiO$_2$

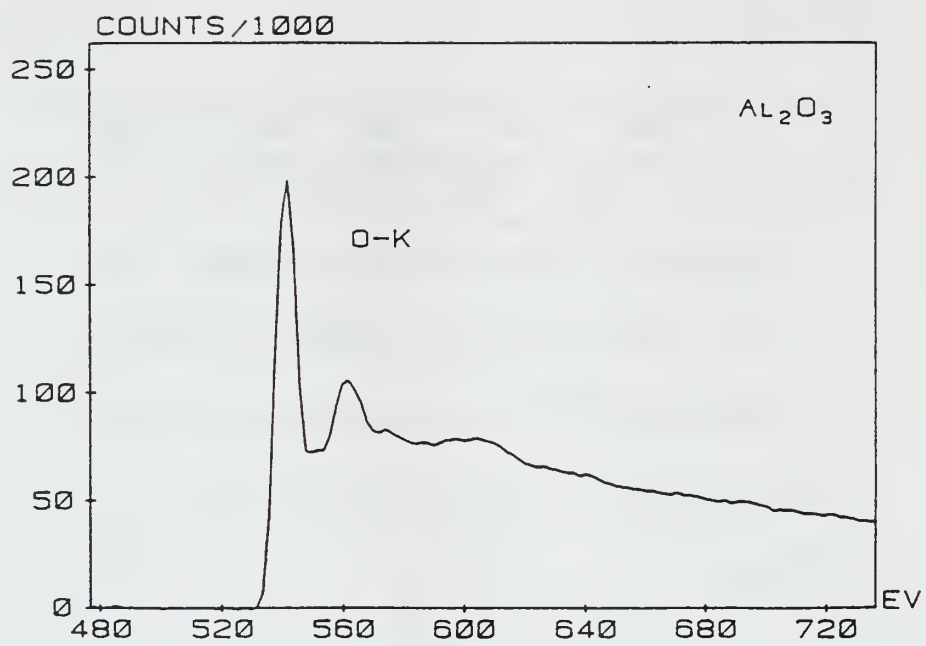Figure 4.16   Energy loss spectra for aluminum - Al$_2$O$_3$ [From Ref. 38]

57

Figure 4.17   Energy loss spectra for oxygen - Al_2O_3 [From Ref. 38]

2. Prediction of Inclusion Composition for the Samples Studied Using Simple Thermodynamic Principles

As mentioned previously in the background, the power of an element to deoxidize is a result of its free energy of formation. The lower the free energy the higher the deoxidizing capability. The following is a list of deoxidizers from strongest to weakest:

Aluminum Al_2O_3

Titanium Ti_xO_y (TiO, TiO_2, etc.)

Silicon SiO_2

Manganese MnO

It should be noted that TiN has a lower free energy of formation than Ti_xO_y. However, in the weld metal samples studied the oxygen activity is very high so both oxides and nitrides of titanium are possible especially when significant amounts of aluminum are present leaving very little oxygen for titanium oxide formation. Sulfides in the form of MnS and CuS are also expected. Due to inhomogeneities in dissolved aluminum, titanium, oxygen, silicon and manganese in the weld, various inclusion compositions and phases can possibly form in the weld pool. As a result complex binary and possibly ternary phase reactions can occur in the samples making it very difficult to predict exactly which phases will develop in any given sample. For example, Greene and Fox found that samples containing 1 ppm Ti and 6 ppm Al produced inclusions containing MnO, SiO_2 and CuS. Whereas for samples containing 28 ppm Ti and 5 ppm Al, the

inclusions contained $MnO.SiO_2$ and TiO (possibly in compound form) and CuS [Ref. 30, 39].

Sample Y, which contains 390 ppm Ti and 13 ppm Al, was the first sample to be studied. Titanium has the highest activity in the sample and so it was expected that the majority of inclusions in the final pass region would contain TiO and/or TiO_2 along with SiO_2, MnO and/or $MnO.SiO_2$ and very small amounts of Al_2O_3. Also small amounts of sulfides in the form of CuS and/or MnS were expected.

Sample Z, 420 ppm Ti and 160 ppm Al, was the second sample studied. In this sample with the higher aluminum activity, it was expected that a large amount of oxygen would be consumed in Al_2O_3 formation followed by TiO and/or TiO_2 possibly TiN and SiO_2 and MnO and/or $MnO.SiO_2$. Small amounts of sulfides were also expected.

Sample V, 540 ppm Ti and 580 ppm Al, was the third sample studied. In this sample the aluminum activity is high and it was expected that all of oxygen would react with aluminum to form Al_2O_3 leaving the majority of titanium to form TiN. Smaller amounts of TiO and/or TiO_2, MnO, SiO_2 and/or $MnO.SiO_2$ and trace amounts of MnS and CuS were also expected.

It should be noted that, in the present work, because diffraction studies were not performed in detail, it was not possible to determine exactly the phases present but the oxide type for each element can be determined and where segregation occurred, a good estimate of the phases present could be made.

3.   Sample Y - EDX and PEELS Results

a.   *Inclusion Composition Analysis*

In order to determine an average composition of the non-metallic inclusions in sample Y, EDX analysis was performed on twenty-five random inclusions using a probe size of 6 nm. The atomic percentages of the major elements in each inclusion is presented in Table 4.3 along with the average atomic percentage for each element. Oxygen was detected but could not be accurately quantified because it is a light element. Figure 4.18 shows a graph comparing the elements overall atomic percent averages. As predicted, titanium was the primary element present followed by manganese and then small amounts of silicon, sulfur, copper and aluminum. In-depth EDX and PEELS analysis was then conducted on inclusions JWY1, JWY2 and JWY3 in order to determine specific compositions in different areas of the inclusions and identify the possible chemical phases present.

Inclusion	Al	Si	S	Ti	Mn	Cu
1	1.39	1.85	0.00	81.82	11.72	3.22
2	8.23	6.64	0.00	57.42	4.71	22.99
3	1.52	1.69	0.16	84.97	8.52	3.14
4	1.25	1.29	0.07	85.2	9.76	2.44
5	1.76	2.71	0.21	82.9	8.94	3.49
6	1.39	1.75	9.94	65.03	19.29	2.59
7	1.33	1.99	12.73	58.71	22.71	2.52
8	1.33	1.98	0.11	84.68	9.18	2.72
9	2.58	3.76	0.82	79.14	7.09	6.61
10	2.55	4.87	1.59	75.93	9.29	5.76
11	1.89	3.03	0.13	82.94	8.2	3.8
12	5.41	5.92	13.78	38.54	1.27	35.07
13	1.23	2.22	0.00	83.44	8.75	4.36
14	2.14	4.36	0.16	85.47	4.39	3.48
15	1.67	3.62	1.36	73.59	6.45	13.31
16	1.83	3.58	9.42	77.69	2.53	4.95
17	0.57	1.73	0.36	83.58	8.68	5.08
18	1.06	2.25	0.00	83.57	6.52	6.60
19	1.54	2.53	0.32	72.59	1.64	21.38
20	2.15	1.37	0.35	79.69	3.95	12.49
21	1.53	1.73	10.26	74.68	9.25	2.55
22	1.33	1.94	1.38	73.83	12.35	9.17
23	3.52	3.07	0.72	86.92	5.42	0.35
24	2.16	3.48	0.66	58.72	1.85	33.13
25	0.93	4.83	0.27	83.66	3.92	6.39
Average	2.09	2.97	2.59	75.79	7.86	8.70

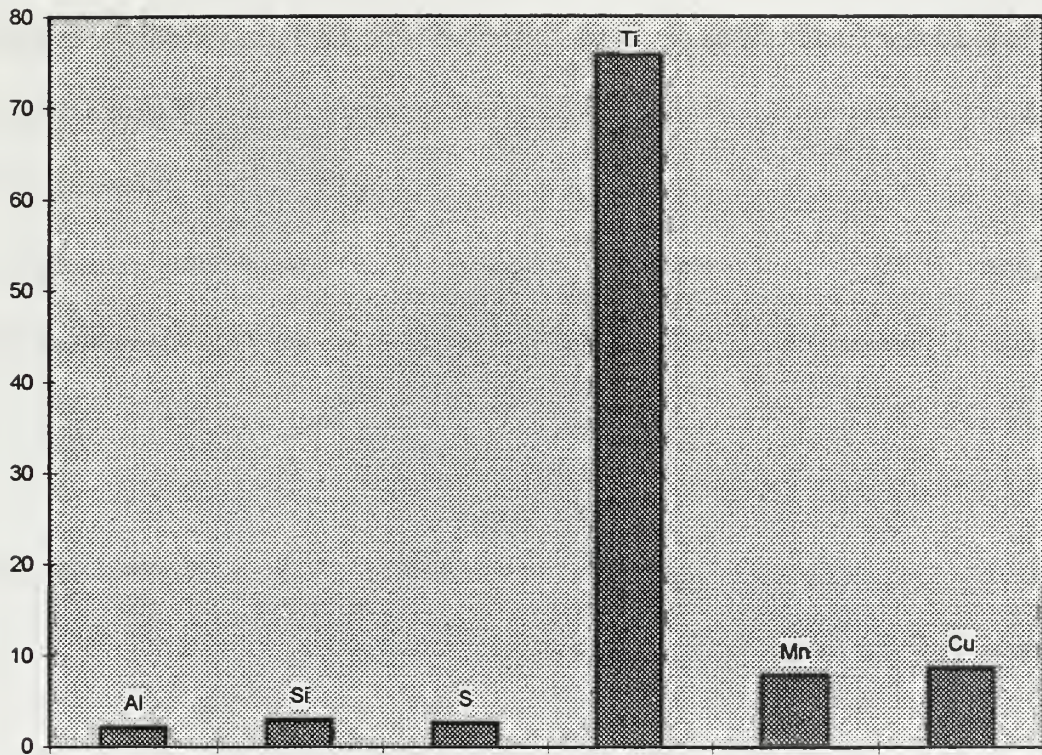Table 4.3   Sample Y inclusion analysis - Atomic %

Figure 4.18   Sample Y average inclusion composition - Atomic %

b.   *Inclusion JWY1*

A TEM micrograph of inclusion JWY1 is shown in Figure 4.19. This inclusion appeared to have two separate regions, a darker area in the upper half of the inclusion and a lighter area in the lower half of the inclusion. The different areas were analyzed by both EDX and PEELS and it was found that the composition within the two areas was approximately the same. It was therefore concluded that the contrast variation was due to thickness and/or diffraction effects. EDX analysis given in Figure 4.20 showed high amounts of titanium (81.3%) present in the inclusion, followed by a lower amount of manganese (8.0%). All other elements were present in very low amounts. This again supports the presence of TiO and/or TiO_2, MnO and/or MnS and trace amounts of CuS in the inclusion. PEELS was conducted on titanium, oxygen and manganese shown in Figures 4.21 through 4.23. The spectra of the $Ti_{L2,3}$ and O_K through ELNES "fingerprinting," suggested TiO-like coordination rather than TiO_2. The weak $Mn_{L2,3}$ edge, indicated MnO like coordination and/or possibly small amounts of MnS.
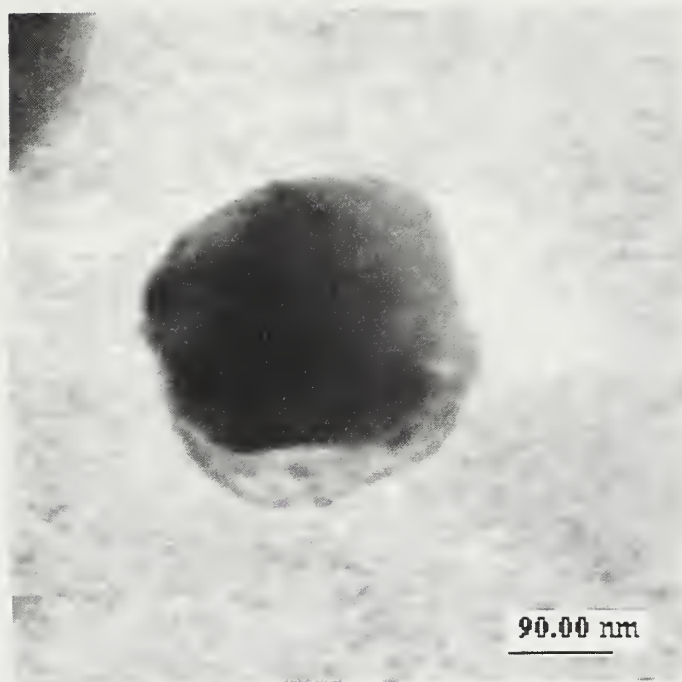
Figure 4.19   TEM micrograph of inclusion JWY1

Element	Weight %	Atomic %
AlK	2.6	4.5
SiK	2.8	4.6
S K	1.1	1.6
TiK	84.0	81.3
MnK	9.5	8.0
CuK	0.0	0.0
Total	100.0	100.0

Label:					
kV:200.0	Tilt:0.0	Take-off:35.0	Det Type:SUTW	Res:142	Tc:40
FS : 638		Lsec : 100		20-Mar-98	13:43:19
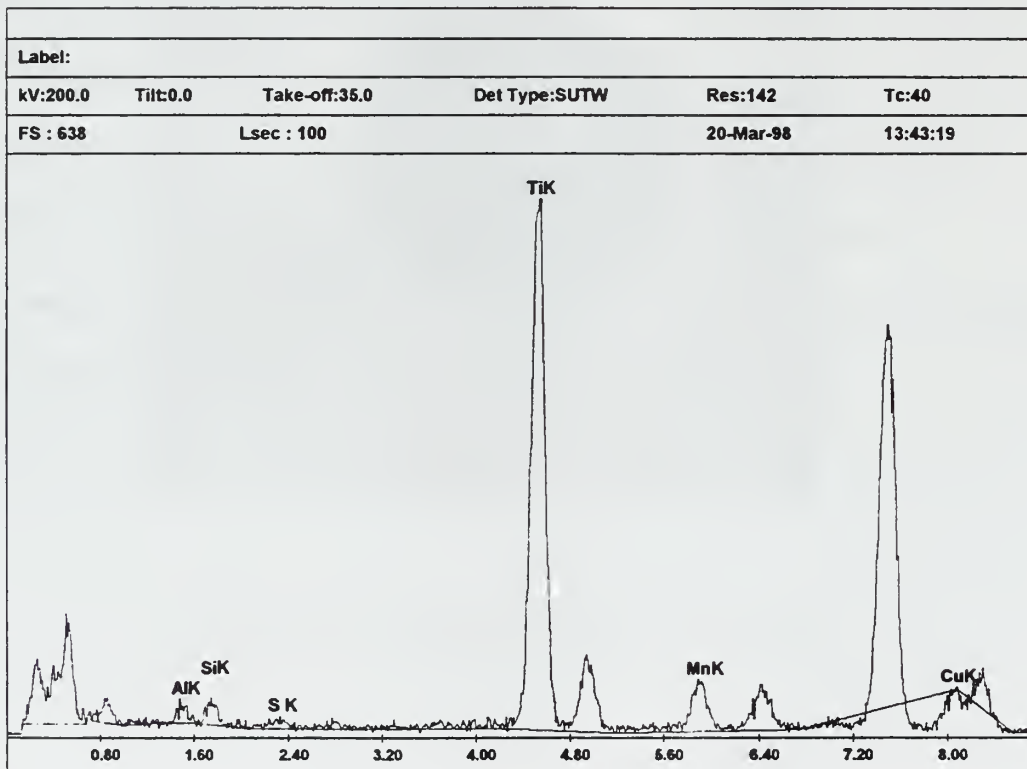
Figure 4.20   EDX analysis of inclusion JWY1
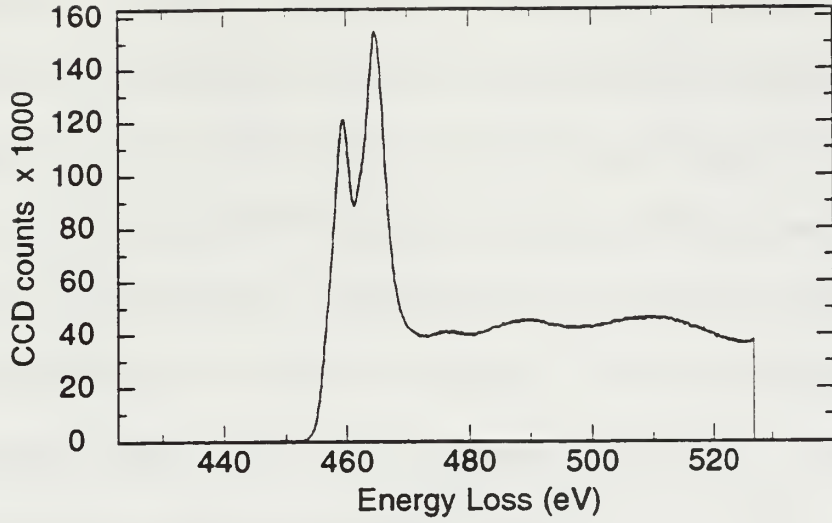
Figure 4.21   PEELS analysis of inclusion JWY1 - $Ti_{L2,3}$ spectrum
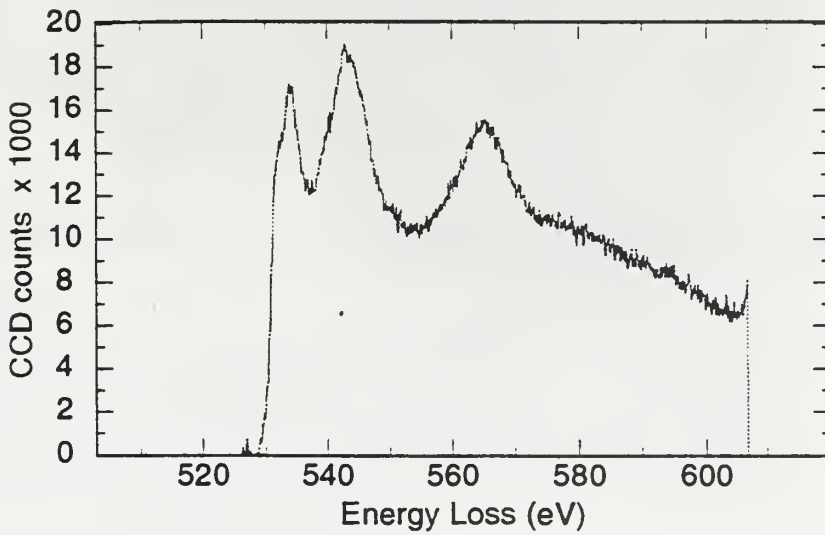
Figure 4.22   PEELS analysis of inclusion JWY1 - O_K spectrum
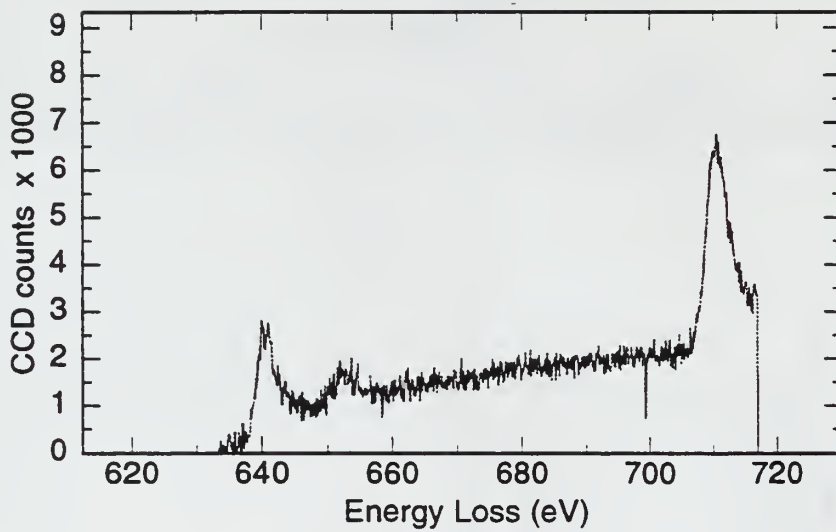
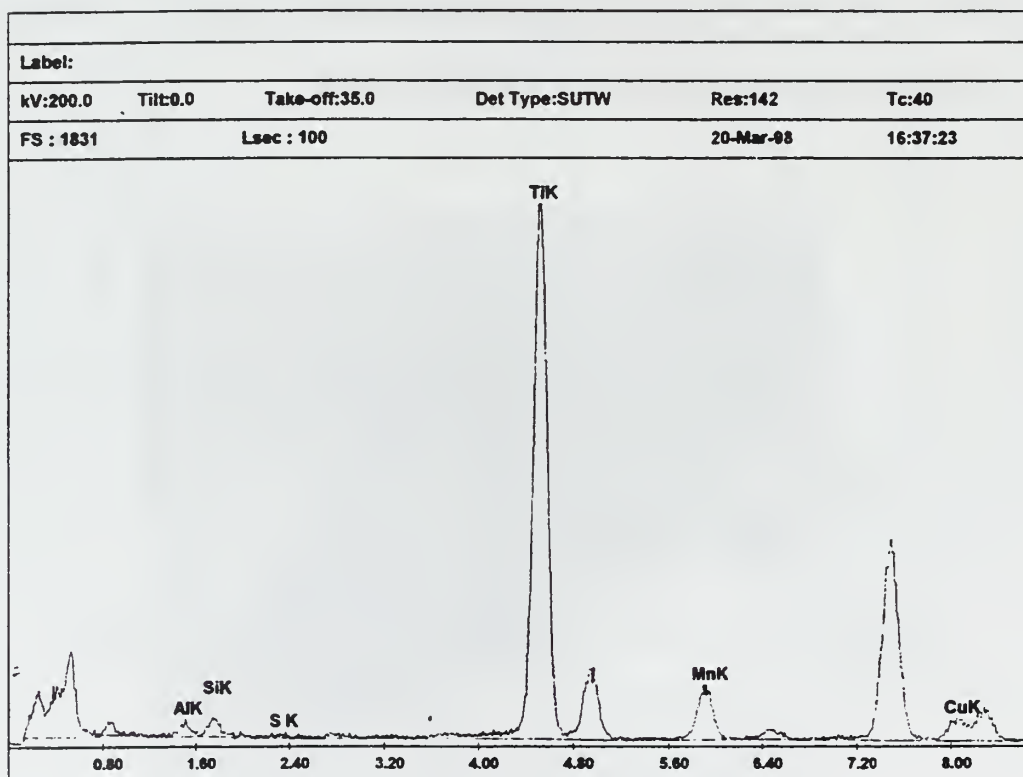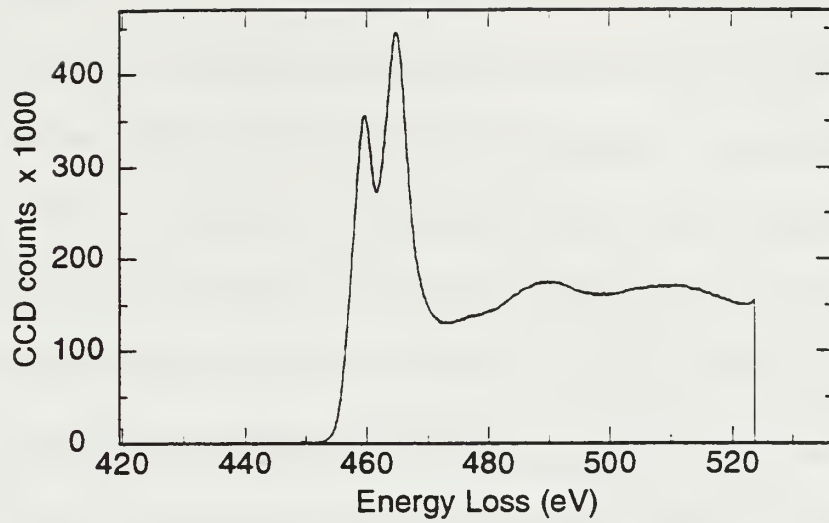Figure 4.23   PEELS analysis of inclusion JWY1 - $Mn_{L2,3}$ spectrum

68

c.   *Inclusion JWY2*

TEM micrograph of inclusion JWY2 is shown in Figure 4.24. This inclusion appeared to be faceted and possibly contained areas with different compositions. EDX and PEELS analysis performed in different areas of the inclusion suggested that it was homogeneous and very similar to JWY1. The EDX data in Figure 4.25 showed the strong presence of titanium (80.6%) followed by manganese (8.2%) and trace amounts of aluminum, silicon, sulfur and copper. PEELS analysis was conducted on titanium, oxygen and manganese shown in Figures 4.26 and Figure 4.28. The ELNES of the $Ti_{L2,3}$ and O_K edges again suggested the TiO-like coordination rather than TiO_2. The weak $Mn_{L2,3}$ edge again infers small amounts of MnO and/or MnS.
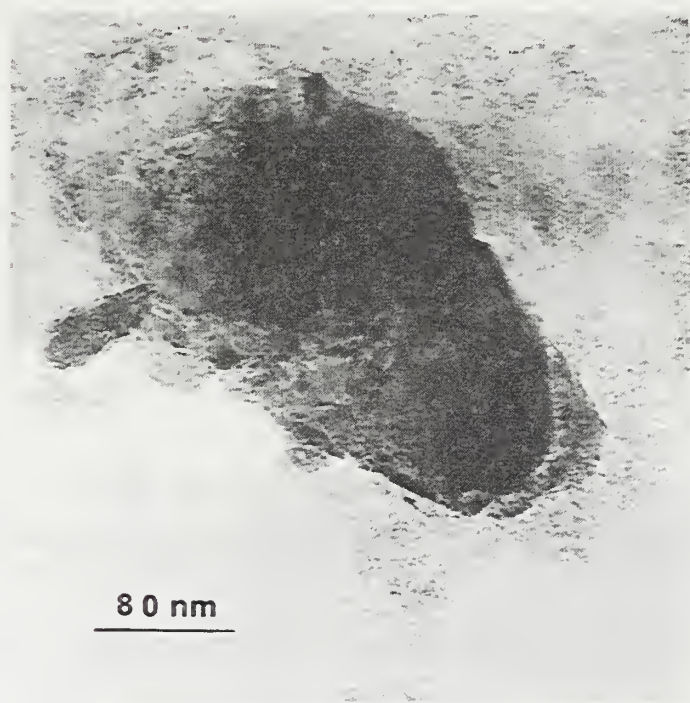
Figure 4.24   TEM micrograph of inclusion JWY2

Element	Weight %	Atomic %
AlK	1.8	3.2
SiK	2.1	3.5
S K	0.4	0.5
TiK	81.0	80.6
MnK	9.4	8.2
CuK	5.4	4.1
Total	100.0	100.0

Figure 4.25   EDX analysis of inclusion JWY2

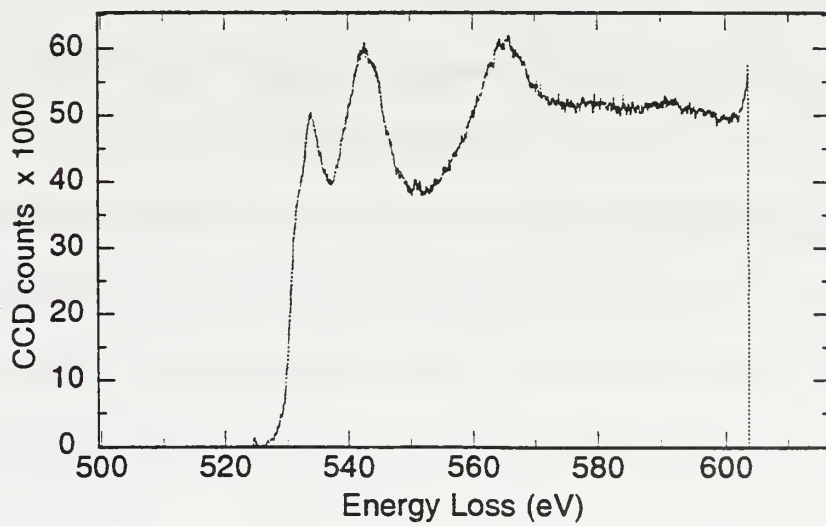Figure 4.26   PEELS analysis of inclusion JWY2 - Ti$_{L2,3}$ spectrum

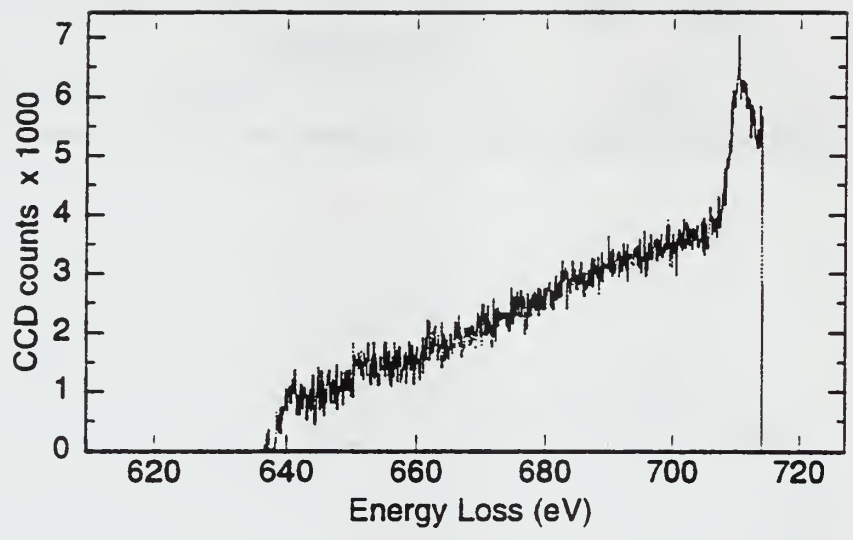Figure 4.27   PEELS analysis of inclusion JWY2 - O$_K$ spectrum

71

Figure 4.28   PEELS analysis of inclusion JWY2 - Mn$_{L2,3}$ spectrum

72

d.   *Inclusion JWY3*

Inclusion JWY3 was segregated into two regions, Region A and Region B, as shown in Figure 4.29. EDX analysis of Region A is shown in Figure 4.30 and again confirmed the presence of titanium (85.0%) and manganese (9.4%) with small amounts of the other elements. PEELS analysis was conducted on titanium, oxygen and manganese in Region A, Figure 4.31 through 4.33. Once again, the PEELS spectra suggested TiO-like coordination. The more prevalent manganese edge inferred a stronger presence of MnO and/or MnS than previously observed in the other two inclusions. EDX analysis in Region B showed a lower presence of titanium (57.0%) and a higher amount of manganese (22.0%) and sulfur (16.1%) than previously seen in other inclusions, Figure 4.34. PEELS data supported the EDX results by showing evidence of lower amounts of TiO formation, Figures 4.35 and 4.36, and a stronger $Mn_{L2,3}$ edge, Figure 4.37. The presence of a $S_{L2,3}$ edge at 165 eV, Figure 4.38, indicated higher amounts of MnS than observed in inclusions JWY1 and JWY2. PEELS maps of the inclusion were produced and are displayed in Figure 4.39 in order to better clarify the segregation of the inclusion composition. The titanium, oxygen and manganese maps clearly showed two separate formations, one being TiO-rich in the upper right area of the inclusion and the other being MnS in the lower left area of the inclusion. It was not possible to obtain a sulfur map because the carbon around the inclusion was destroyed due to electron bombardment during the sulfur analyses causing the inclusion to "drop out" of the extraction replica.
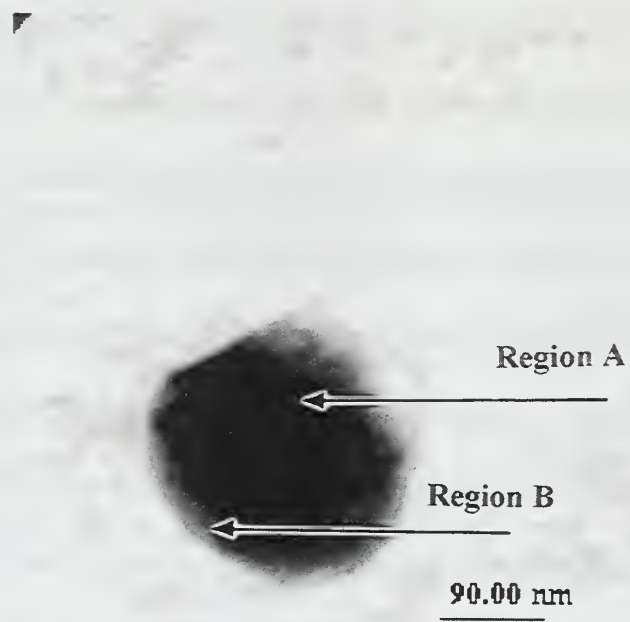
Figure 4.29   TEM micrograph of inclusion JWY3

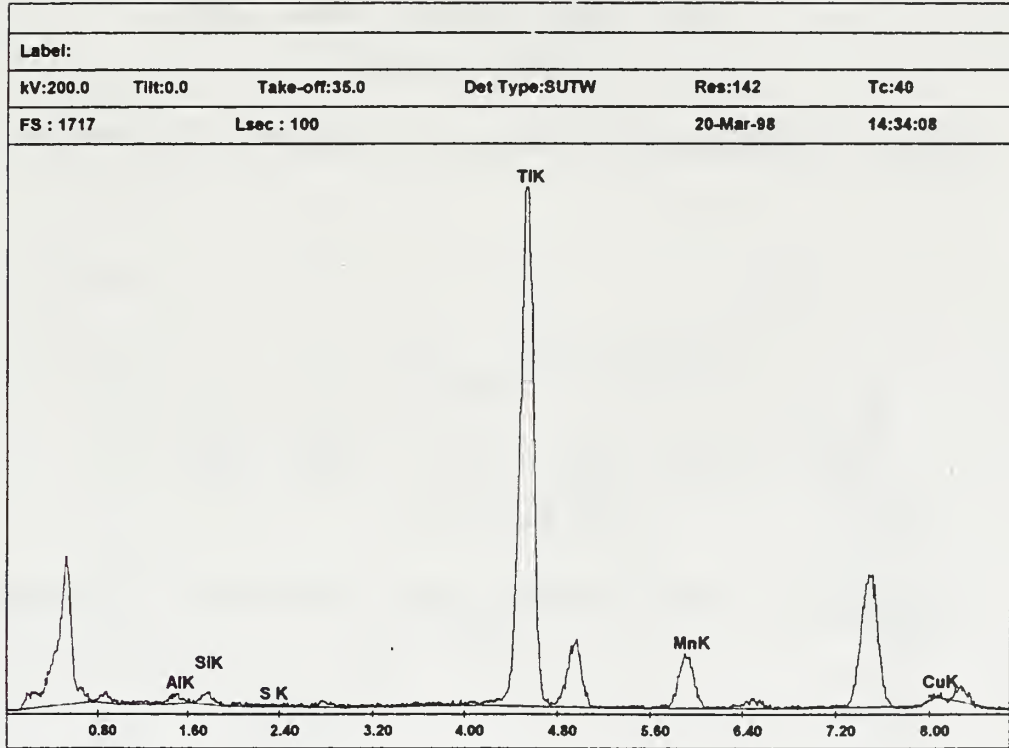| Element	Weight %	Atomic %
AlK	1.3	2.4
SiK	1.4	2.4
S K	0.3	0.5
TiK	85.6	85.0
MnK	10.8	9.4
CuK	0.5	0.4
Total	100.0	100.0

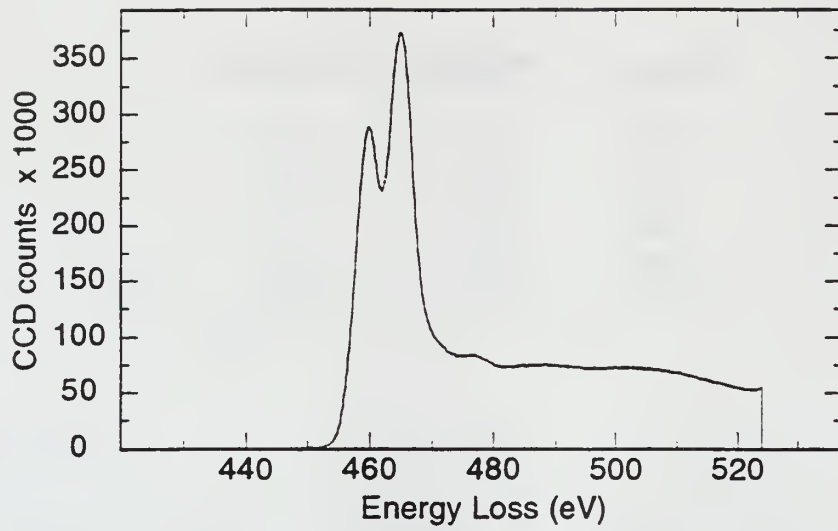Figure 4.30   EDX analysis of inclusion JWY3 - Region A

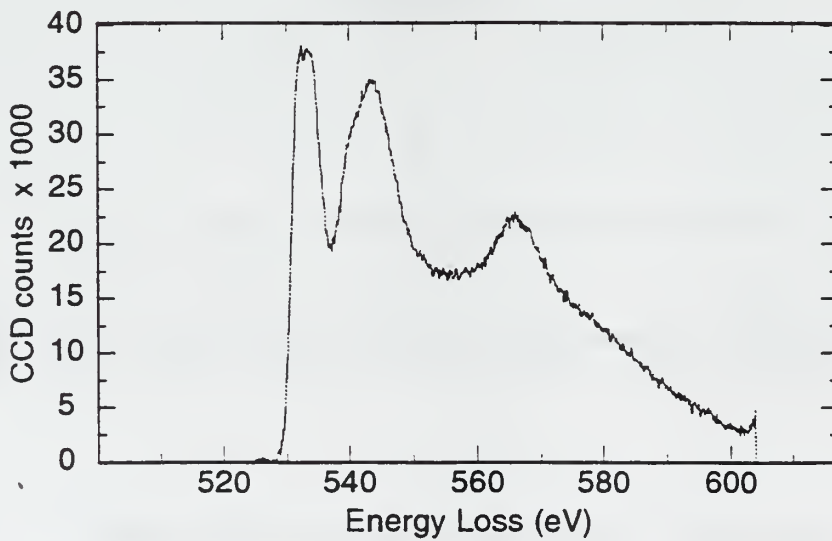Figure 4.31   PEELS analysis of inclusion JWY3 Region A - $Ti_{L2,3}$ spectrum

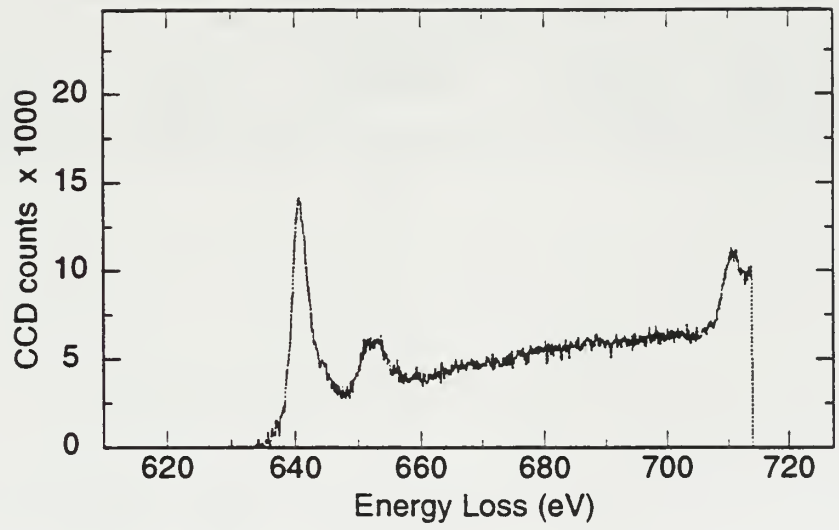Figure 4.32   PEELS analysis of inclusion JWY3 Region A - O_K spectrum

Figure 4.33   PEELS analysis of inclusion JWY3 Region A - $Mn_{L2,3}$ spectrum

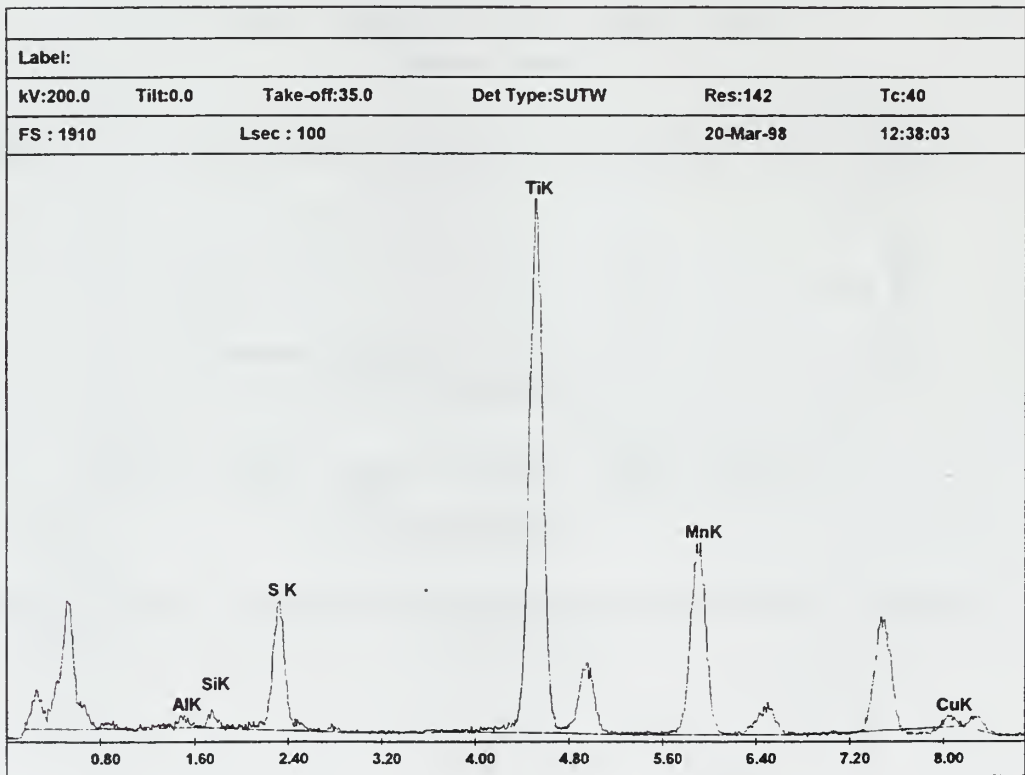| Element	Weight %	Atomic %
AlK	1.1	1.8
SiK	1.1	1.9
S K	11.2	16.1
TiK	59.0	57.0
MnK	26.1	22.0
CuK	1.6	1.1
Total	100.0	100.0

Figure 4.34   EDX analysis of inclusion JWY3 - Region B
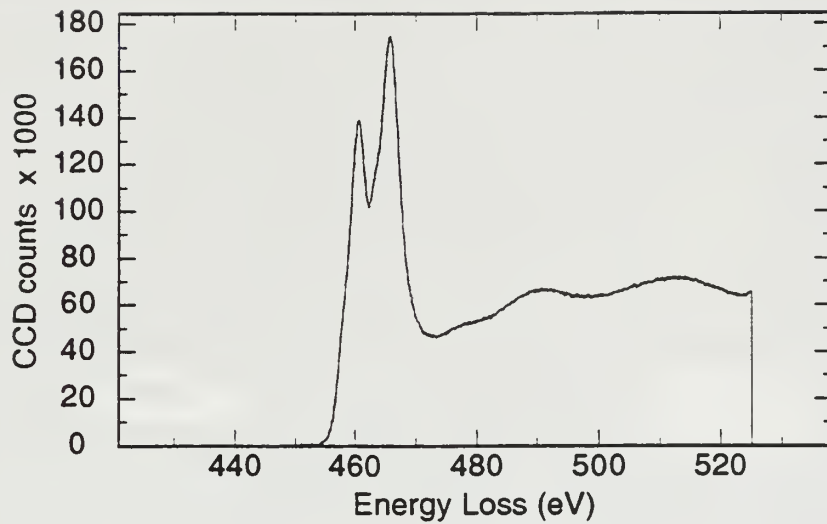
78

Figure 4.35   PEELS analysis of inclusion JWY3 Region B- Ti$_{L2,3}$ spectrum
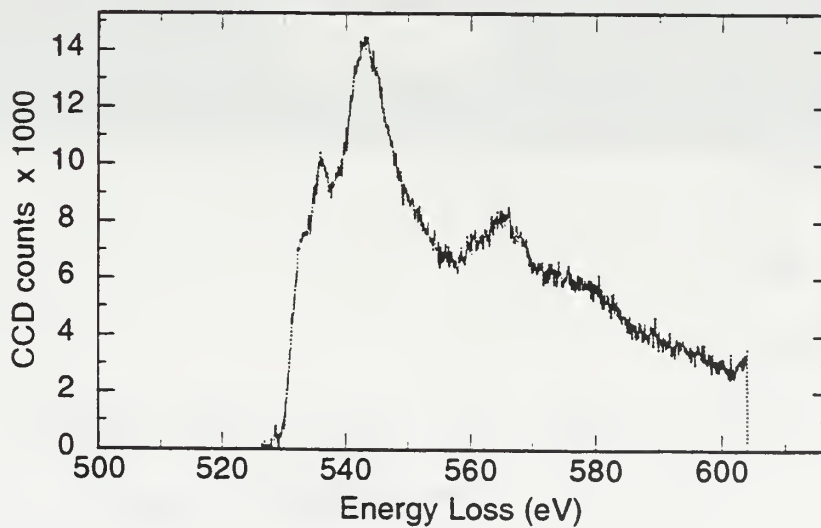

Figure 4.36   PEELS analysis of inclusion JWY3 Region B - O$_K$ spectrum
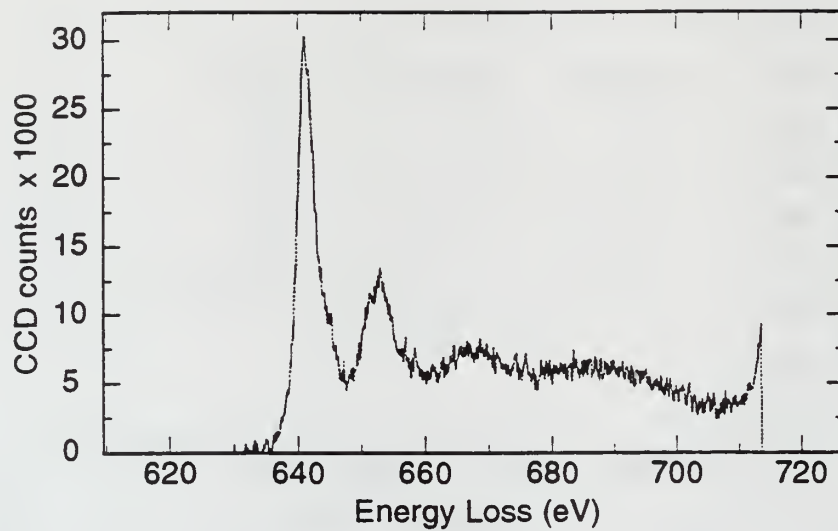
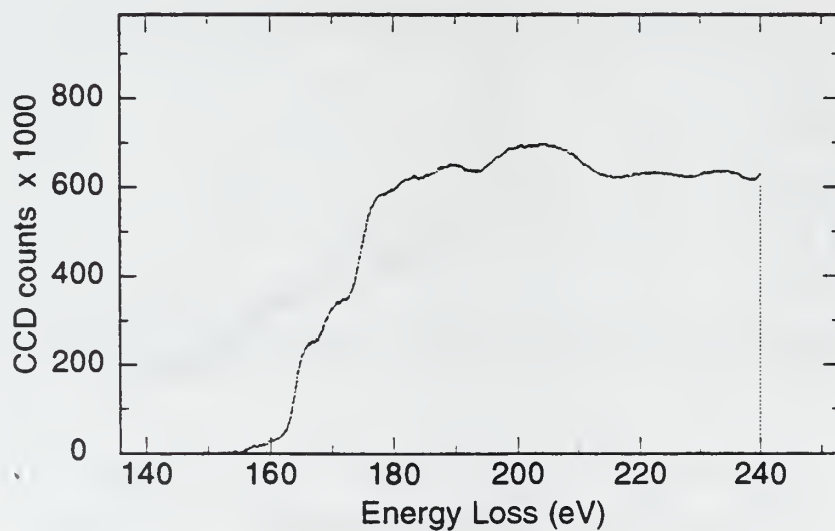Figure 4.37   PEELS analysis of inclusion JWY3 Region B - $Mn_{L2,3}$ spectrum

Figure 4.38   PEELS analysis of inclusion JWY3 Region B - $S_{L2,3}$ spectrum

Figure 4.39   PEELS maps of inclusion JWY3

4.   Sample Z - EDX and PEELS Results

a.   *Inclusion Composition Analysis*

EDX analysis was again performed on twenty-five random inclusions using a probe size of 6 nm in order to determine an average composition of the inclusions. The atomic percentages of the major elements in each inclusion is presented in Table 4.4 along with the average atomic percentage for each element. Figure 4.40 shows a graph comparing the elements overall atomic percent averages. The analysis showed that, titanium was the primary element present followed closely by aluminum, and then small amounts of manganese, silicon, sulfur, and copper. The titanium content in the final weld pass was over 2.5 times that of aluminum, however the atomic percent of titanium to aluminum in the inclusions was almost 1 to 1. This clearly shows the strength of aluminum as a deoxidizer. EDX and PEELS analysis was then conducted on inclusions JWZ1, JWZ2 and JWZ3 in order to determine specific compositions in different areas of the inclusions and identify the possible phases present.

Inclusion	Al	Si	S	Ti	Mn	Cu
1	42.29	0.45	0.00	55.14	1.05	0.87
2	34.78	1.05	0.00	60.87	1.96	1.35
3	40.37	0.99	1.16	52.45	3.61	1.42
4	36.65	0.61	8.20	39.21	9.18	6.14
5	9.63	1.47	28.74	21.09	32.34	6.73
6	32.37	1.20	0.94	58.97	4.42	2.10
7	36.76	1.70	4.99	46.52	4.52	5.51
8	38.36	0.94	0.00	58.37	1.22	1.11
9	45.66	1.22	0.00	49.75	2.49	0.88
10	44.88	1.06	0.00	51.92	1.11	1.03
11	38.91	2.19	0.00	54.72	1.94	2.25
12	50.10	0.82	0.00	45.00	2.28	1.80
13	38.05	0.82	0.00	58.03	1.85	1.26
14	63.05	6.97	0.23	20.93	7.05	1.77
15	44.09	0.89	0.00	52.77	1.07	1.19
16	42.09	2.57	0.20	51.66	0.68	2.80
17	44.12	0.86	0.00	52.16	1.67	1.19
18	34.49	1.75	6.50	40.97	6.21	9.68
19	35.32	1.29	5.6	41.93	1.35	14.51
20	56.91	0.14	0.00	38.38	3.60	0.97
21	59.99	0.62	0.00	35.44	3.16	0.79
22	27.29	9.45	15.36	9.61	26.61	11.69
23	64.03	0.49	0.00	29.97	4.78	0.73
24	44.88	1.35	0.00	49.28	3.69	0.79
25	41.06	0.54	0.53	54.17	1.59	2.11
Average	41.87	1.66	2.90	45.17	5.18	3.23

Table 4.4   Sample Z inclusion analysis - Atomic %
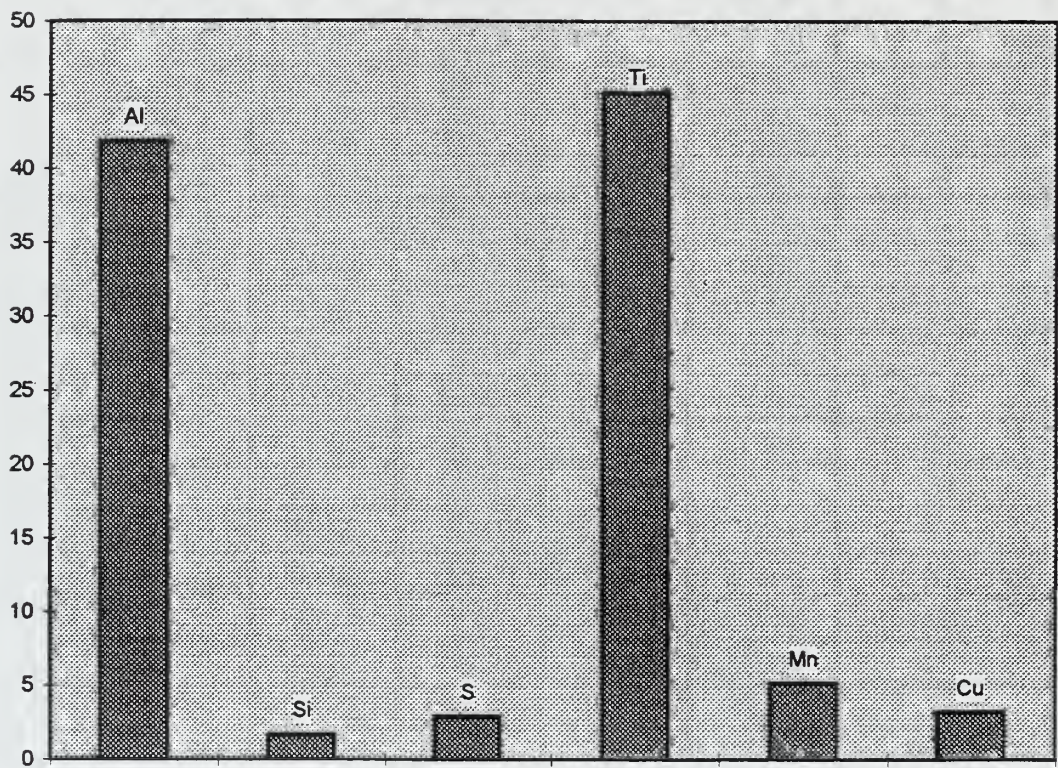
Figure 4.40   Sample Z average inclusion composition - Atomic %

b.   *Inclusion JWZ1*

A TEM micrograph of inclusion JWZ1 is shown in Figure 4.41. The EDX data in Figure 4.42 showed a strong presence of both titanium (39.0%) and aluminum (57.4%) and trace amounts of manganese, silicon, sulfur and copper. This suggested that the main components of this inclusion were Al_2O_3, TiO and/or TiO_2. PEELS analysis was conducted on titanium, oxygen, manganese and aluminum shown in Figures 4.43 through Figure 4.46. The $Ti_{L2,3}$ and O_K spectra again suggested TiO-like coordination over the TiO_2 and the $Al_{L2,3}$ and O_K spectra showed the formation of Al_2O_3. It appeared that both Al_2O_3 and TiO were dispersed homogeneously throughout the inclusion. The weak $Mn_{L2,3}$ edge showed the presence of slight amounts of MnO and/or MnS.
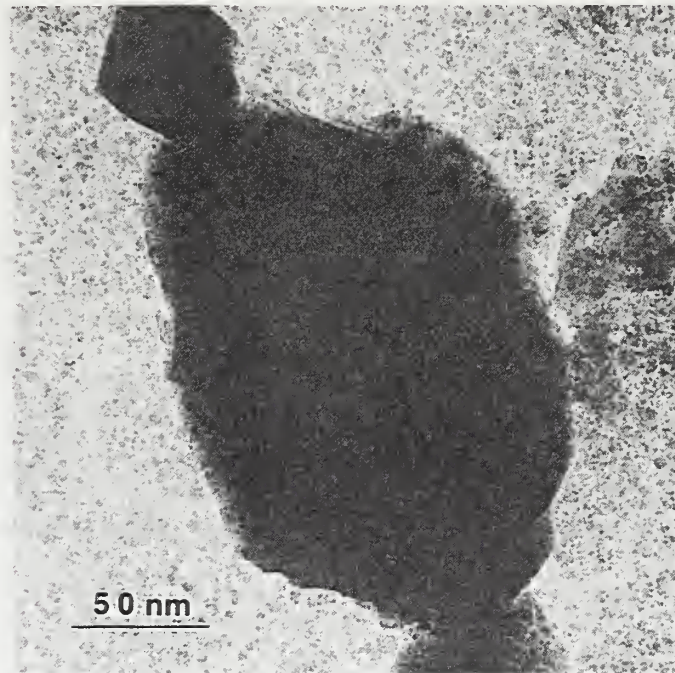

Figure 4.41   TEM micrograph of inclusion JWZ1

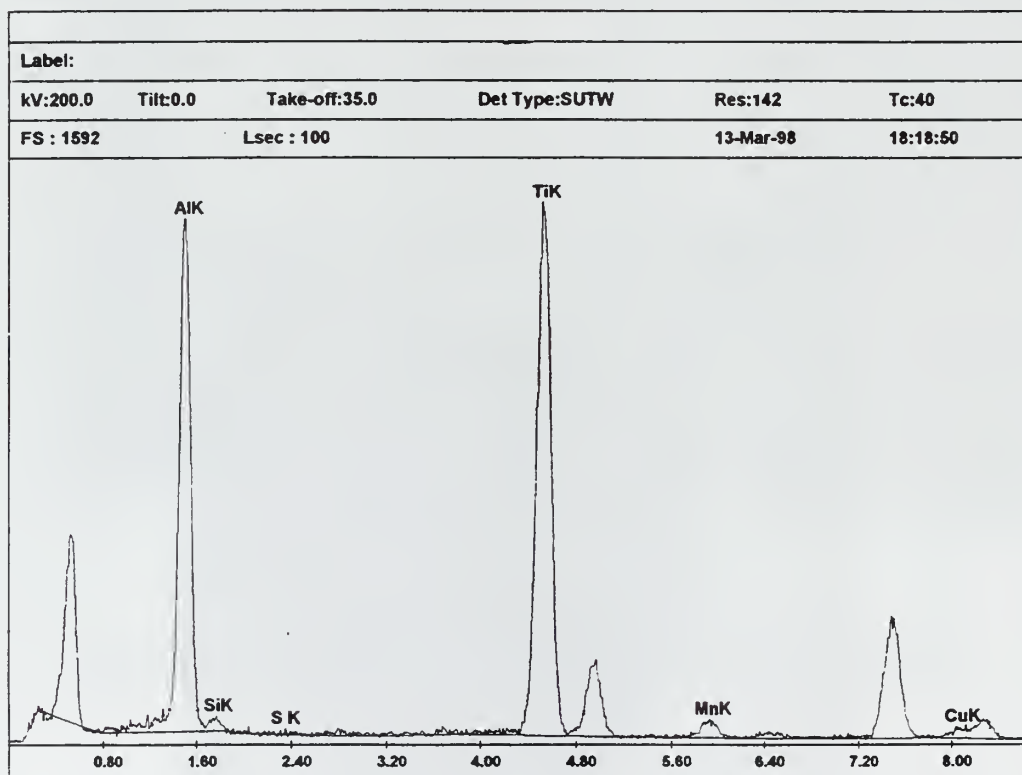| Element	Weight %	Atomic %
AlK	43.2	57.4
SiK	1.0	1.3
S K	0.1	0.1
TiK	52.1	39.0
MnK	2.0	1.3
CuK	1.5	0.9
Total	100.0	100.0

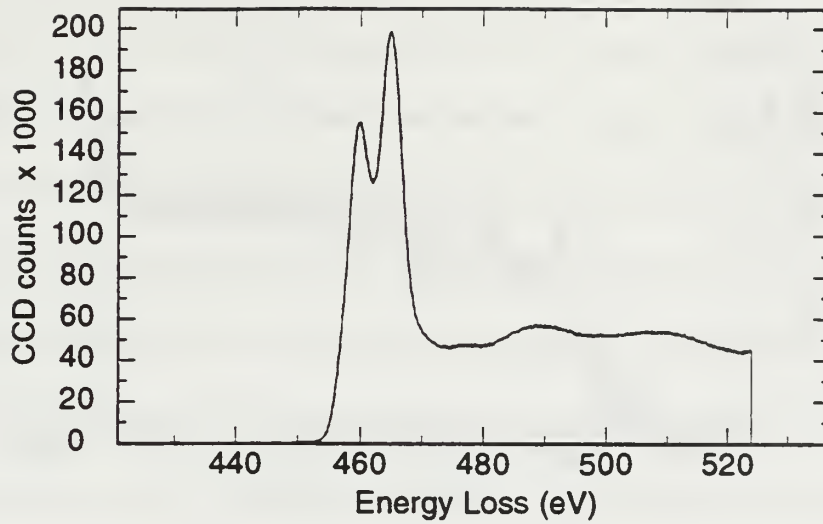Figure 4.42   EDX analysis of inclusion JWZ1

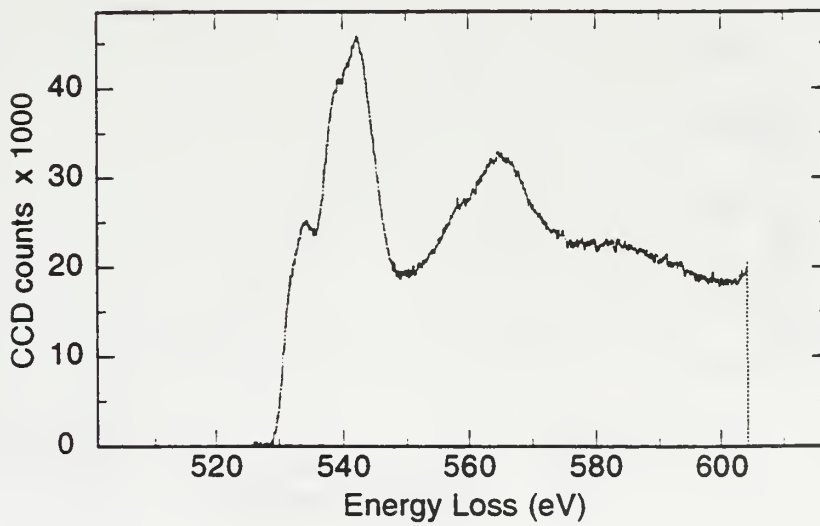Figure 4.43   PEELS analysis of inclusion JWZ1 - $Ti_{L2,3}$ spectrum

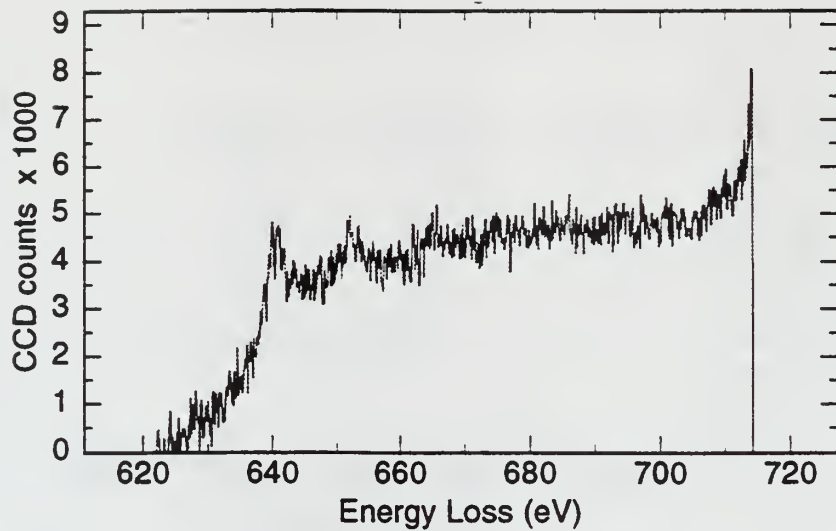Figure 4.44   PEELS analysis of inclusion JWZ1 - O_K spectrum

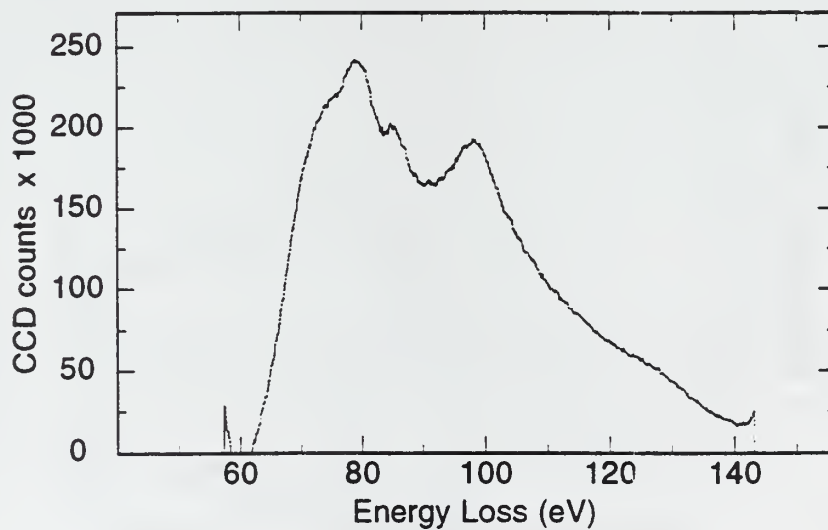Figure 4.45   PEELS analysis of inclusion JWZ1 - $Mn_{L2,3}$ spectrum
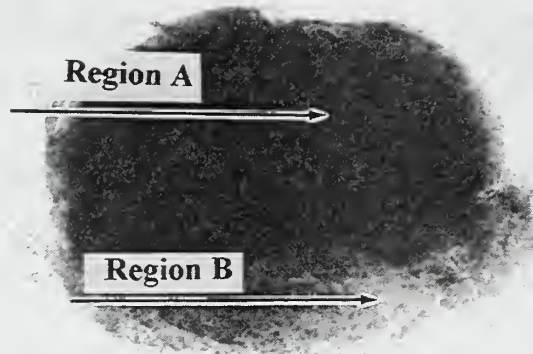

Figure 4.46   PEELS analysis of inclusion JWZ1 - $Al_{L2,3}$ spectrum

88

c.   *Inclusion JWZ2*

Inclusion JWZ2 shown in Figure 4.47 was segregated into Regions A and B, by both EDX and PEELS. EDX on Region A, Figure 4.48, showed a strong presence of aluminum (87.4%) followed by manganese (6.4%) with small amounts of the other elements. PEELS analysis was conducted on titanium, oxygen, manganese and aluminum in Region A, Figures 4.49 through 4.52. The spectra suggested a strong Al_2O_3 component with a much smaller amount of TiO in this region. The manganese edge suggested the presence of MnO and/or MnS. EDX analysis in Region B showed aluminum (55.4%) and titanium (41.3%), Figure 4.53. All other detected elements were present in trace amounts. PEELS data supported the EDX results showing evidence of both the TiO and Al_2O_3 components in the region with a weak $Mn_{L2.3}$ edge, indicating MnO and/or MnS, Figures 4.54 through 4.57.

Figure 4.47   TEM micrograph of inclusion JWZ2

Element	Weight %	Atomic %
AlK	79.2	87.4
SiK	1.8	2.0
S K	0.4	0.4
TiK	4.4	2.7
MnK	11.7	6.4
CuK	2.4	1.1
Total	100.0	100.0

Label:

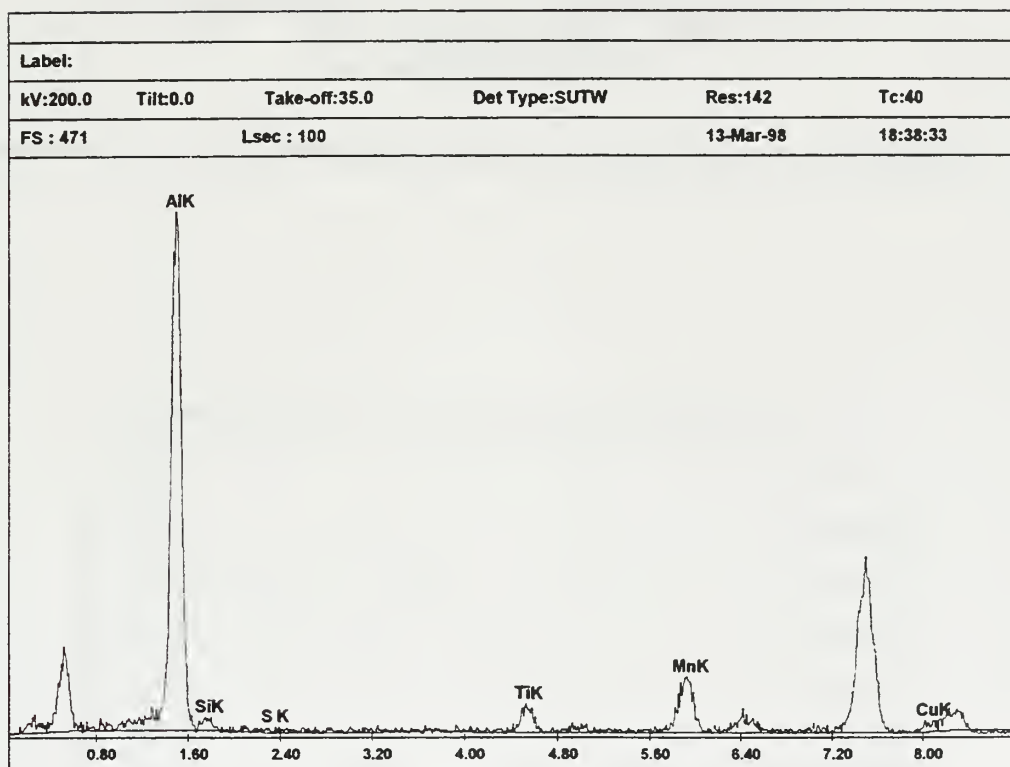| kV:200.0	Tilt:0.0	Take-off:35.0	Det Type:SUTW	Res:142	Tc:40
FS : 471		Lsec : 100		13-Mar-98	18:38:33

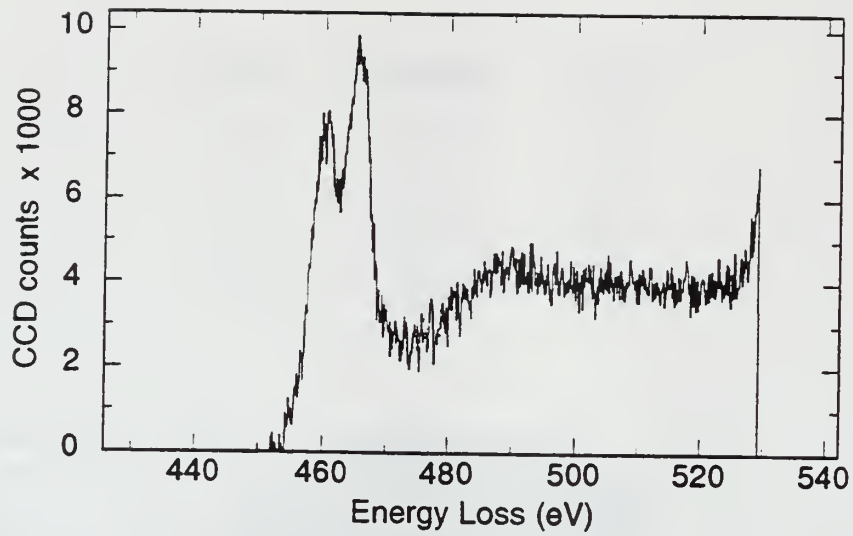Figure 4.48   EDX analysis of inclusion JWZ2 - Region A

91

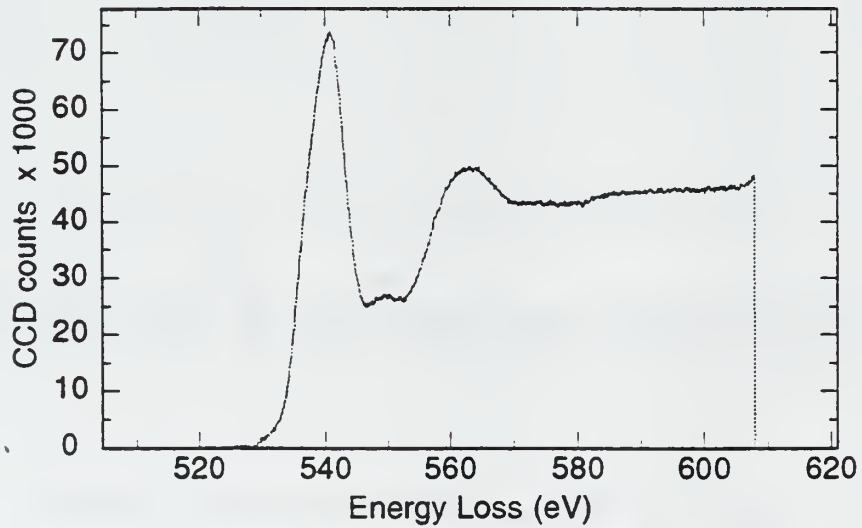Figure 4.49   PEELS analysis of inclusion JWZ2 Region A - Ti$_{L2,3}$ spectrum

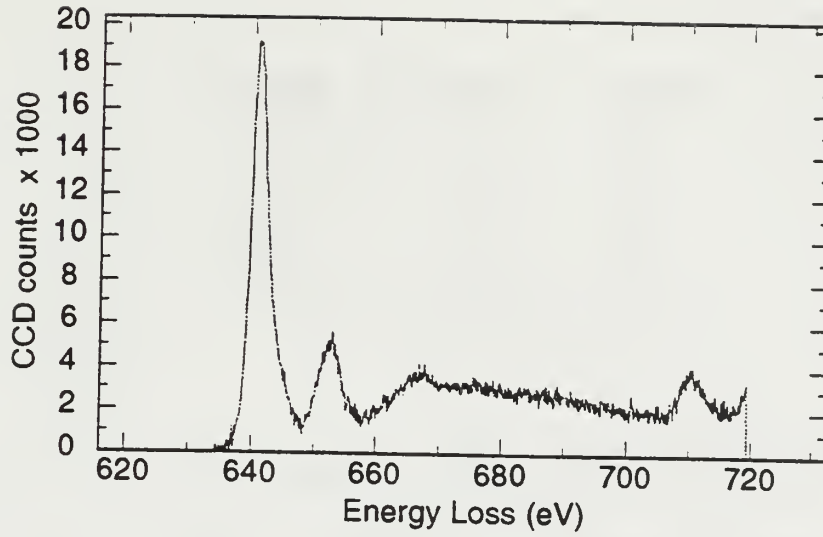Figure 4.50   PEELS analysis of inclusion JWZ2 Region A - O$_K$ spectrum

Figure 4.51   PEELS analysis of inclusion JWZ2 Region A - $Mn_{L2,3}$ spectrum

Figure 4.52   PEELS analysis of inclusion JWZ2 Region A - $Al_{L2,3}$ spectrum

Element	Weight %	Atomic %
AlK	41.2	55.4
SiK	0.8	1.1
S K	0.2	0.2
TiK	54.6	41.3
MnK	1.3	0.8
CuK	2.0	1.1
Total	100.0	100.0

Figure 4.53   EDX analysis of inclusion JWZ2 - Region B

94

Figure 4.54   PEELS analysis of inclusion JWZ2 Region B - $Ti_{L2,3}$ spectrum

Figure 4.55   PEELS analysis of inclusion JWZ2 Region B - O_K spectrum

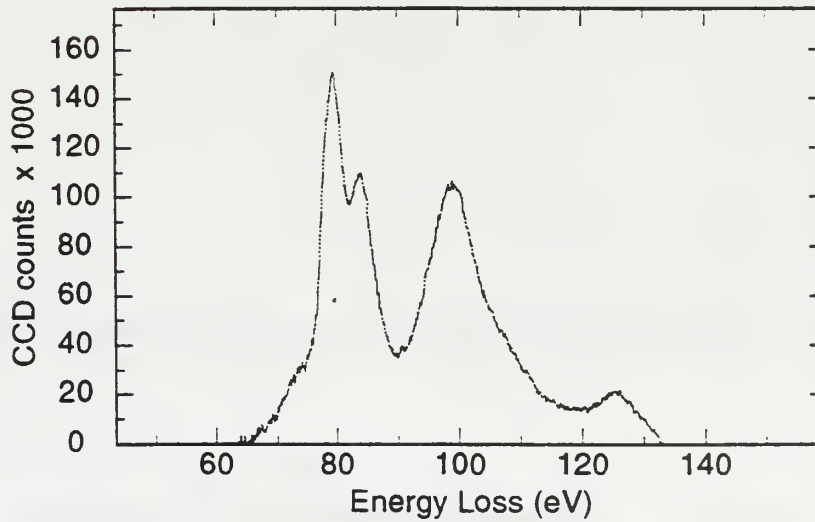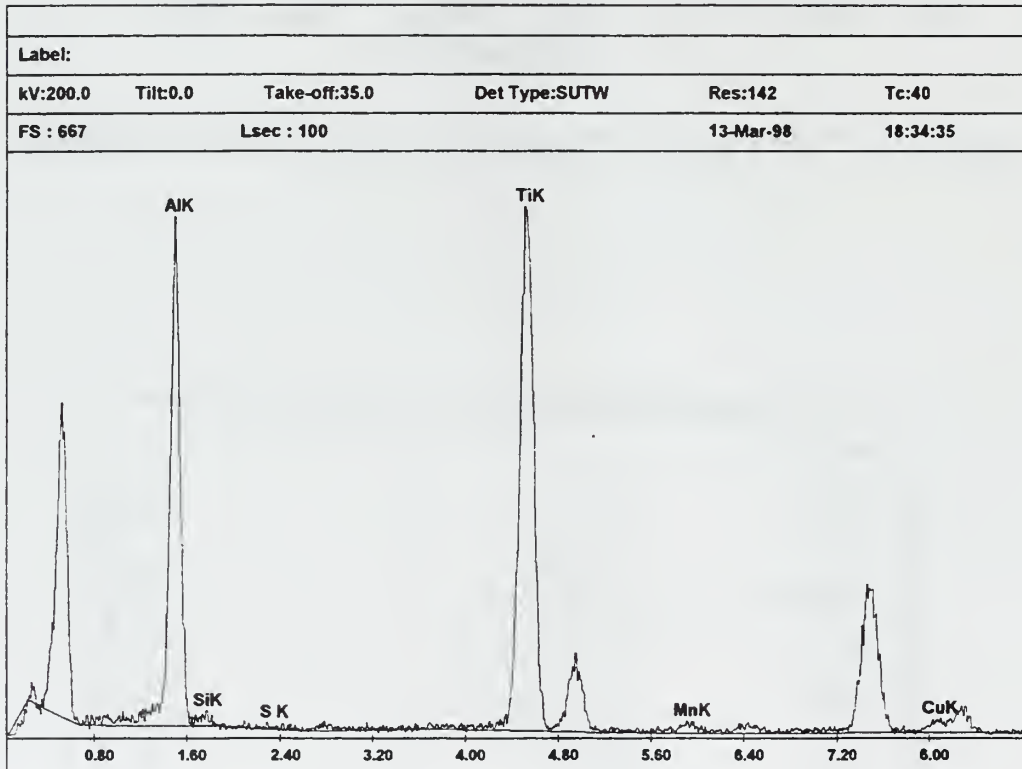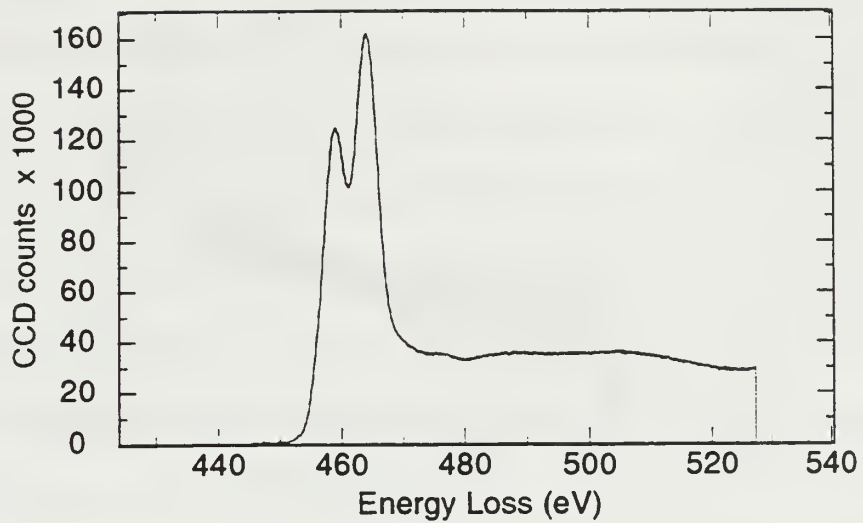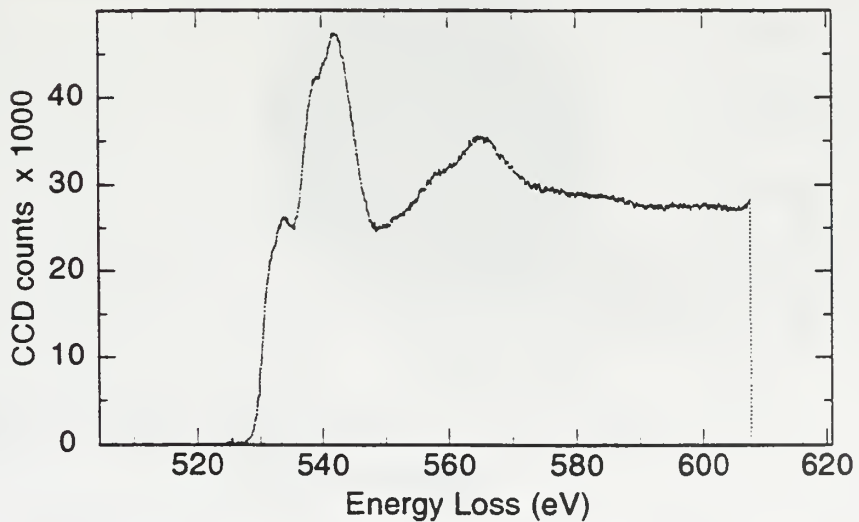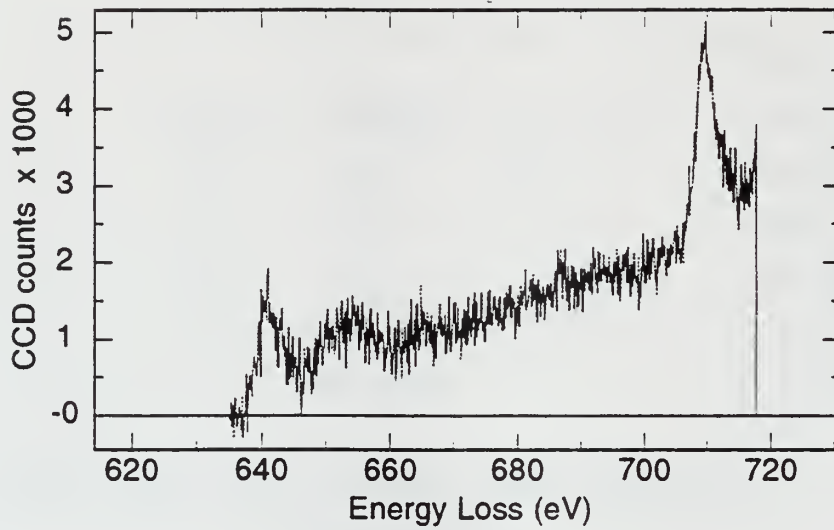Figure 4.56   PEELS analysis of inclusion JWZ2 Region B - Mn$_{L2,3}$ spectrum

Figure 4.57   PEELS analysis of inclusion JWZ2 Region B - Al$_{L2,3}$

d.   *Inclusion JWZ3*

Inclusion JWZ3 is shown in Figure 4.58. EDX analysis, Figure 4.59, confirmed the presence of aluminum (61.3%) and titanium (36.1%) and again trace amounts of the other elements. PEELS analysis was conducted on titanium, oxygen and aluminum, Figures 4.60 through 4.62. The spectra supported a strong presence of both Al_2O_3 and the TiO. PEELS maps of oxygen, titanium and aluminum in the inclusion were produced and are displayed in Figure 4.63. The maps show the TiO and Al_2O_3 to be evenly distributed throughout the inclusion. This suggests that this inclusion is a homogeneous mixture of Al_2O_3 and TiO (either a solid solution or intermediate phase) rather than separate regions of TiO and Al_2O_3.
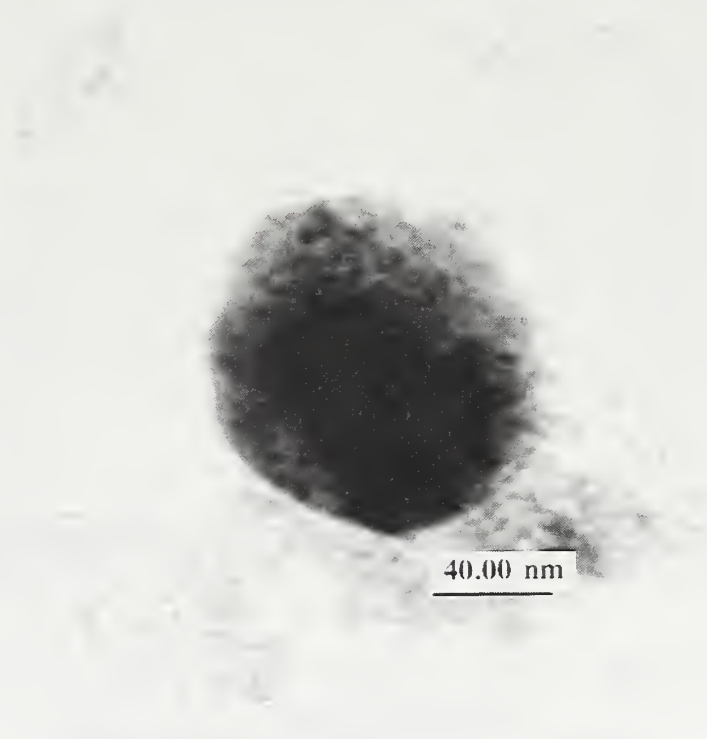
Figure 4.58   TEM micorgraph of inclusion JWZ3

97

Element	Weight %	Atomic %
AlK	47.1	61.3
SiK	0.7	0.9
S K	0.0	0.0
TiK	49.3	36.1
MnK	0.4	0.2
CuK	2.5	1.4
Total	100.0	100.0
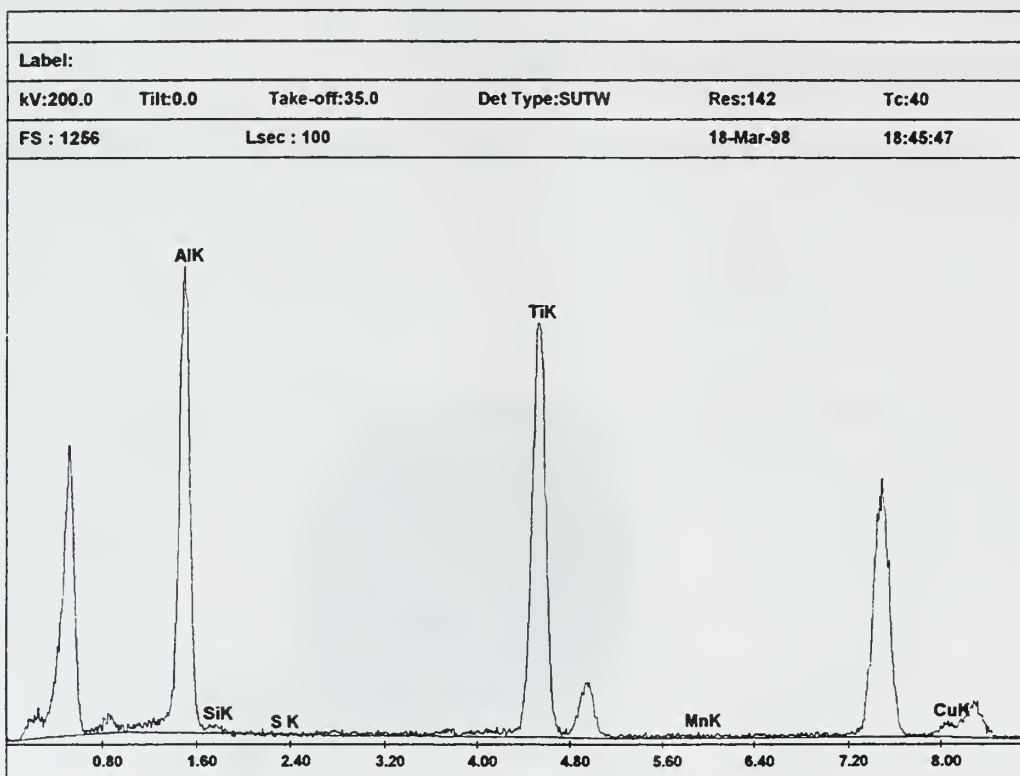
Figure 4.59   EDX analysis of inclusion JWZ3

98

Figure 4.60   PEELS analysis of inclusion JWZ3 - $Ti_{L2,3}$ spectrum

Figure 4.61   PEELS analysis of inclusion JWZ3 - O_K spectrum
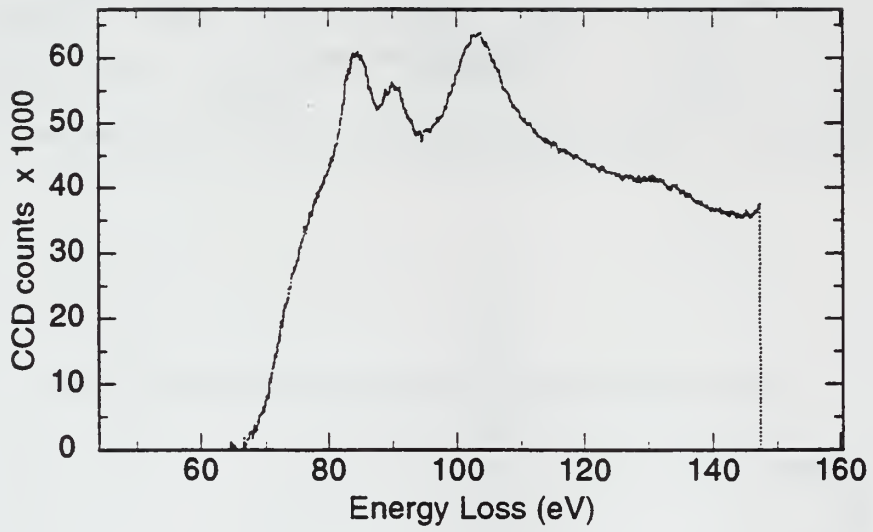
Figure 4.62   PEELS analysis of inclusion JWZ3 - Al$_{L2,3}$ spectrum
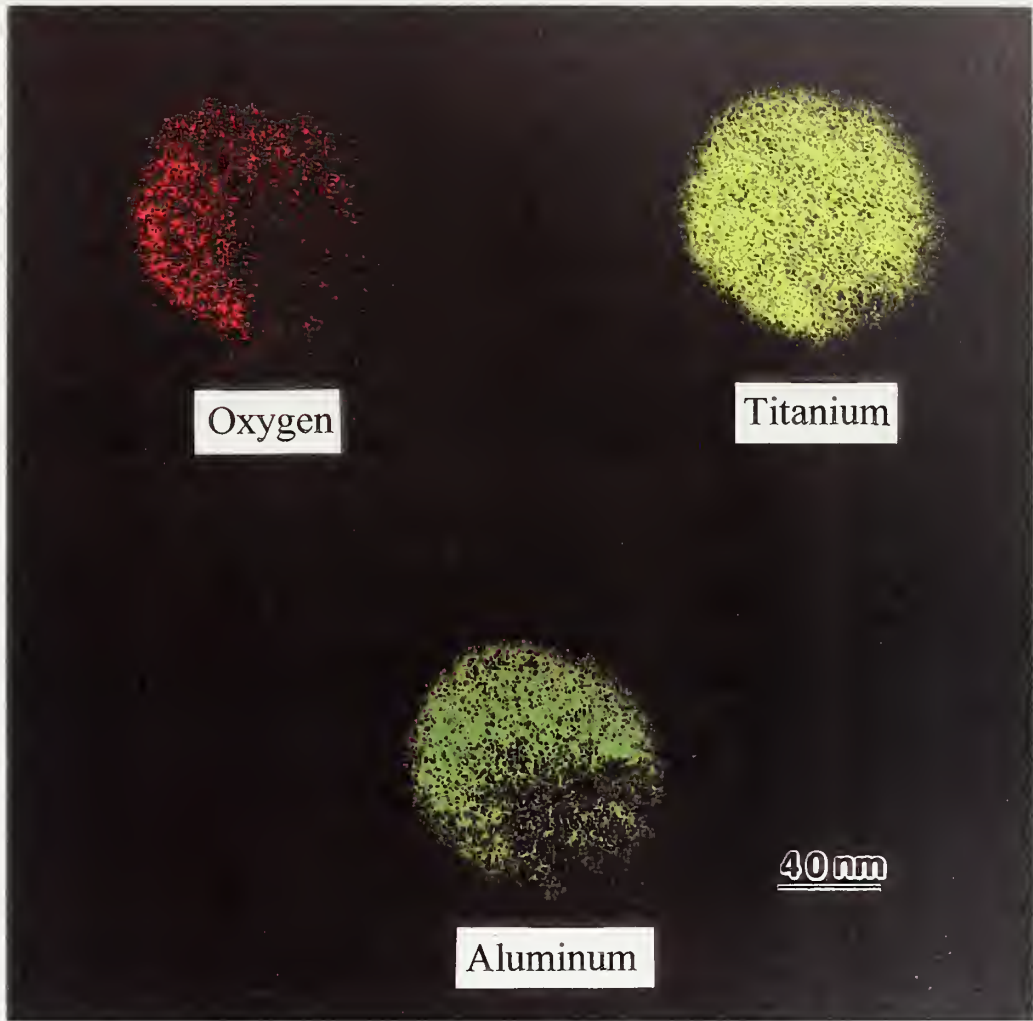
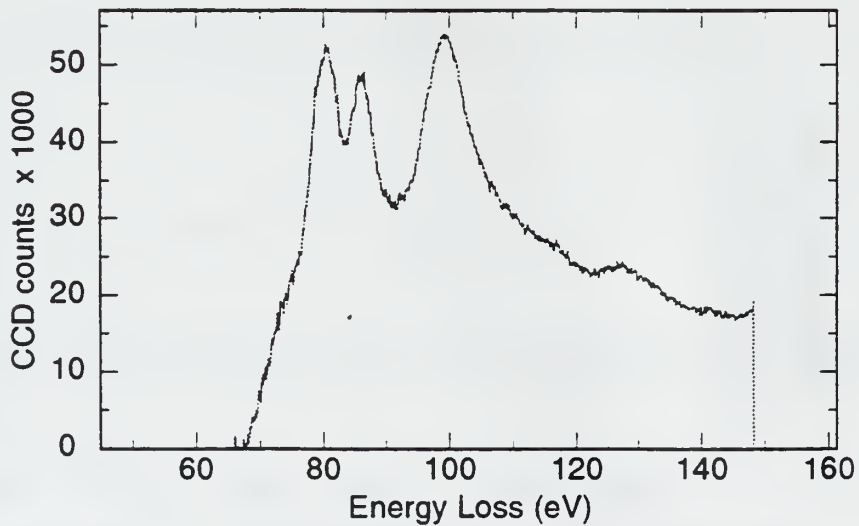Figure 4.63   PEELS maps of inclusion JWZ3

Figure 4-51 PECS S page of function 1W23

5. Sample V - EDX and PEELS Results

a. *Inclusion Composition Analysis*

EDX analysis was again performed on twenty-five random inclusions using a probe size of 6 nm in order to determine an average composition of the inclusions. The atomic percentages of the major elements in each 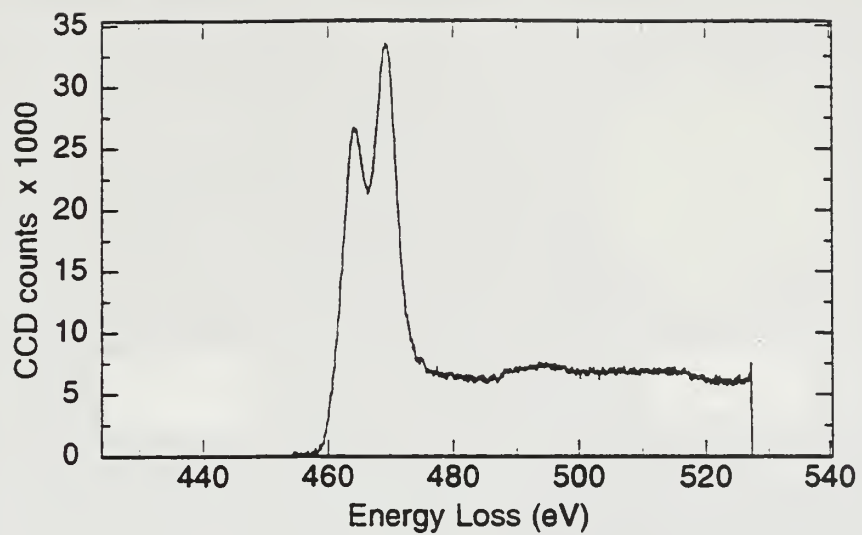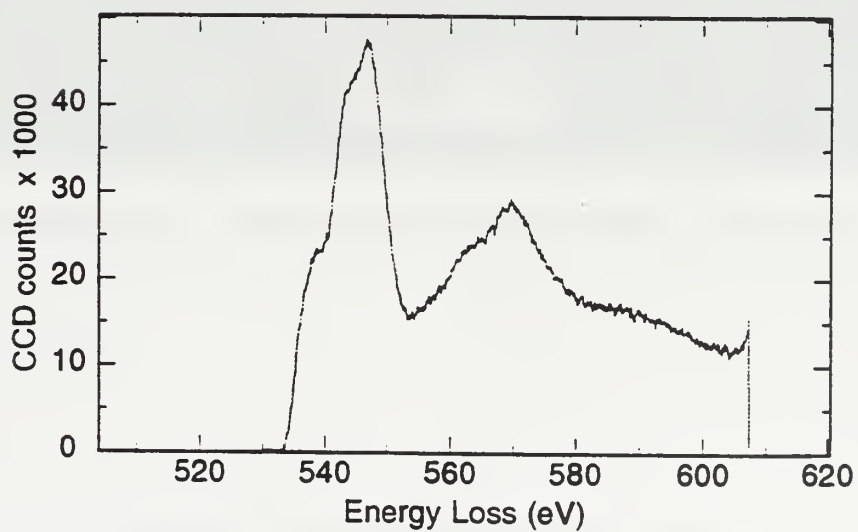inclusion is presented in Table 4.5 along with the average atomic percentage for each element. Figure 4.64 shows a graph comparing the elements overall atomic percent averages. The analysis showed that, aluminum was the primary element present followed titanium, and then small amounts of manganese, silicon, sulfur, and copper. The aluminum to titanium content in the final weld pass was about 1 to 1 but the atomic percent of titanium to aluminum in the inclusions was almost 2 to 1. This again shows the strength of aluminum as a deoxidizer. EDX and PEELS analysis was then conducted on inclusions JWV1, JWV2 and JWV3 in order to determine specific compositions in different areas of the inclusions and identify the possible phases present.

Inclusion	Al	Si	S	Ti	Mn	Cu
1	47.92	5.83	7.46	29.64	4.62	4.53
2	52.84	0.84	8.56	33.74	1.57	2.45
3	66.43	2.52	5.00	23.23	2.17	0.65
4	63.79	2.69	3.47	21.95	6.45	1.65
5	47.82	0.03	2.24	30.47	13.43	6.01
6	68.33	2.27	1.55	25.42	0.56	1.87
7	75.29	2.83	4.76	16.26	0.35	0.51
8	48.42	2.08	0.34	40.78	3.05	5.33
9	52.69	2.19	12.84	22.54	4.62	5.21
10	43.56	0.21	7.64	42.72	4.01	1.86
11	55.83	2.57	6.36	24.64	6.17	4.43
12	64.07	0.73	4.86	29.04	0.43	0.87
13	64.16	5.62	2.73	27.28	0.17	0.04
14	59.47	0.48	9.53	27.84	1.98	0.70
15	39.67	4.74	7.77	45.75	0.52	1.55
16	75.02	0.64	5.48	15.43	1.69	1.74
17	49.78	3.69	0.79	44.34	0.53	0.87
18	58.33	3.11	5.42	21.93	8.34	2.87
19	78.49	2.33	3.73	11.23	2.06	2.16
20	48.63	3.49	1.26	43.56	2.24	0.82
21	63.64	2.91	8.56	23.14	0.44	1.31
22	59.07	3.94	2.46	26.74	4.30	3.49
23	56.51	4.23	2.48	32.04	4.27	0.47
24	57.65	3.75	2.27	25.77	5.55	5.01
25	48.03	1.05	0.68	43.51	5.01	1.72
Average	57.82	2.59	4.73	29.16	3.38	2.32

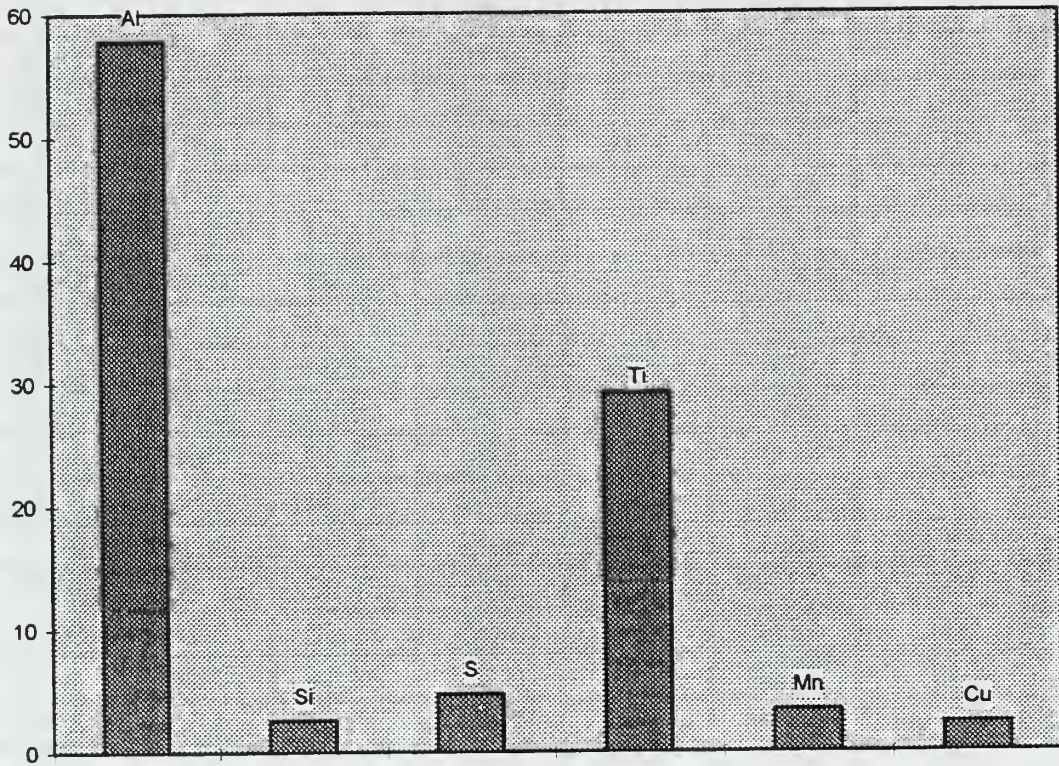Table 4.5   Sample V inclusion analysis - Atomic %

103

Figure 4.64   Sample V average inclusion composition - Atomic %

b. *Inclusion JWV1*

Inclusion JWV1 shown in Figure 4.65 was analyzed in two areas, Region A and Region B, by both EDX and PEELS. Region A appeared to be more spherical and separated from the more faceted structure of Region B. EDX on Region A, Figure 4.66, showed the strong presence of aluminum (89.0%) followed by titanium (6.3%) with low amounts of the other elements. PEELS analysis was conducted on titanium, oxygen and aluminum in Region A, Figures 4.67 through 4.69. The spectra suggested a large Al_2O_3 component with a small amount of TiO. EDX analysis in Region B showed titanium (63.7%) and aluminum (33.8%), Figure 4.70. All other detected elements were present in trace amounts. PEELS data, Figures 4.71 through 4.74, showed the Al_2O_3 presence to be much weaker. A nitrogen edge was also detected showing the presence of a TiN with the fcc lattice structure which explains the cubic facets in the micrograph Figure 4.65. It appeared that the aluminum reacted with almost all of the oxygen and that titanium then reacted with some oxygen but when this was consumed it reacted with dissolved nitrogen instead.

Figure 4.65   TEM micrograph of inclusion JWV1

Element	Weight %	Atomic %
AlK	82.0	89.0
SiK	1.2	1.2
S K	0.3	0.3
TiK	10.3	6.3
MnK	3.8	2.0
CuK	2.3	1.1
Total	100.0	100.0

Label:					
kV:200.0	Tilt:0.0	Take-off:35.0	Det Type:SUTW	Res:142	Tc:40
FS : 4306		Lsec : 100		6-Apr-98	14:55:31

AlK

SiK   S K   TiK   MnK   CuK

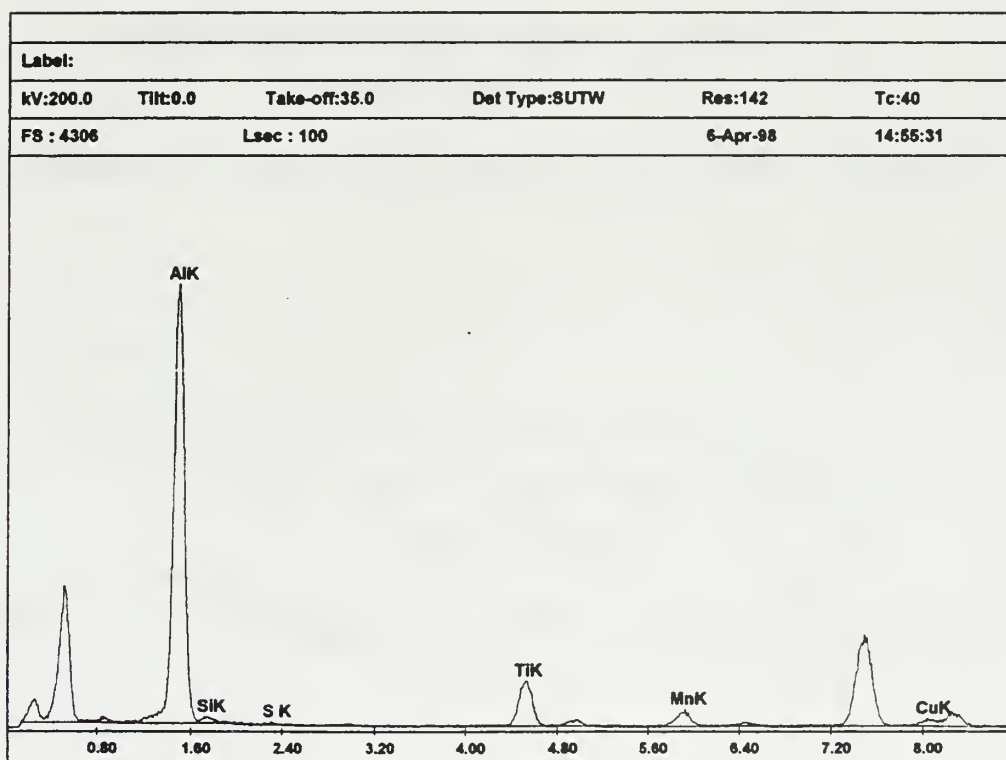0.80   1.60   2.40   3.20   4.00   4.80   5.60   6.40   7.20   8.00

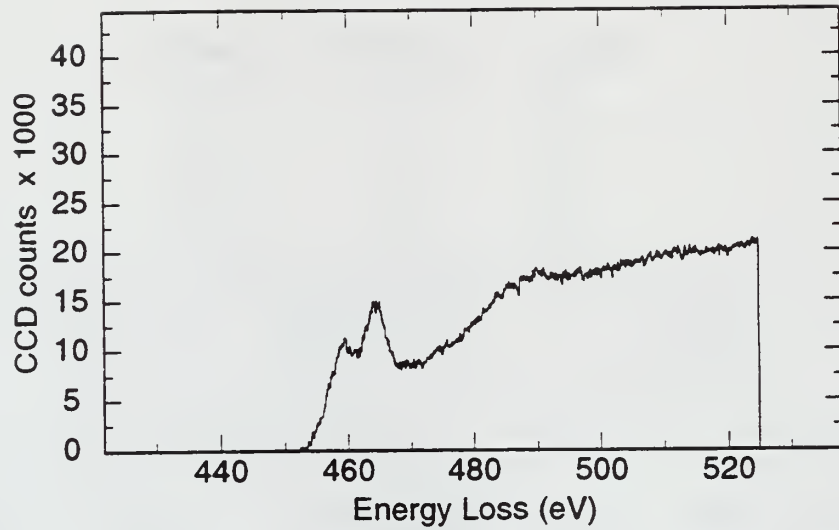Figure 4.66   EDX analysis of inclusion JWV1 - Region A

Figure 4.67   PEELS analysis of inclusion JWV1 Region A - $Ti_{L2,3}$ spectrum
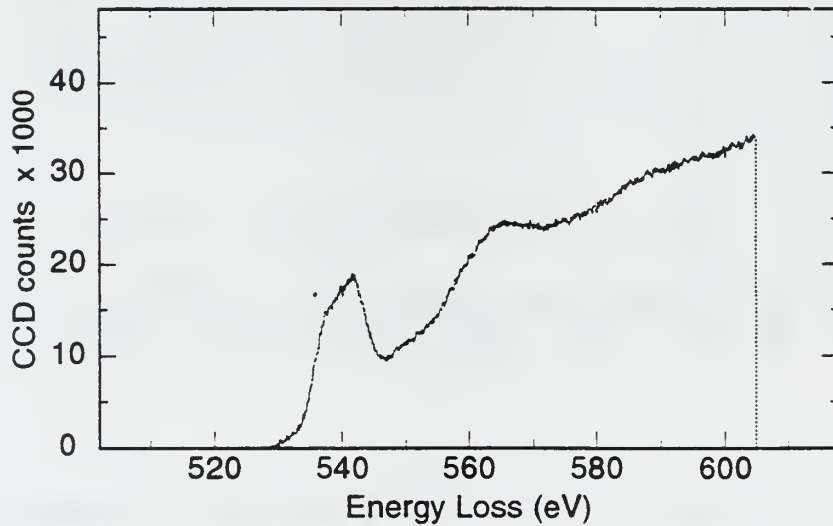

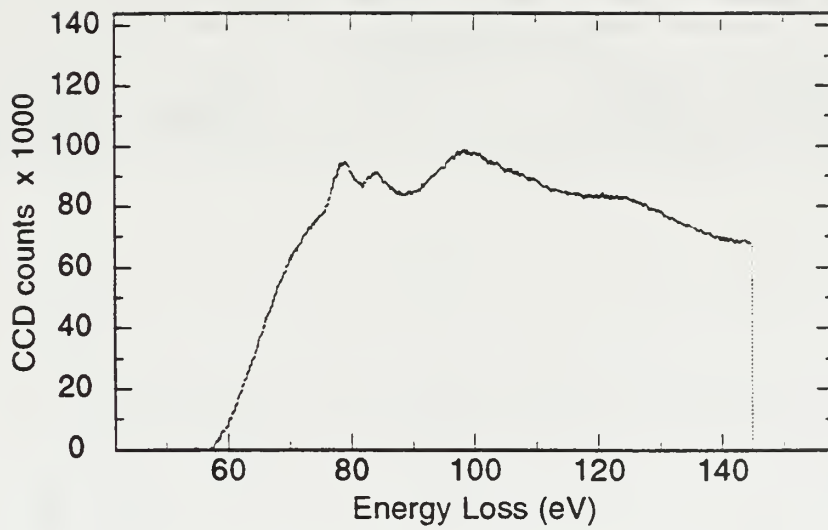Figure 4.68   PEELS analysis of inclusion JWV1 Region A - O_K spectrum

Figure 4.69   PEELS analysis of inclusion JWV1 Region A - $Al_{L2,3}$ spectrum

Element	Weight %	Atomic %
AlK	22.4	33.8
SiK	0.8	1.1
S K	0.2	0.2
TiK	74.9	63.7
MnK	0.1	0.1
CuK	1.7	1.1
Total	100.0	100.0

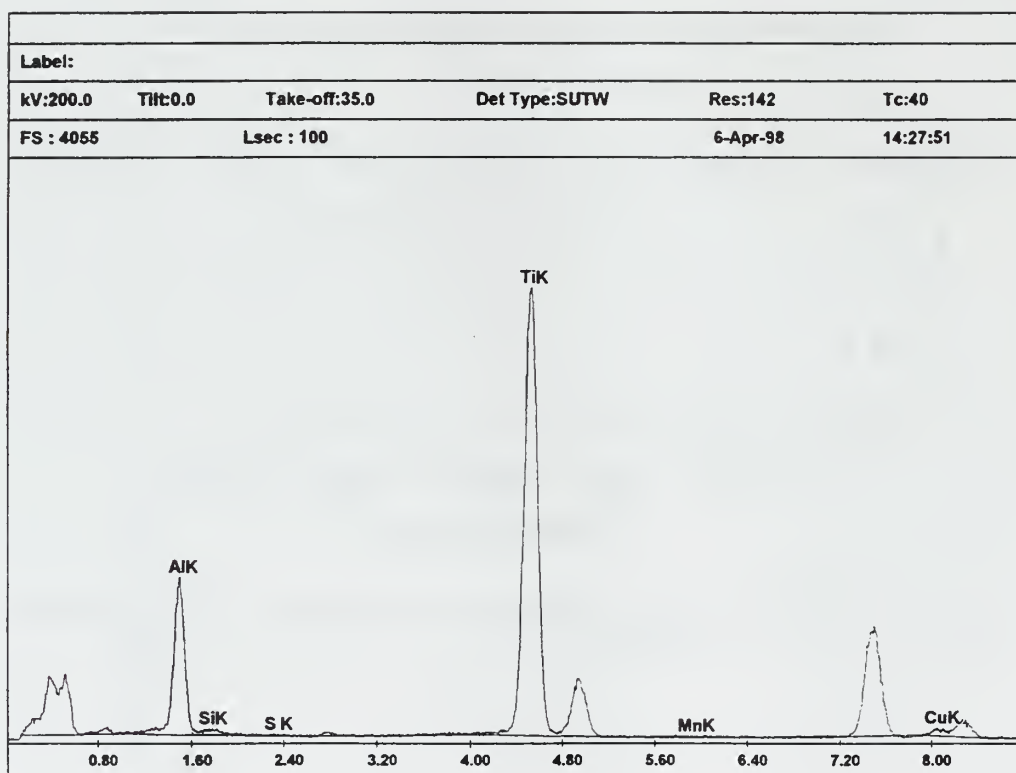| Label:					
kV:200.0	Tilt:0.0	Take-off:35.0	Det Type:SUTW	Res:142	Tc:40
FS : 4055		Lsec : 100		6-Apr-98	14:27:51

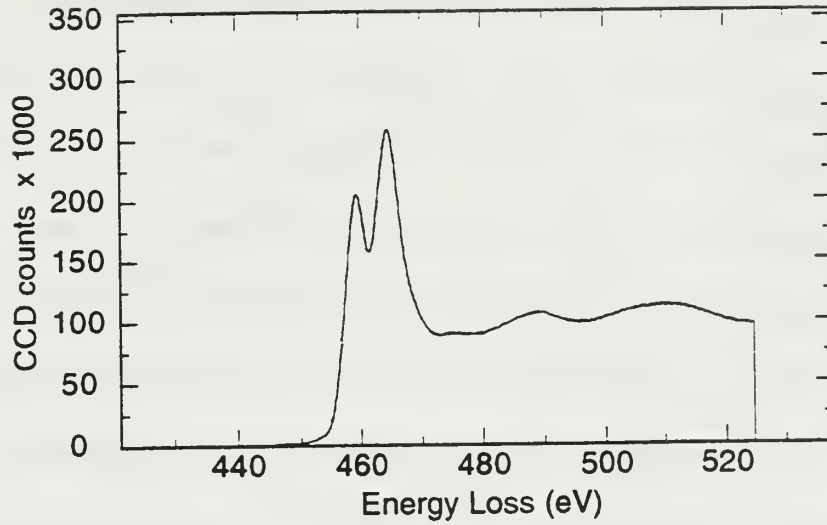Figure 4.70   EDX analysis of inclusion JWV1 - Region B

110

Figure 4.71   PEELS analysis of inclusion JWV1 Region B- Ti$_{L2,3}$ spectrum
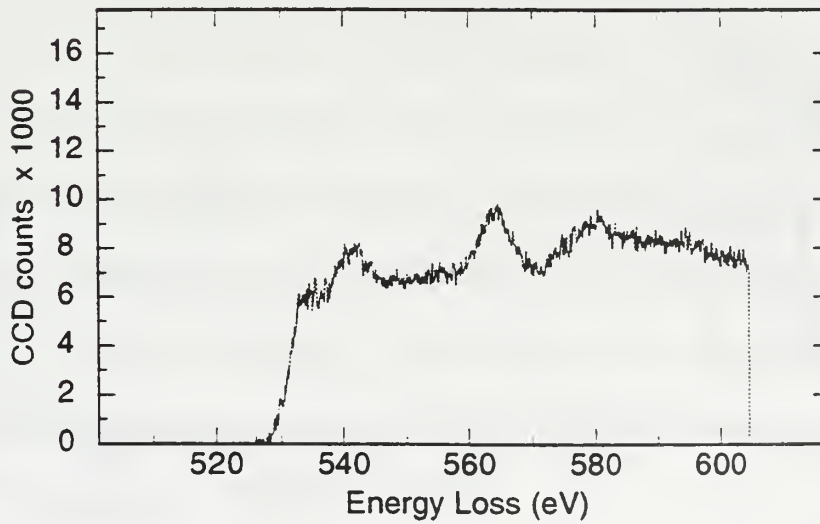

Figure 4.72   PEELS analysis of inclusion JWV1 Region B - O$_K$ spectrum
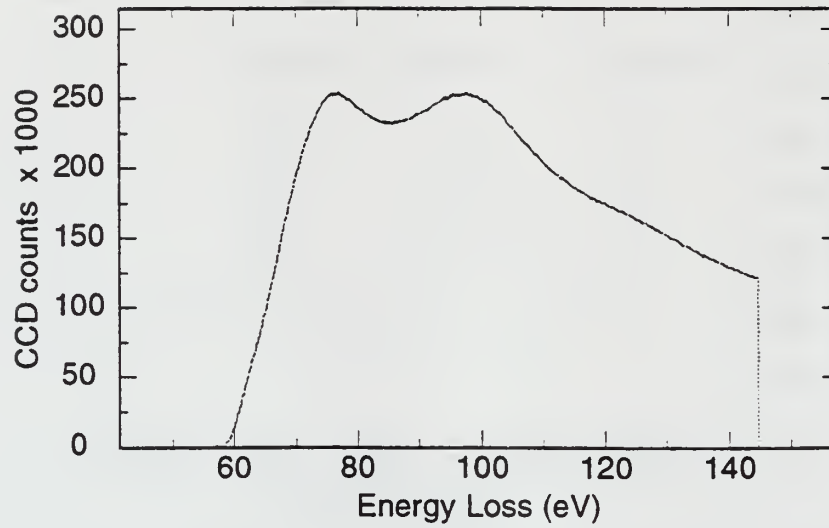
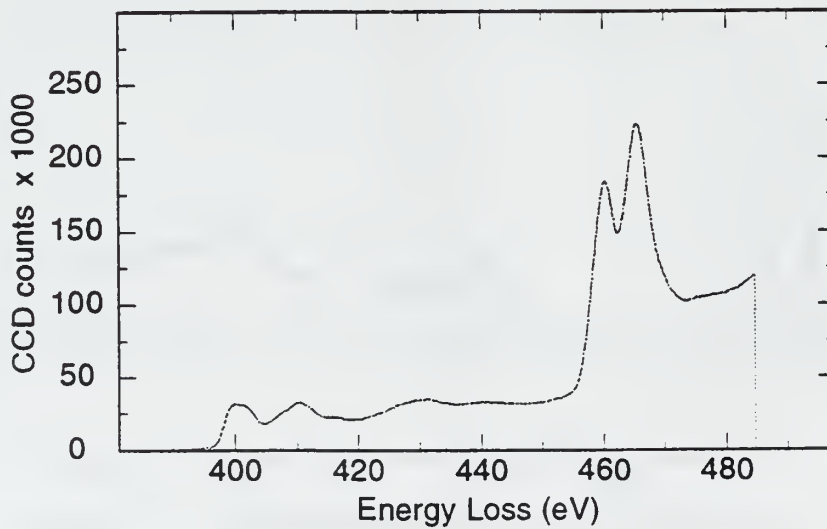Figure 4.73   PEELS analysis of inclusion JWV1 Region B - $Al_{L2,3}$ spectrum

Figure 4.74   PEELS analysis of inclusion JWV1 Region B - N_K spectrum

112

c. *Inclusion JWV2*

Inclusion JWV2 shown in Figure 4.75 was segregated into three Regions A, B and C, each of which were analyzed by both EDX and PEELS. The inclusion was probed in different regions because it appeared to have a layered structure. EDX on Region A, Figure 4.76, showed the presence of aluminum (66.0%) followed by titanium (27.8%) and again low amounts of the other elements. PEELS analysis was conducted on titanium, oxygen, manganese and aluminum in Region A, Figures 4.77 through 4.80. The spectra supported a strong component of Al_2O_3 together with a weaker one of TiO with an $Mn_{L2,3}$ edge indicating the presence of MnO and/or MnS. EDX analysis in Region B showed aluminum (93.0%) and very small amounts of titanium (3.6%), Figure 4.81. All other elements were again present in trace amounts. PEELS data, Figures 4.82 through 4.85, showed the Al_2O_3 like coordination to be the strongest formation followed by a weaker TiN formation. Both the O_K and $Al_{L2,3}$ spectra exhibited a different ELNES than previously observed in samples Y and Z this may be due to additional reactions between the Al_2O_3 and the TiO and/or MnO. EDX analysis on Region C showed aluminum (21.5%), manganese (38.3%) and sulfur (35.2%) to be the dominant elements, Figure 4.86. PEELS analysis, Figures 4.87 through 4.91 supported EDX results indicating Al_2O_3 to be the primary reaction phase and MnS to be the secondary phase. A very small amount of TiO or possibly TiN was also detected. This inclusion was very segregated in its compositions and demonstrated the complexity of deoxidation and desulfurization reactions in the inclusions.

Region A

Region B

Region C

0.10 μm
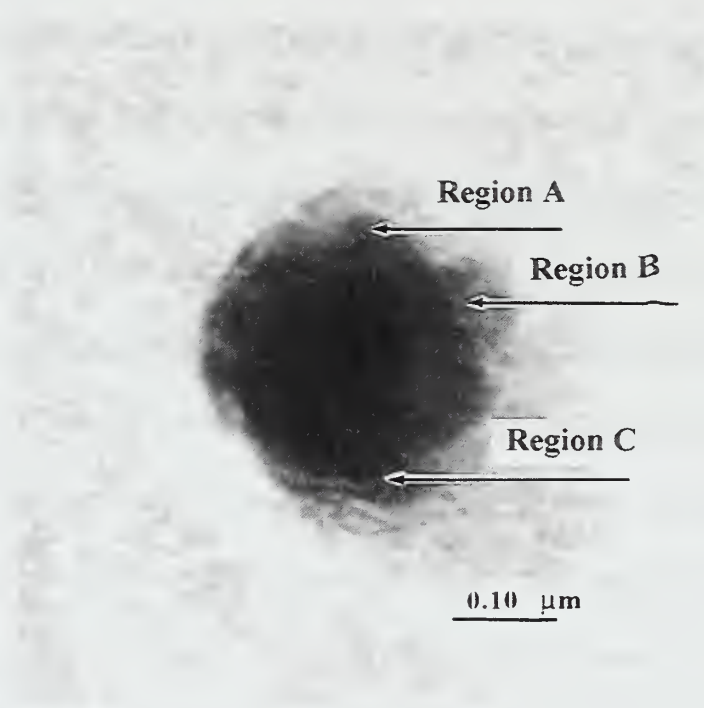
Figure 4.75   TEM micrograph of inclusion JWV2

Element	Weight %	Atomic %
AlK	52.4	66.0
SiK	2.0	2.4
S K	0.1	0.1
TiK	39.1	27.8
MnK	3.8	2.3
CuK	2.6	1.4
Total	100.0	100.0

Label:					
kV:200.0	Tilt:0.0	Take-off:35.0	Det Type:SUTW	Res:142	Tc:40
FS : 2179		Lsec : 100		6-Apr-98	15:26:18

Figure 4.76   EDX analysis of inclusion JWV2 - Region A

Figure 4.77   PEELS analysis of inclusion JWV2 Region A - Ti$_{L2,3}$ spectrum

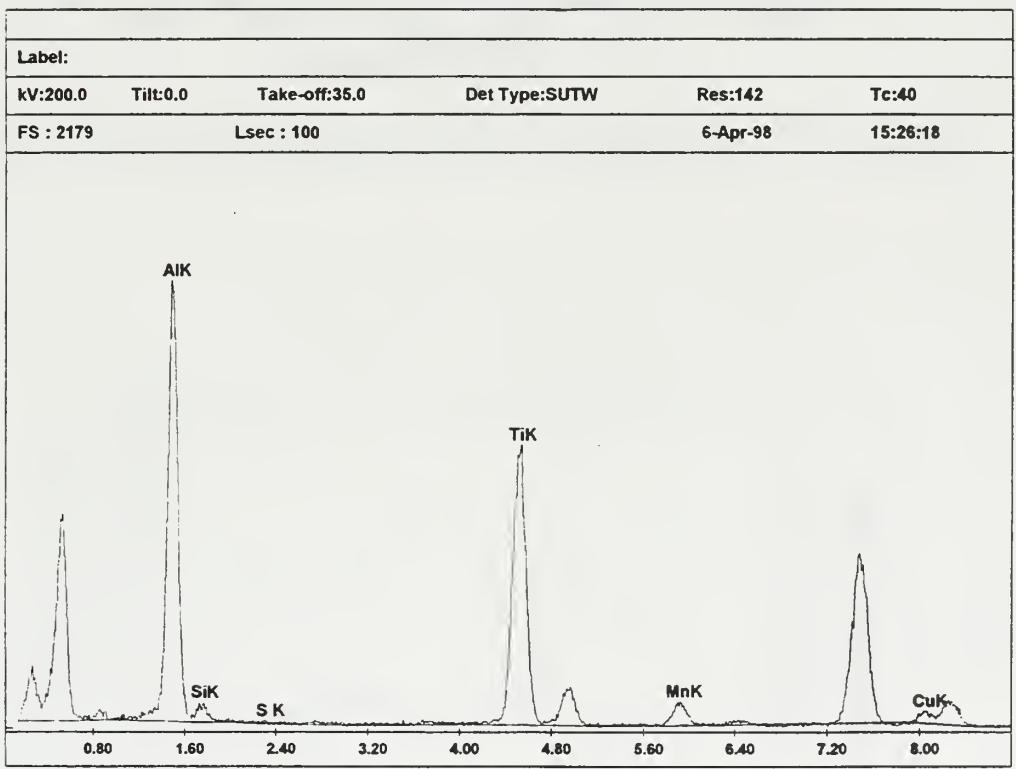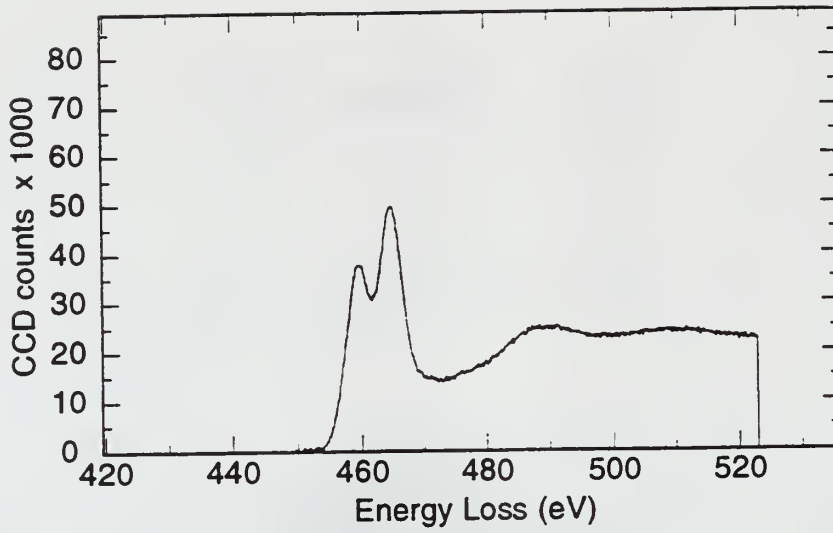Figure 4.78   PEELS analysis of inclusion JWV2 Region A - O$_K$ spectrum

Figure 4.79   PEELS analysis of inclusion JWV2 Region A - $Mn_{L2,3}$ spectrum

Figure 4.80   PEELS analysis of inclusion JWV2 Region A - $Al_{L2,3}$ spectrum

117

Element	Weight %	Atomic %
AlK	88.4	93.0
SiK	1.3	1.3
S K	0.2	0.2
TiK	6.1	3.6
MnK	0.8	0.4
CuK	3.2	1.4
Total	100.0	100.0

Label:					
kV:200.0	Tilt:0.0	Take-off:35.0	Det Type:SUTW	Res:142	Tc:40
FS : 1614		Lsec : 100		6-Apr-98	15:12:21

Figure 4.81   EDX analysis of inclusion JWV2 - Region B

Figure 4.82   PEELS analysis of inclusion JWV2 Region B - $Ti_{L2,3}$ spectrum
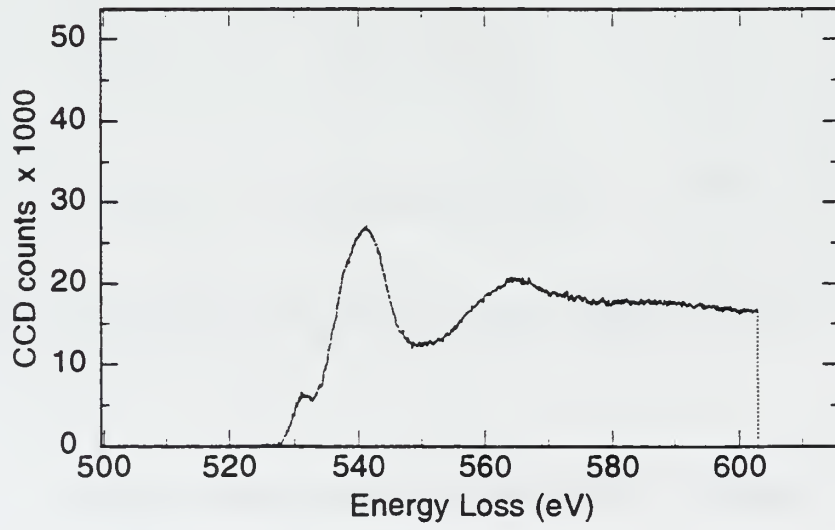

Figure 4.83   PEELS analysis of inclusion JWV2 Region B - O_K spectrum

119

Figure 4.84   PEELS analysis of inclusion JWV2 Region B - $Al_{L2,3}$ spectrum

Figure 4.85   PEELS analysis of inclusion JWV2 Region B - N_K spectrum
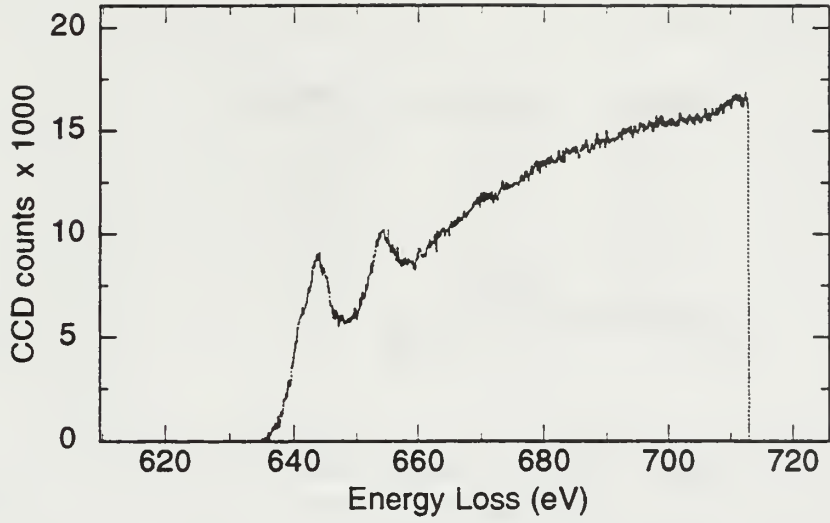
Element	Weight %	Atomic %
AlK	14.3	21.5
SiK	0.9	1.4
S K	27.8	35.2
TiK	1.4	1.2
MnK	51.8	38.3
CuK	3.8	2.4
Total	100.0	100.0
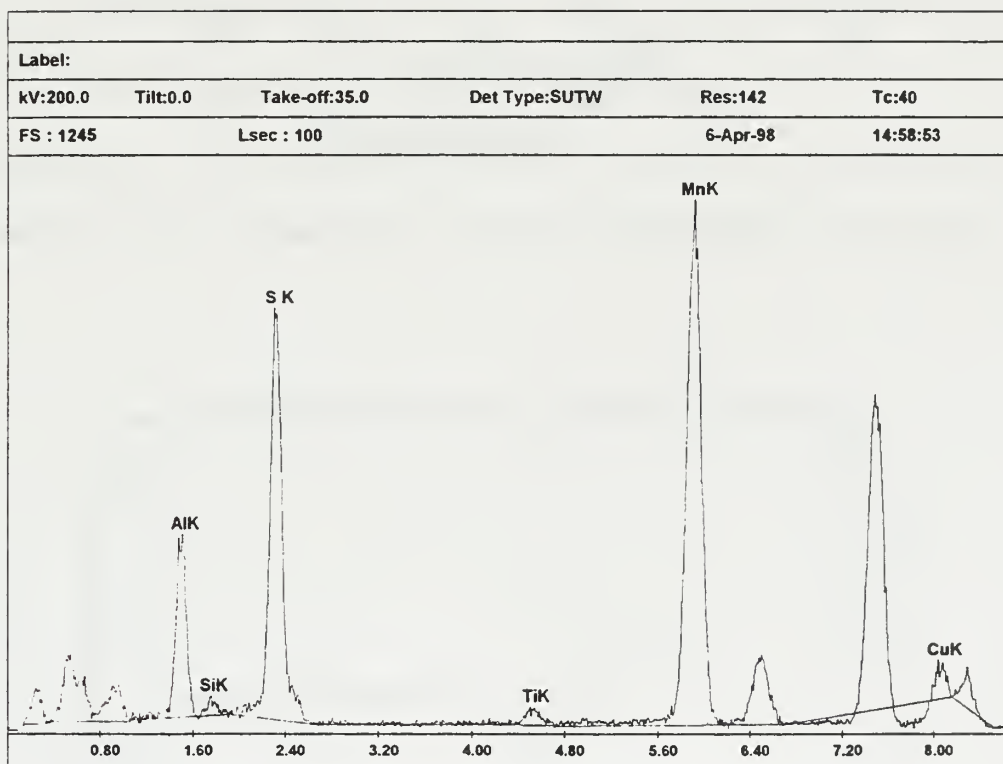
Figure 4.86   EDX analysis of inclusion JWV2 - Region C

121

Figure 4.87   PEELS analysis of inclusion JWV2 Region C - Ti$_{L2,3}$ spectrum

Figure 4.88   PEELS analysis of inclusion JWV2 Region C - O$_K$ spectrum

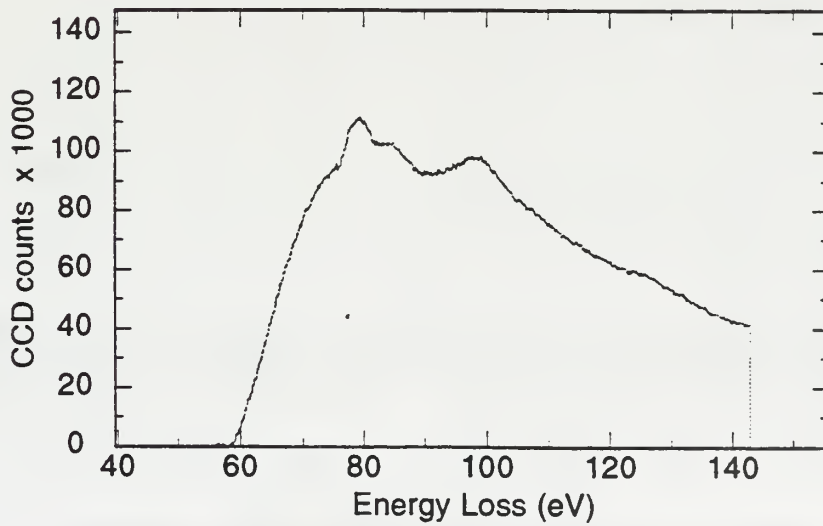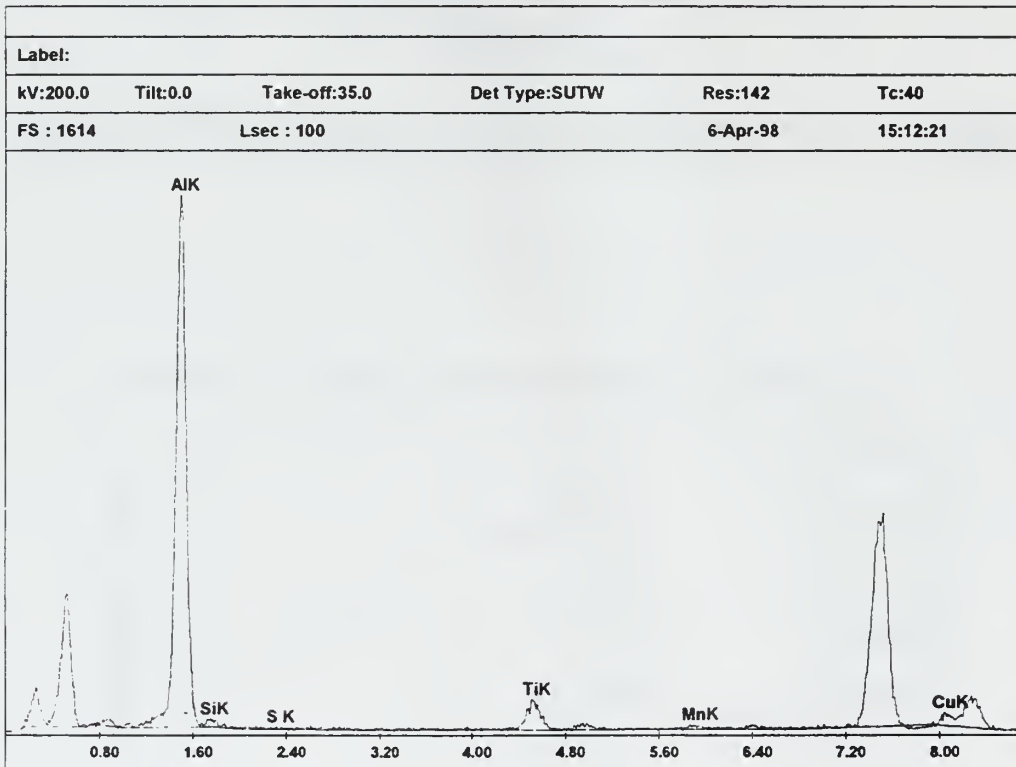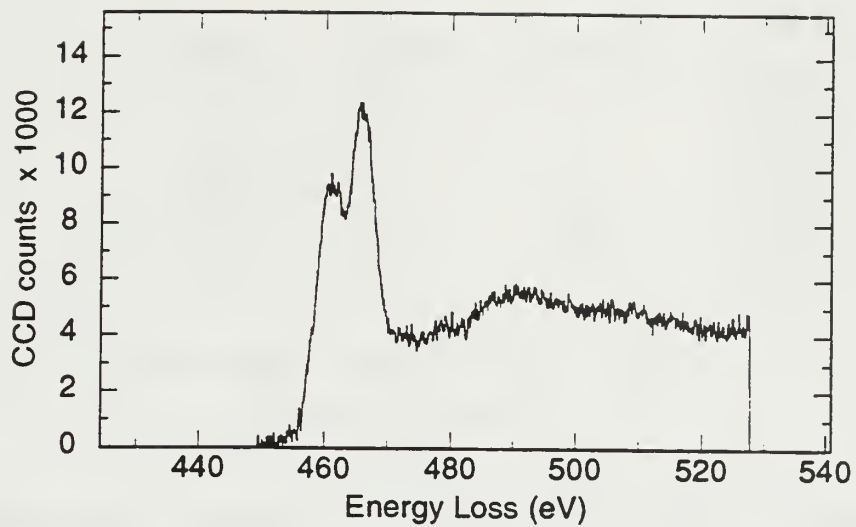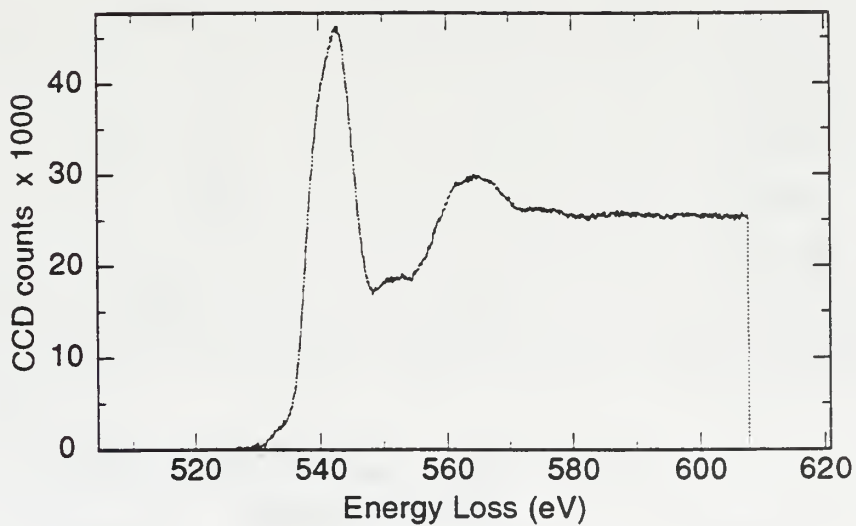Figure 4.89   PEELS analysis of inclusion JWV2 Region C - $Mn_{L2,3}$ spectrum
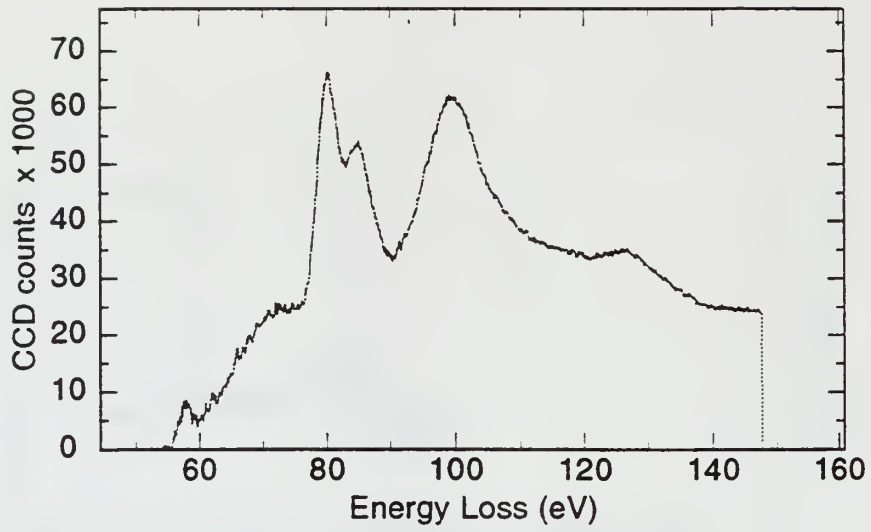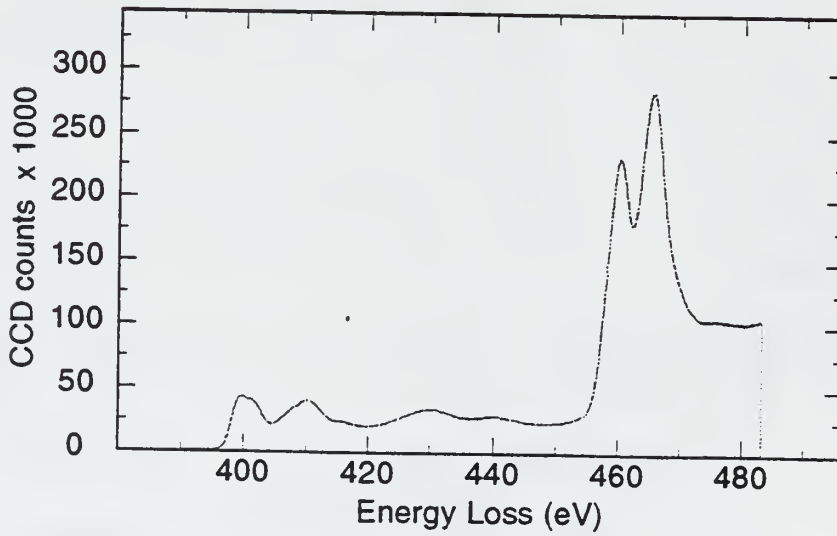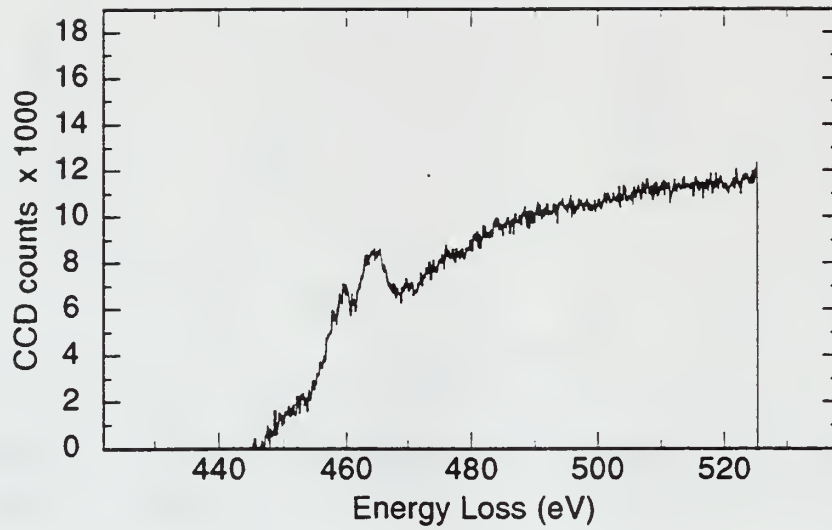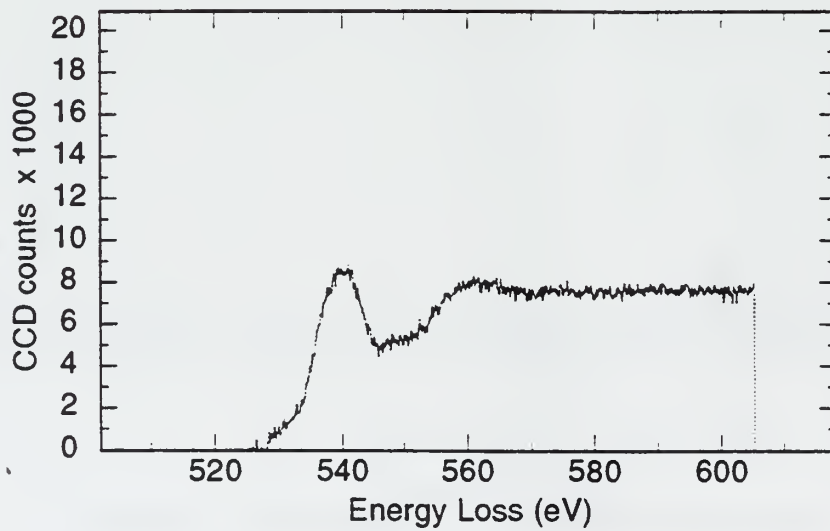

Figure 4.90   PEELS analysis of inclusion JWV2 Region C - $Al_{L2,3}$ spectrum
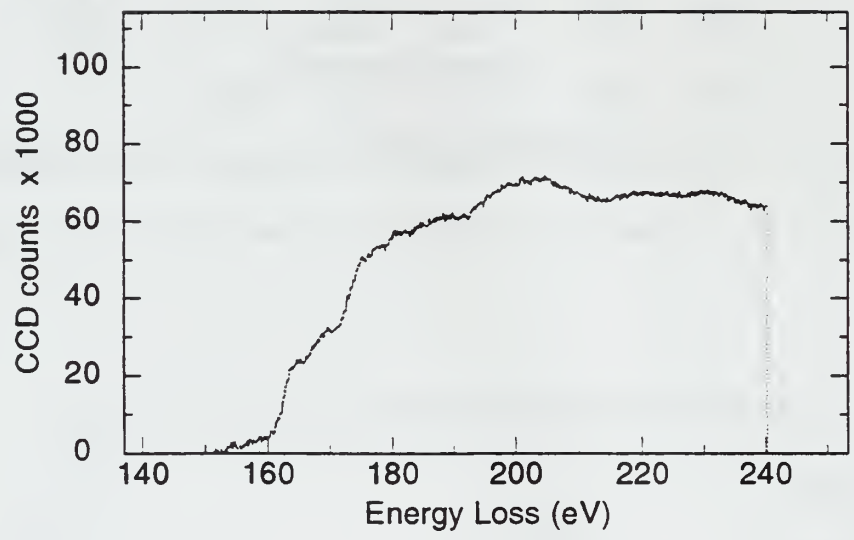
Figure 4.91   PEELS analysis of inclusion JWV2 Region C - S_L spectrum

124

d.   *Inclusion JWV3*

Inclusion JWV3 shown in Figure 4.92 was analyzed in two Regions, A and B, by both EDX and PEELS. The inclusion appeared to be comprised of two separate phases consisting of a sphere in the center of a cube. EDX in Region A, shown in Figure 4.93, again confirmed the presence of high amounts of aluminum (84.0%) followed by lower amounts of titanium (11.6%) and the other elements indicating the presence of Al_2O_3. PEELS analysis was conducted on titanium, oxygen and aluminum in Region A, Figure 4.94 through 4.96. These spectra indicated the presence of the Al_2O_3 formation with possibly small amounts of TiO and/or TiN. EDX analysis in Region B showed a much lower amount of aluminum (7.1%) and an increased amount of titanium (76.8%) indicating the presence of TiO and/or TiN, Figure 4.97. PEELS analysis Figures 4.98 through 4.101 showed that TiN had formed along with a small amount of Al_2O_3 formation. PEELS maps of the inclusion were produced and are displayed in Figure 4.102 in order to better clarify the segregation of the inclusion composition. The oxygen, titanium, aluminum and nitrogen maps showed two separate distributions. The inner sphere appears to be predominantly Al_2O_3 and the outer cubic formation is primarily TiN.
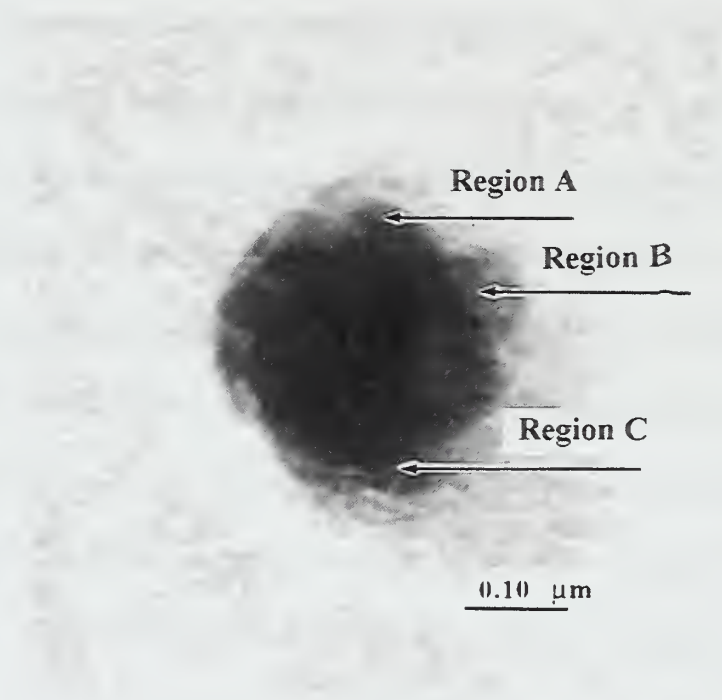
Figure 4.92   TEM micrograph of inclusion JWV3

Element	Weight %	Atomic %
AlK	74.6	84.0
SiK	1.1	1.2
S K	0.7	0.6
TiK	18.2	11.6
MnK	0.6	0.3
CuK	4.8	2.3
Total	100.0	100.0

Label:					
kV:200.0	Tilt:0.0	Take-off:35.0	Det Type:SUTW	Res:142	Tc:40
FS : 5568		Lsec : 100		6-Apr-98	18:06:24

Figure 4.93   EDX analysis of inclusion JWV3 - Region A

127

Figure 4.94   PEELS analysis of inclusion JWV3 Region A - $Ti_{L2,3}$ spectrum
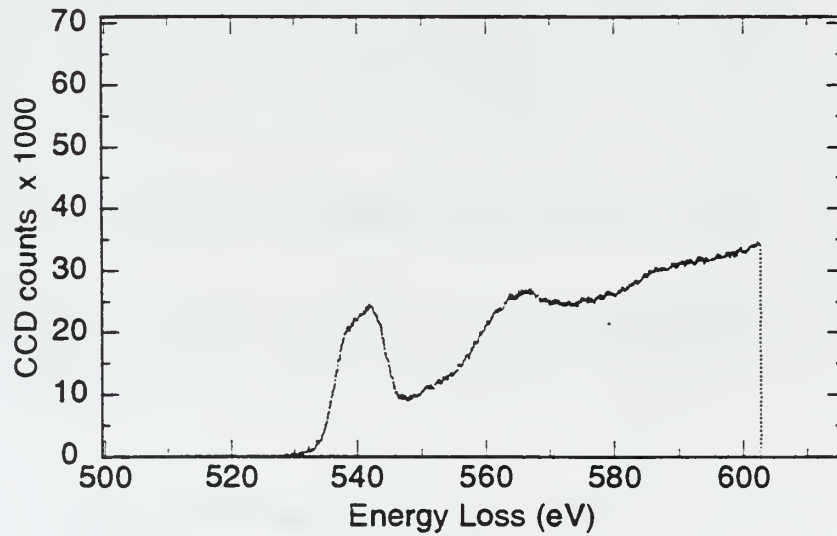
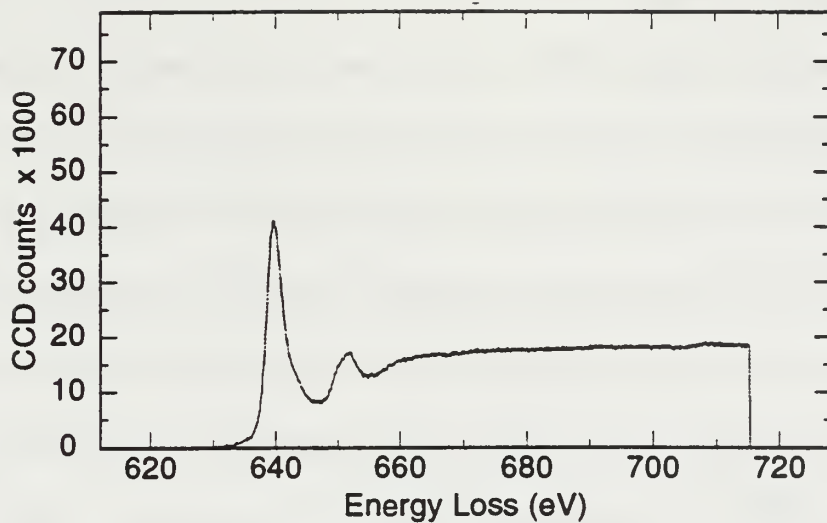Figure 4.95   PEELS analysis of inclusion JWV3 Region A - O_K spectrum
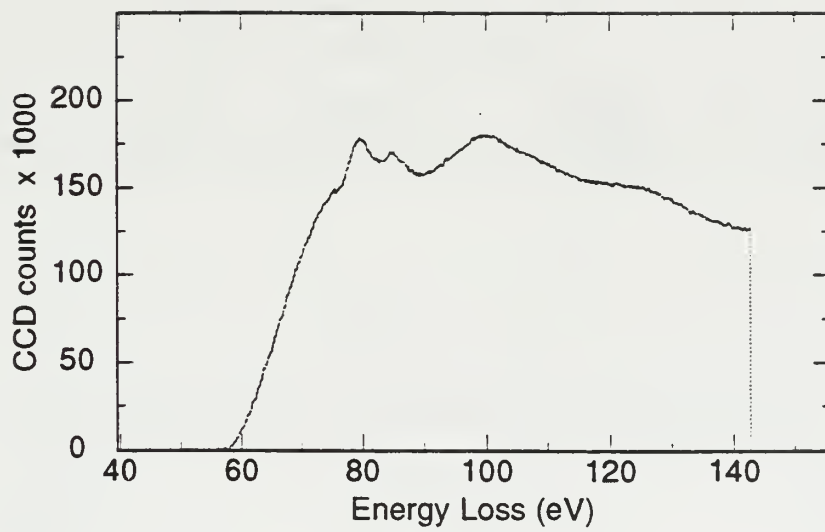
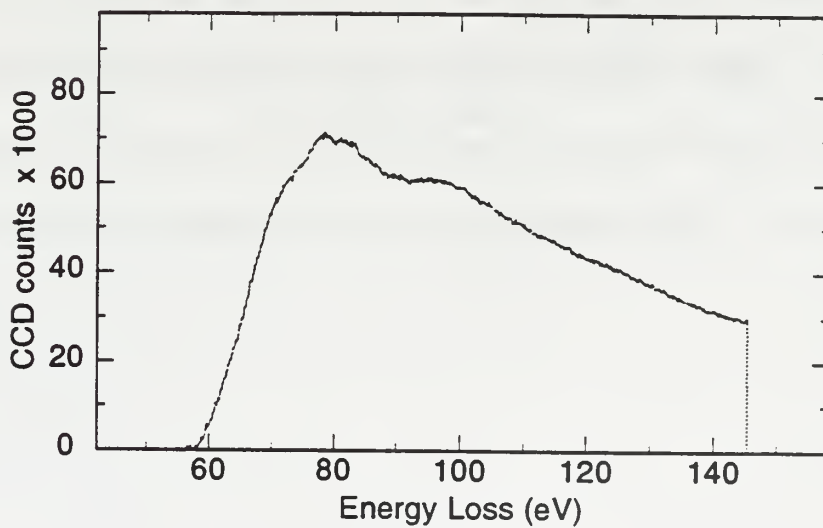Figure 4.96   PEELS analysis of inclusion JWV3 Region A - Al$_{L2,3}$ spectrum

| Element	Weight %	Atomic %
AlK	4.1	7.1
SiK	2.1	3.5
S K	0.3	0.4
TiK	77.5	76.8
MnK	0.9	0.8
CuK	15.2	11.3
Total	100.0	100.0

Label:					
kV:200.0	Tilt:0.0	Take-off:35.0	Det Type:SUTW	Res:142	Tc:40
FS : 886		Lsec : 100		6-Apr-98	18:02:21

Figure 4.97   EDX analysis of inclusion JWV3 - Region B

130

Figure 4.98   PEELS analysis of inclusion JWV3 Region B - Ti$_{L2,3}$ spectrum
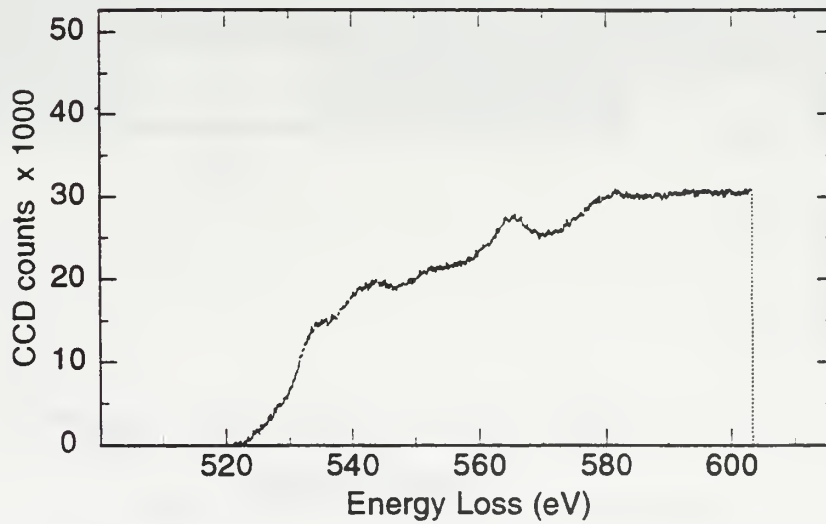
Figure 4.99   PEELS analysis of inclusion JWV3 Region B - O$_K$ spectrum
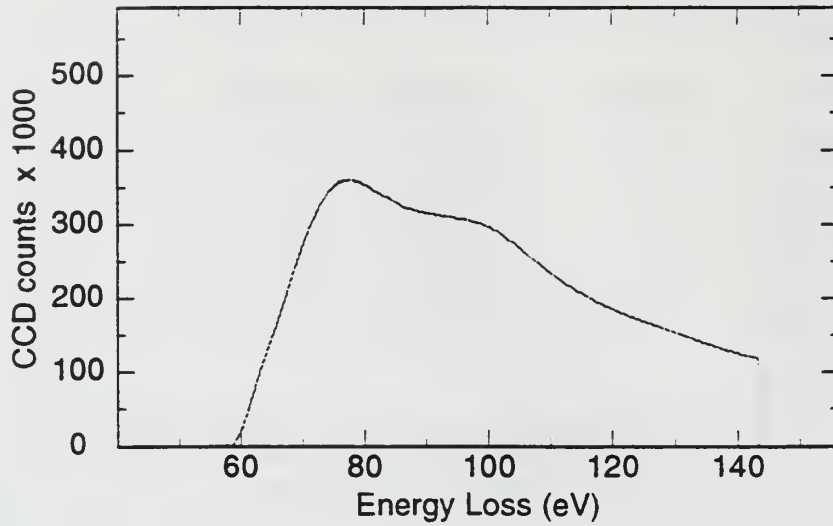
Figure 4.100   PEELS analysis of inclusion JWV3 Region B - Al$_{L2,3}$ spectrum
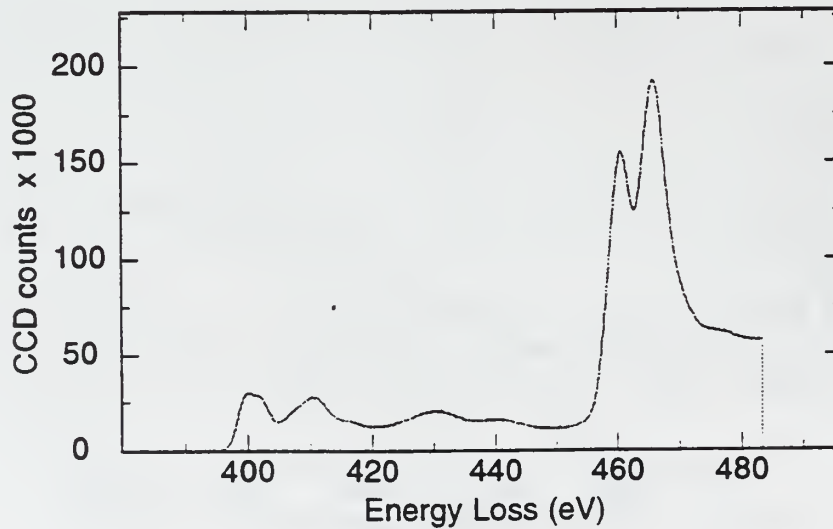
Figure 4.101   PEELS analysis of inclusion JWV3 Region B - N$_K$ spectrum
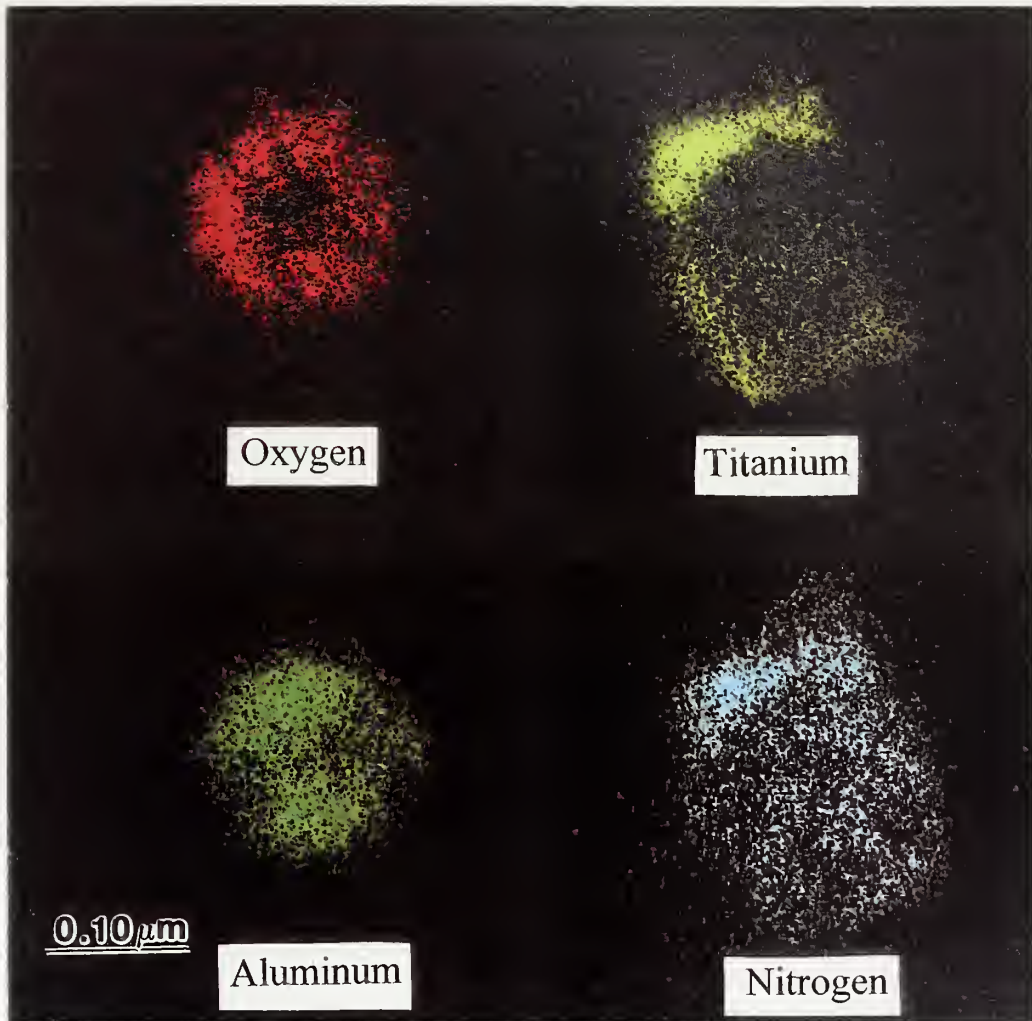
Figure 4.102   PEELS maps of inclusion JWV3

F.   ANALYSIS AND SUMMARY

The results of the microchemical analysis on samples Y, Z, and V proved to be close to the thermodynamic predictions. Sample Y inclusions contained TiO as the primary component followed with other reaction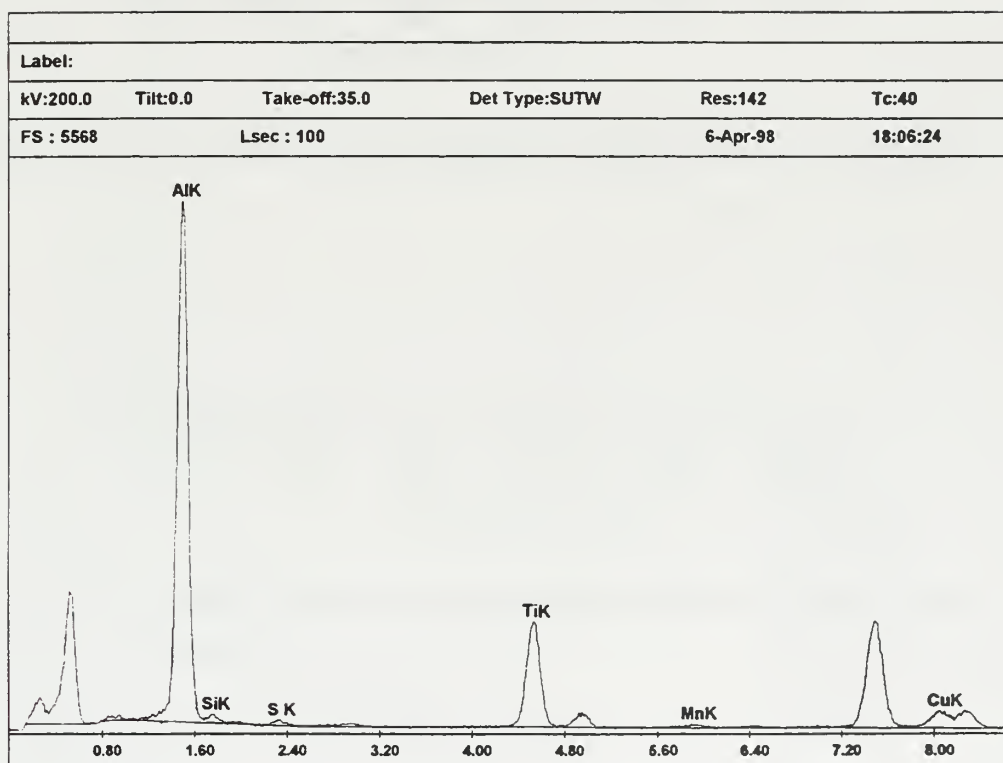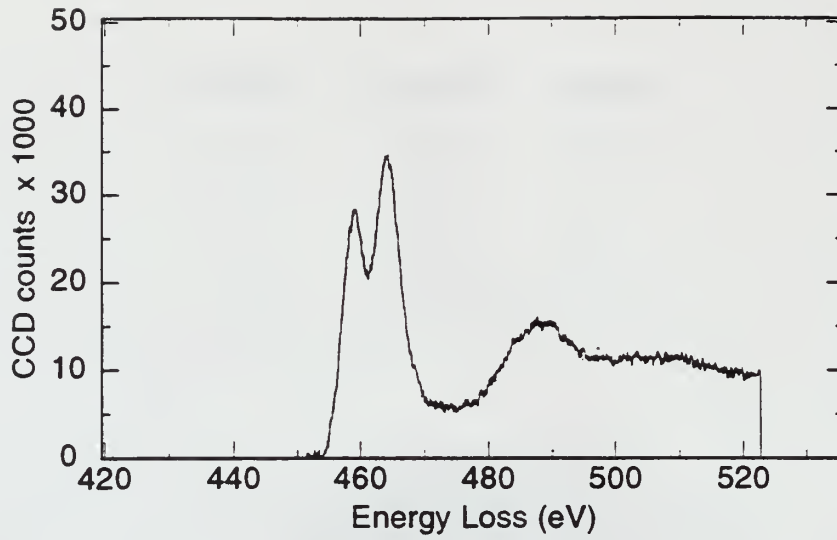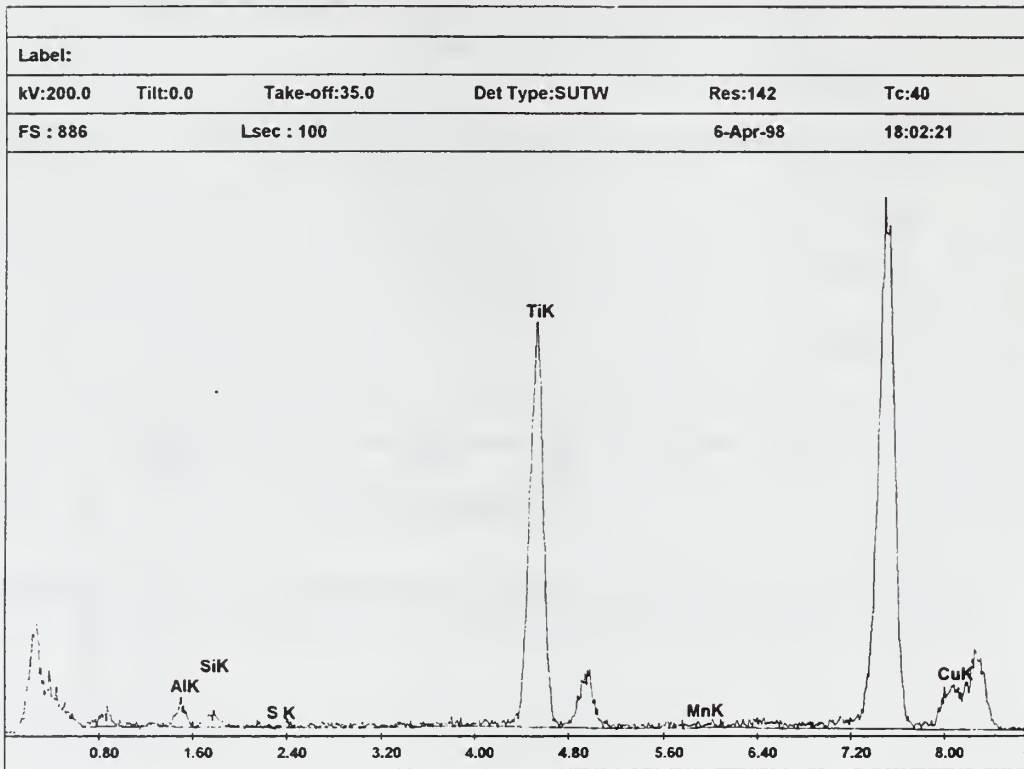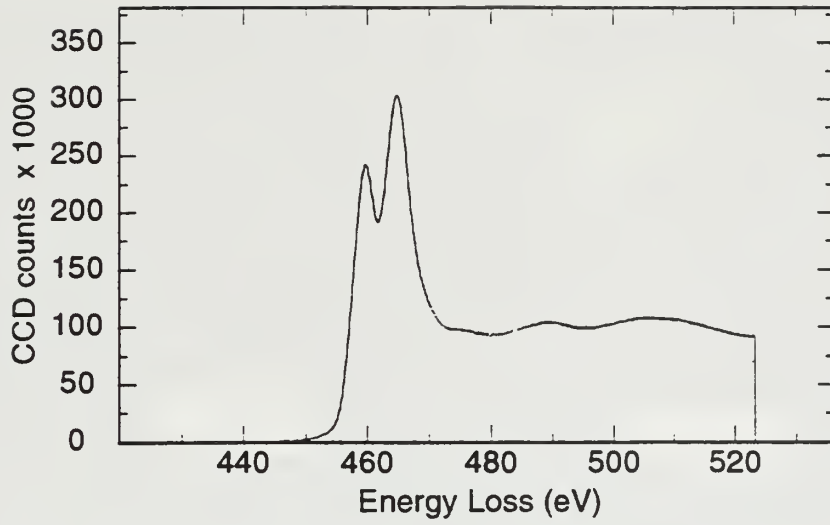 products in the form of SiO_2, MnO possibly $MnO.SiO_2$ and Cu(Mn)S. Very little Al_2O_3 was found which was thermodynamically predicted due to the low aluminum content in the matrix of the final pass. Sample Z inclusions were primarily comprised of Al_2O_3 and TiO. In some inclusions these components segregate whereas in others they were homogeneously distributed, possibly as a compound. Very small amounts of MnO, SiO_2 and sulfides were also found. Both Al_2O_3 ands TiO formation and small amounts of the other deoxidizers were thermodynamically predicted. What was not predicted was the finely dispersed two phase mixture of Al_2O_3 and TiO or possible compound of the two. There is no evidence for such a compound in the literature and this must be considered a new and highly relevant discovery. For Sample V the primary reaction was Al_2O_3 with some TiO, SiO_2 and MnO formation followed by titanium reacting with dissolved nitrogen to form TiN. The large presence of Al_2O_3 was thermodynamically predicted due to the large amount of aluminum in the final weld pass matrix. The faceted cubic TiN formations were expected as a result of the deoxidizing power of the aluminum and the free energy of formation for TiN.

The results showed that primary titanium deoxidation reaction for all three samples to be TiO rather than TiO_2. Additional diffraction analysis needs to be conducted to

confirm these results and to completely determine the constitution of the phases suggested by EDX and PEELS.

V. SUMMARY

A. CONCLUSIONS

Non-Metallic inclusions in the C-Mn SMA weldment samples analyzed have complex chemical compositions.

The EDX analyses allowed identification of elements present in the inclusions but was unable to quantify the oxygen and thus identify the titanium oxide(s) present.

PEELS (ELNES) analysis was able to determine the coordination of the titanium and oxygen atoms and indicated that the TiO like coordination as opposed to TiO_2 to be the most likely for all samples.

For sample Y, Ti (390 ppm) and Al (13 ppm), the primary deoxidization products were found to be TiO with a small amounts of MnO and SiO_2. (Some Cu(Mn)S was also present)

For sample Z, Ti (420 ppm) and Al (160 ppm), the deoxidization products were found to be Al_2O_3 and TiO. These phases formed in both separate regions and as evenly distributed two phase mixture or possible compound. Very small amounts of MnO, SiO_2 and sulfides were also found.

For sample V, Ti (540 ppm) and Al (580 ppm), the primary deoxidation product appeared to be Al_2O_3 with the majority of Ti reacting with dissolved nitrogen to form TiN. The TiN inclusions were present as cuboids in the inclusions as a result of their face

centered cubic crystalline structure. Isolated areas in the inclusions showed small amounts of TiO, $TiO.Al_2O_3$ mixtures or compounds, MnO, SiO_2 and sulfides.

From the above information it appears that inclusions containing MnO, SiO_2, $MnO.SiO_2$, TiO, $TiO.Al_2O_3$ mixtures or compounds and Al_2O_3 (together with TiN) can all nucleate acicular ferrite but each type apparently varies in effectiveness.

Soluble aluminum left after deoxidization in the Al (580 ppm) sample may lower acicular ferrite content due to its ability to stabilize austenite grains and promote sideplate ferrite. Prior austenite grain size reduction may also affect the acicular ferrite content and thus explain the reduced level of acicular ferrite in sample V.

B.   SUGGESTIONS FOR FURTHER RESEARCH

Scanning electron microscopy analysis needs to be performed on all three samples to determine the inclusion size distribution for each.

The prior austenite grain size needs to be determined for each sample in order to check if the increase in aluminum reduces the acicular ferrite by changing prior austenite grain size.

Thin foil TEM samples need to be prepared to determine if epitaxy (lattice matching) between the inclusion and acicular ferrite exists.

Additional diffraction analysis needs to be conducted to try and determine the exact nature of the phases predicted by EDX and PEELS..

LIST OF REFERENCES

1. Flax, R.W., Keith, R.E. and Randall, M.D., "Welding the HY Steels," *ASTM Special Technical Publication*, 1971.

2. Kou, S., *Welding Metallurgy*, John Wiley and Sons, 1987.

3. *Guidelines for Classification of Ferritic Steel Weld Metal Microstructural Constituents using the Light Microscope*. IIW Doc. No. IXJ-102-85.

4. Bhadeshia, H.K.D.H., "Control of Weld Metal Microstructure and Properties," *The Metallurgy, Welding, and Qualification of Microalloyed (HSLA) Steel Weldments*, American Welding Society, 1990.

5. Callister, W.D., *Materials Science and Engineering: An Introduction*, John Wiley and Sons, Inc., New York, 1991.

6. Bhadeshia, H.K.D.H. and Christian, J.W., "Bainite in Steels," *Metallurgical Transactions A*, Vol. 21A, 1990.

7. Strangwood, M. and Bhadeshia, H.K.D.H., "The Mechanism of Acicular Ferrite Formation in Steel Weld Deposits," *International Conference on Trends in welding Research*, ASM International, 1989.

8. Yang, J.R. and Bhadeshia H.K.D.H., "Orientation Relationships Between Adjacent Plates of Acicluar Ferrite in Steel Weld Deposits," *Materials Science and Technology*, 1989.

9. Ricks, R.A., Howell, P.R. and Barrite, G.S., "The Nature of Acicular Ferrite in HSLA Steel Weld Metals," *Journal of Materials Science*, 1982.

10. Edmonds, D.V. and Cochrane, R.C., "Structure-Property Relations in Bainitic Steels," *Metallurgical Transactions*, Vol. 21A, 1990.

11. McHale, P.F., *Factors Influencing the Microstructural and Mechanical Properties of ULCB Steel Weldments*, Master's Thesis, Naval Postgraduate School, Monterey, CA, 1991.

12. Sugden, A.A.B. and Bhadeshia, H.K.D.H., "The Nonuniform Distribution of Inclusions in Low-Alloy Steel Weld Deposits," *Metallurigical Transaction A*, 1988.

13. Kiessling, R.K., *Non-metallic Inclusions in Steel, Part V*, The Institute of Metals, 1989.

14. Babu, S.S., David, S.A., Vitek, J.M., Mundra, K. and Debroy, T., "Development of Macro- and Microstructures of C-Mn Low Alloy Steel Welds: Inclusion Formation," *Materials Science and Technology 11*, 1995.

15. Bhatti, A.R., Saggese, M.E., Hawkins, D.N., Whiteman, J.A. and Golding, M.S., "Analysis of Inclusions in Submerged Arc Welds in Microalloyed Steels," *Welding Research Supplement*, 1984.

16. Hertzberg, R.W., *Deformation and Fracture Mechanics of Engineering Materials*, John Wiley and Sons, Inc., 1989.

17. Grong, O. and Matlock, D.K., "Microstructural Development in Mild and Low-Alloy Steel Weld Metals," *International Metals Reviews*, Vol. 31, 1986.

18. Kiessling, R. and Lange, N., *Nonmetallic Inclusions In Steel*, The Metals Society , 1978.

19. Ohkita, S., Homma, H., Matsuda, S., Wakabayashi, M. and Yamamoto, K., "Improvement of HAZ Toughness of HSLA Steel by Finely Dispersed Titanium Oxide," *Nippon Steel Technical Report*, No. 37, 1988.

20. Grong, O., Kluken, A.O., Nylund, H.K., Dons, A.L. and Hjelen, J., "Catalyst effects in Heterogeneous Nucleation of Acicular Ferrite," *Metallurgical and Materials Transition A*, Vol. 26A, 1995.

21. Komizo, Y. and Fukada, Y., "Toughness Improvement in Weld metal of Carbon and HSLA Steels in Japan," *Sumitomo Metal Industries, Ltd.*, 1988.

22. Abson, D.J. and Pargeter, R.J., "Factors Influencing As-deposited Strength, Microstructure and Toughness of Manual Metal Arc Welds Suitable for C-Mn Steel Fabrications," *International Metals Review*, Vol. 31, No. 4, 1986.

23. Muan, A. and Osborn, E.F., *Phase Equilibrium Among Oxides in Steelmaking*, Addison-Wesley Publishing Company, 1965.

24. Fox, A.G., Eakes, M.W. and Franke, G.L., "The Effect of Small Changes in Flux Basicity on the Acicular Ferrite Content and Mechanical Properties of Submerged-Arc Weld Metal of Navy Hy-100 Steel," Submitted, *Welding Research Supplement to The Welding Journal*, 1995.

25. Bhadesia, H.K.D.H., *Bainite in Steels*, Institute of Metals, 1992.

26. Zhang, Z. and Farrar, R.A., "Role of Non-Metallic Inclusions in Formation of Acicular Ferrite in Low Alloy Weld Metals," *Materials Science and Technology*, 1996.

27. Fox, A.G. and Brothers, D.G., "The Role of Titanium in the Non-Metallic Inclusions which Nucleate Acicular Ferrite in the Submerged Arc Weld (SAW) Fusion Zones of Navy HY-100 Steel," *Scripta Metallurgica et Materiala*, 1995.

28. Gregg, J.M. and Bhadeshia, H.K.D.H, "Solid-State Nucleation of Acicular Ferrite on Minerals added to Molten Steel," *Acta Metallurgica, Inc.*, Vol. 45, No. 2, 1997.

29. Dowling, J.M. ,Corbett, J.M. and Kerr, H.W., "Inclusion Phases and the Nucleation of Acicular Ferrite in Submerged Arc Welds in high Strength Low Alloy Steels," *Metallurgical Transactions A*, 1986.

30. Greene, M.K., "The Effects of Titanium on the Mechanical Properties of Shielded Metal Arc Welding (SMAW) of C-Mn Steels," Master's Thesis, Naval Postgraduate School, Monterey, CA, 1997.

31. Blais, C., L' Esperance, G., Baril, E. and Forget, C., "Characterization of Small Inclusions: SEM vs. TEM, or is it Even Worth Considering SEM?," *Microscopy and Microanalysis*, San Francisco Press Inc., 1996.

32. Evans, G. M., *Effect of Aluminum and Nitrogen on Ti-B Containing Steel Welds.* IIW/IIS Doc. II - A- - 96.

33. Evans, G. M., *Microstructures and Properties of Ferritic Steel Welds Containing Ti and B.* IIW/IIS Doc. II - 1264 - 95.

34. Williams, D.B., *Practical Analytical Electron Microscopy in Materials Science*, Philips Electronic Instruments Inc., 1984.

35. Williams, B.D. and Carter, C.B., *Transmission Electron Microscopy*, Plenum Press, 1996.

36. Cullity, B.D., *Elements of X-ray Diffraction Second Edition*, Addison-Wesley Publishing Company, Inc., 1978.

37. Smallman, R.E., *Modern Physical Metallurgy*, Butterworth-Heinemann Ltd., 1992.

38. Ahn, C.C. and Krivanek, O.L., *EELS Atlas*, Gatan, Inc., 1983.

39. Fox, A.G., Private Communication, 1998.

INITIAL DISTRIBUTION LIST

1. Defense Technical Information Center...2
    8725 John J. Kingman Rd., STE 0944
    FT. Belvoir, Virginia 22060-6218

2. Dudley Knox Library..2
    Naval Postgraduate School
    411 Dyer Rd.
    Monterey, California 93943-5100

3. Naval Engineering, Code34..1
    Naval Postgraduate School
    Monterey, California 93943-5100

4. Department Chairman, Code ME/Mc..1
    Department of Mechanical Engineering
    Naval Postgraduate School
    Monterey, California 93943-5000

5. Dr. Alan G. Fox, Code ME/FX..2
    Department of Mechanical Engineering
    Naval Postgraduate School
    Monterey, California 93943-5000

6   Dr. Joe Blackburne 1
    Naval Surface Warfare Center
    Carderock Division, Code 615
    9500 McAurthur Boulevard
    Bethesda, Maryland 20084-5000

7. Dr. G. M. Evans..1
    34 Grenfell Park
    Parkgate
    South Wirral L64 TT United Kingdom

8. Lt. Jon D. Walters 2
    912 Ellston St.
    Colorado Springs, Colorado 80907